Aalto University
School of Engineering

Quinton Weaver

# Numerical Modeling and Validation for the Development of Tool Geometry and Material for Friction Stir Welding of Thick Copper

Thesis submitted in partial fulfillment of the requirements
for a degree of Master of Science in Technology

Aalto University, School of Engineering
Espoo, Finland. May 2017
Supervisor: Professor Pedro Vilaça
Advisor: Timo Salonen

**Author** Quinton B. Weaver

**Title of thesis** Numerical Modeling and Validation for the Development of Tool Geometry and Material for Friction Stir Welding of Thick Copper

**Degree programme** Mechanical Engineering

**Major/minor** Mechanical Engineering **Code** IA3027

**Thesis supervisor** Professor Pedro Vilaça

**Thesis advisor(s)** Timo Salonen

**Date** 29.05.2017 **Number of pages** 96 + 6 **Language** English

**Abstract**

This thesis catalogs the development of a numerical model for the Friction Stir Welding (FSW) of large sealed copper canisters used in the disposal of nuclear waste. FSW is a highly complex process, with many interconnected physical phenomena that determine the quality and effectiveness of the weld. FSW of copper is particularly challenging due to the increased processing temperature required. Specifically, for the purpose of FSW 50 mm thick copper canisters, Posiva Oy, SKB, and TWI jointly developed the current process. While the current process produces acceptable welds, it was noted that further improvements could be made to the probe material and geometry. These improvements were not explored during the original development cycle due to the high cost associated with the manufacturing and testing of full-scale probe prototypes. The numerical model developed in this thesis combats this problem by allowing multiple probe prototypes to be simulated, and their performance compared to the original probe design.

The model developed in this work uses a highly refined mesh near the probe surfaces, giving it the capability to simulate very fine details in the probe geometries. A rigid sliding mesh technique gives the model the ability to simulate complex 3D material flow through time. A strain rate and temperature dependent material model, based on the Sheppard-Wright flow stress equation, was also created specifically for copper. The model was validated by comparing the simulation's results to evidence seen on actual probes. The probes simulated in this work were previously created using analytical design criteria and were focused on improving material flow properties, especially near the probe tip. The results of the simulations give proof of concept that comparative analysis of different probe designs can lead to a more optimized probe without the need for prototyping of every design revision.

The current probe material, Nimonic 105, was chosen for its high temperature strength and stability. Other material options could exist but need to be systematically evaluated. The Low Cycle Fatigue (LCF) test protocol developed in this work is designed to evaluate a material's performance in a FSW environment. Once a baseline for Nimonic 105 has been established using this protocol, other materials could be evaluated using this protocol.

**Keywords** Friction Stir Welding, FSW, Tool Design, Ansys, CFD, Numerical Modeling, Material Flow, Non-Newtonian, Viscosity, Zener-Hollomon, Sheppard-Wright, Oxygen Free Phosphorus, OFP Copper, Nuclear Disposal, Canister, Low Cycle Fatigue, Nimonic.

# Acknowledgments

Thank You:

To my supervisor Pedro Vilaça, for introducing me to the world of friction sir welding and for guiding me while I undertook this project. To Timo Salonen and Posiva Oy, for sharing a wealth of knowledge while allowing me to work on such an interesting subject. To Aalto University, for allowing an outsider to freely study and learn at such a great institution. To the engineering support staff, for all the help during my studies and my thesis. To my fellow students and colleagues, for such a welcoming workplace.

To my parents and my sisters, for pushing me to excel and for supporting me from halfway around the world. To Brian, Kevin, and Daniel, for the many hours of round-table homework, discussion (and beer drinking), and for the years of friendship. Finally, to my wife Elizabeth, for agreeing to leave her dog and her family to go on this Finnish adventure with me.

Quinton Weaver

Espoo, 29.5.2017

# Contents

1 Introduction ... 1
  1.1 Scope of the Thesis ... 1
  1.2 Work Plan and Objectives ... 2
  1.3 Organization of the Thesis ... 3
2 State of the Art ... 5
  2.1 Introduction ... 5
  2.2 Fundamentals of the FSW Application ... 6
    2.2.1 Tool Geometries ... 7
  2.3 FSW of Copper Canisters ... 9
  2.4 Canister FSW Tool Material ... 11
    2.4.1 Material and Coating Microstructural Analysis ... 12
  2.5 Canister FSW Tool Design ... 15
    2.5.1 Analytical Design Improvements ... 17
  2.6 FSW Modeling ... 19
    2.6.1 General Numerical Modeling ... 21
    2.6.2 Copper Numerical Modeling ... 22
3 Numerical Modeling Approach ... 25
  3.1 Introduction ... 25
  3.2 Geometry and Mesh ... 26
    3.2.1 Interfaces and Solid Walls ... 29
  3.3 Sliding Mesh ... 30
4 Model and Solver Theory ... 33
  4.1 Introduction ... 33
  4.2 Governing Equations ... 34
    4.2.1 Solver Method; Segregated or Coupled ... 35
  4.3 Material Model ... 37
    4.3.1 Iterative Viscosity Function ... 42
  4.4 Boundary Conditions ... 43
    4.4.1 Initial Conditions ... 44
5 Model Validation ... 45
  5.1 Introduction ... 45
  5.2 Viscosity & Strain Rate Zones ... 45
    5.2.1 Strain Rate Cracking ... 48
  5.3 Pressure ... 49
  5.4 Pressure Integration (Forces) ... 51
6 Probe Comparison Results ... 55
  6.1 Introduction ... 55
  6.2 Velocity Characteristics ... 56
    6.2.1 Velocity Streamlines & Vectors ... 56
    6.2.2 Axial Velocity Contours ... 58
  6.3 Viscosity & Strain Rate ... 60
  6.4 Heat Generation ... 63
7 Low Cycle Fatigue Material Testing ... 67
  7.1 Introduction ... 67
  7.2 Experimental Theory & Protocol ... 68
    7.2.1 Preliminary Results ... 71
  7.3 Parameter Verification Results ... 73

        - 7.3.1 Revision 2 Probes ........ 77
        - 7.3.2 Probe Twisting ........ 78
    - 7.4 Microscopic Analysis ........ 79
- 8 Summary ........ 87
    - 8.1 General Comments ........ 87
    - 8.2 Conclusions ........ 87
    - 8.3 Future Work ........ 89
- 9 References ........ 91
- 10 Appendices ........ 95

# Symbols & Abbreviations

ALE - Arbitrary Lagrangian Eulerian
BM - Base Material
CEL - Coupled Eulerian Lagrangian
CFD - Computational Fluid Dynamics
CFL - Courant–Friedrichs–Lewy number
CrN - Chromium Nitride
CT - Computer Tomography
DXZ - Dynamically Recrystallized Zone
EBW - Electron Beam Welding
FEM - Finite Element Method
FSW - Friction Stir Welding
FVM - Finite Volume Method
HAZ - Heat Affected Zone
KBS - Kärnbränslesäkerhet (Nuclear Fuel Safety, Barrier Disposal)
LCF - Low Cycle Fatigue
OFP copper - Oxygen Free Phosphorous-alloyed copper
OM – Optical Microscope
PCBN - Polycrystalline Cubic Boron Nitride
PM - Powder Metallurgy
PVD - Physical Vapor Deposition
R&D - Research and Development
RPEBW - Reduced Pressure Electron Beam Welding
RR - Rotating Region
RRF - Rotating Reference Frame
SEM – Scanning Electron Microscope
SKB - Svensk Kärnbränselhantering AB (Swedish Nuclear Fuel and Waste Management Co)
SoR - Surface of Revolution
SZ - Stirred Zone
TMAZ - Thermomechanically Affected Zone
TWI - The Welding Institute
UDF - User Defined Function
UTS - Ultimate Tensile Strength

## Symbols

$c_p$ - Specific heat
E - Enthalpy
k - Thermal conductivity
P - Pressure
Q - Activation energy
R - Universal gas constant
T - Temperature
t - Time (timestep)
v - Velocity
V - Volume
ρ - Density
ϕ - General scalar variable

$\mu$ - Dynamic viscosity
$\vec{u}$ - Fluid velocity
$\vec{u}_g$ - Mesh velocity
$\dot{\varepsilon}$ - Strain rate
$\sigma_e$ - Flow stress
Z - Zener-Hollomon parameter
$\bar{\bar{\tau}}$ - Stress tensor
$\bar{\bar{D}}$ - Rate of deformation tensor

# 1 Introduction

## 1.1 Scope of the Thesis

This thesis catalogs the development of a numerical model for the Friction Stir Welding (FSW) of large sealed copper canisters used in the disposal of nuclear waste. This work, is part of a cooperation between Posiva Oy and Aalto University, that aims at reviewing the material and design of the probe, based on experimental investigation and validated numerical modeling. A new Low Cycle Fatigue (LCF) test was developed due to the need of comparing different possible probe materials fracture characteristics under real FSW conditions.

FSW is a solid state joining process invented at The Welding Institute in 1991 [1] [2] that uses a rotating, nonconsumable, probe to heat and soften the material. The probe then stirs this softened material, allowing joining to occur between components without melting and resolidification. Because FSW does not melt the material, it is useful for joining materials that are difficult to weld using fusion methods. FSW is also useful where the demands for the structural components are high, such as the aerospace and nuclear industries, because FSW creates lower peak temperatures and has less losses of heat into the base materials than fusion welding. Additionally, the welded material will behave as having been hot formed, which can improve the material properties over cast structures.

FSW is most commonly done on aluminum alloys, but has recently been used more in copper, magnesium alloys, steels, and thermoplastics. Due to copper's melting temperature and thermal conductivity, 1085 °C and 401 $\frac{\mathrm{W}}{\mathrm{m}*\mathrm{K}}$ respectively, it is difficult to weld using traditional methods. These properties also make it more demanding for FSW, due to the higher processing temperatures, when compared with aluminum alloys. The ideal processing temperature for FSW of copper is roughly 860 °C, i.e. 80 % the melting temperature of copper; in this temperature range the flow stress and activation energies for diffusion are low, allowing for good flow and material joining without melting. In the reference data for this present work, the process is temperature controlled to 845±10 °C [3].

FSW is a complex process with many, often interdependent, material and physics phenomena occurring. Predicting and controlling these phenomena are crucial when establishing an accurate welding procedure specification; a poorly controlled FSW can result in defects, such as void formation, oxide particles alignment and lack of penetration [4] [5]. The real influence of the parameters controlling the process is often difficult to establish. The material flow during FSW will define all the mechanical and microstructural properties of the joint; so, assessing the influence of the tool geometry and parameters in the material flow is of major importance. Tracers and macro/microstructure analysis often give initial and final states of the weld material, but rarely can give material flow characteristics during the actual welding. A validated numerical modeling can be a very useful tool in predicting the complex flow characteristics of the material during the weld.

The probe geometry in FSW of thick components governs most of the material flow. Thus, the probe geometry can significantly affect the quality of the weld, even when using the same control parameters [4]. Numerical modeling can be used to compare different probe geometries and predict what material flow changes will occur with the addition or removal of probe features. Simulation comparison can optimize designs, reduce costs, and lower experiment times. This simulation based designed approach is very appealing in situations where design revisions and experimentation are difficult and very expensive, as typical with most FSW applications. In Posiva's work, creating long welds through thick copper, with complex probe geometries, makes simulation-based improvements to probe design preferable to purely experimental trials. The model produced in this thesis was intentionally developed with enough resolution to observe how the changes in probe geometries affect the weld conditions; including material flow characteristics, heat generation, and viscosity/shear stress patterns.

## 1.2 Work Plan and Objectives

This thesis focused on the development of a Computational Fluid Dynamics (CFD) based numerical model designed specifically for comparing geometry changes between different weld probes. Additionally, the parameters for a strain rate and temperature dependent material model for OFP copper (oxygen free copper alloyed with phosphorus) was developed for use in conjunction with the CFD model. Previous analytical design of new probe concepts was done in Juho Nenonen's master's thesis [6]. In this thesis, the most promising probe concepts developed in Nenonen's work are simulated and compared to a simulation of the original probe. The purpose of this model is to facilitate the optimization of the weld tool geometry by reducing the need for experimental trials to test different design revisions.

Continued development of a coupled multiload and thermal Low Cycle Fatigue (LCF) test was also done in this thesis. This test was developed to expose weld tool material candidates to real FSW conditions, encompassing the cyclic multiaxial loading (torque, bending, axial compression) with temperature, random vibration, and shock that exist during the plunge, dwell, and travel periods of the weld cycle. As the initial concept for this test was already developed, the focus of the work in this thesis was to create a standardized protocol for testing and to determine the correct weld parameters for the most reliable test conditions. Once these parameters were determined, the current probe material (Nimonic 105) was tested to begin establishing a baseline for comparing all other material candidates against.

The objectives of this thesis were:

- Review the current state of the art for FSW of copper in general and for modeling of FSW.
    - Examine any previous work and the current status of sealing copper canisters using FSW for the purpose of disposing nuclear waste.
- Develop a stable CFD model using Ansys Fluent software capable of predicting variations in weld properties based on probe geometry changes.
    - The model should be transient in nature and capable of "advancing" through time in order to track fluctuations of the weld properties as the tool rotates.
- Create a validated material model for OFP copper that can be used to define the material parameters (viscosity) in the numerical solver.
    - Material model should be at least temperature and flow stress dependent; i.e. at least a temperature dependent, non-Newtonian, fluid model.
- Validate the simulations of the original probe to evidence present on the real-world probe and to data available in the process monitoring systems of the canister FSW weld machine.
    - Confirm if expected weak areas of the original probe design are present in the simulation of the original probe (namely flow patterns near the probe tip).
- Compare simulations of the new design concept to simulations of the original probe design.
    - Determine and analyze key parameters, such as flow velocity, between probes.
    - Highlight any advantages or disadvantages different probe designs might have relative to each other.

- Develop a protocol for systematically fatigue testing sample probes and define weld parameters for a LCF test specifically developed for FSW.
    - The weld parameters should allow for fatigue failures of the probe (not overload failures), but should not take prohibitively long times to reach the fatigue limit.
    - Start testing the current probe material (Nimonic 105) to begin establishing a baseline to grade possible material alternatives against the incumbent material.

## 1.3 Organization of the Thesis

After the Introduction, second chapter of this thesis is the State of the Art. This chapter covers the fundamentals of FSW, the history and status of the copper canister FSW process, and a brief review of relevant FSW modeling progress. Not all aspects of the FSW process, or of FSW modeling, are covered in this chapter. The primary focus was on work closely related to Posiva's efforts with sealing copper canisters or to the modeling approaches used in this thesis.

Chapters 3 and 4 describe the theory and methods behind the numerical model used in this work. Chapter 3 focuses on how the model is set up, including how the different geometries and mesh regions are defined. Chapter 4 explains the governing systems behind the model, including the construction of the material model for OFP copper.

Results are presented in chapters 5 and 6. The results in chapter 5 are used to validate the model against experimental data. Some comparison results are included in chapter 5 if the information can be used for both validation and comparison. Simulation-to-simulation results are compared in chapter 6; this chapter focuses mainly on comparing the new design concept (probe B) to the original probe, but other relevant probe comparisons are also included.

Chapter 7 discusses the ongoing work to characterize probe material properties through the development of the FSW LCF test. This work will continue after the writing of this thesis so this chapter focuses on the test setup, protocol, parameter validation, and some early results.

The entire work of this thesis is summarized in chapter 8 and some recommendations for future work are given there.

# 2 State of the Art

## 2.1 Introduction

Since its inception by TWI over 20 years ago, much work has gone into understanding and improving the FSW process. This section will briefly cover the fundamentals of FSW, and then will focus more specifically on work done that is relevant to FSW of copper. This mostly includes work done during the development of sealing copper canisters. The work that has led to the current canister FSW process, current probe material and geometry will be the primary topics. Some of the most relevant numerical modeling efforts, which helps form the foundation for this work, will also be discussed.

Long-term safety is one of the most important requirements in the disposal of spent nuclear fuel. The Finnish Centre for Radiation and Nuclear Safety has regulations requiring a redundant barrier system, such that a deficiency in one of the barriers does not jeopardize long-term safety. These barriers must contain the release of radioactive substances into the environment for at least 10,000 years [7]. SKB invented the KBS multiple barrier system (Figure 1), and through their development partnership, Posiva is using the same method.

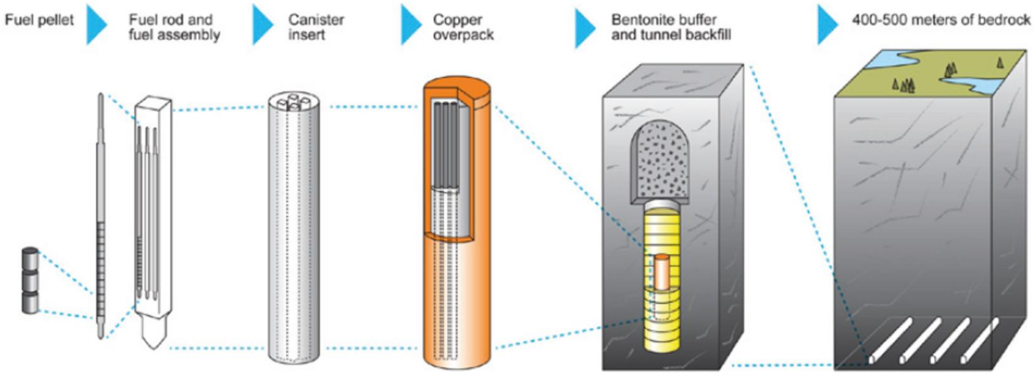
Fuel pellet
Fuel rod and fuel assembly
Canister insert
Copper overpack
Bentonite buffer and tunnel backfill
400-500 meters of bedrock

Figure 1: The KBS multibarrier principle for nuclear waste disposal. [8]

The KBS system involves taking assemblies of spent fuel rods and placing them into a cast iron insert for mechanical protection (Figure 2) [7]. This insert is then placed into a 50 mm thick copper canister for corrosion resistance; the corrosion of the canisters is expected to be less than a few millimeters in 100,000 years [9]. These canisters are then sealed using FSW for joining the lid to the canister body. After the canisters are sealed, they are buried in tunnels under at least 420 meters of bedrock. A bentonite buffer further protects the buried canisters from corrosion and mechanical damage. Finally, the tunnels are sealed using bentonite to keep out water (for both corrosion resistance and pollution mitigation) and also to block any access from the surface [7].

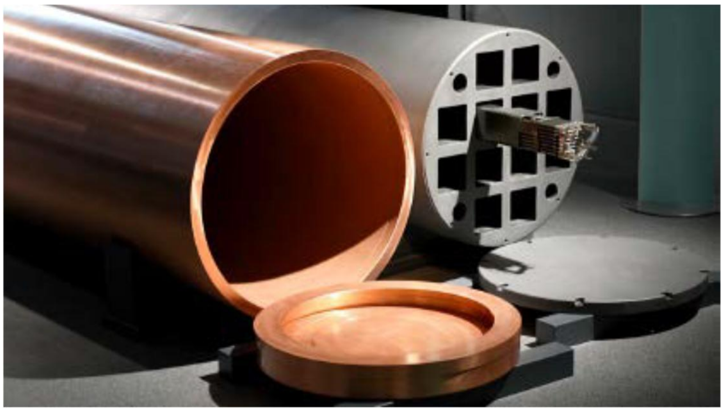

Figure 2: The copper canister, lid, cast iron insert, and fuel rod assembly. [7]

## 2.2 Fundamentals of the FSW Application

FSW works by using a rotating tool (usually a probe and shoulder) plunged into a base material, creating heat through friction and viscous dissipation of shear stress. This heat softens the material and promotes material flow, allowing the tool to stir the material. Once the base material has reached a sufficient temperature, the tool is forced transversely through the material, creating a weld path. As the tools spins, it pulls material from the advancing side of the weld over to the retreating side. A downward force is applied to keep the tool in the material and to maintain enough forging force in the processed zone [5].

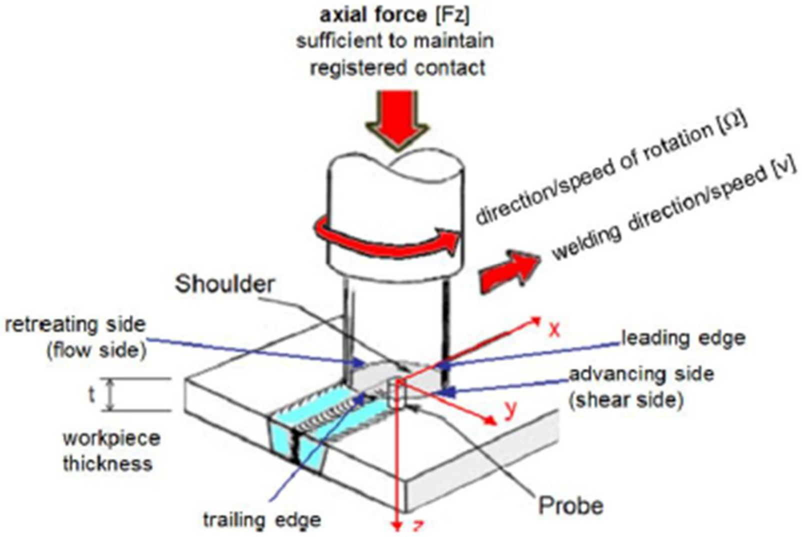
axial force [Fz]
sufficient to maintain
registered contact
direction/speed of rotation [Ω]
welding direction/speed [v]
Shoulder
retreating side
(flow side)
leading edge
x
advancing side
(shear side)
y
t
workpiece
thickness
trailing edge
Probe
z

Figure 3: Schematic of the fundamental FSW process. [5]

FSW is a complex thermomechanical process, with many interconnected parameters that determine the quality and effectiveness of the weld. Some (but not all) of the affecting factors are tool rotational speed, weld travel speed, forging force, thermal conductivity of weld material, and tool geometry. The material being welding can be separated into three major areas: the base material (BM), the heat affected zone (HAZ), and the stirred zone (SZ). The SZ is the region that undergoes plastic deformation and it can be further divided into two more zones: the thermomechanically affected zone (TMAZ) and the dynamically recrystallized zone (DXZ). The TMAZ undergoes small amounts of deformation and typically shows a distorted version of the BM grain structure. The DXZ, also commonly referred to as the nugget, is the highly stirred zone where the most material flow occurs. The typical microstructure zones of a weld are shown in Figure 4. If the process parameters during welding are not optimal, different defects can occur in each of these regions. Some of these defects include void formation, incomplete penetration, and particle alignment. [5] [10]

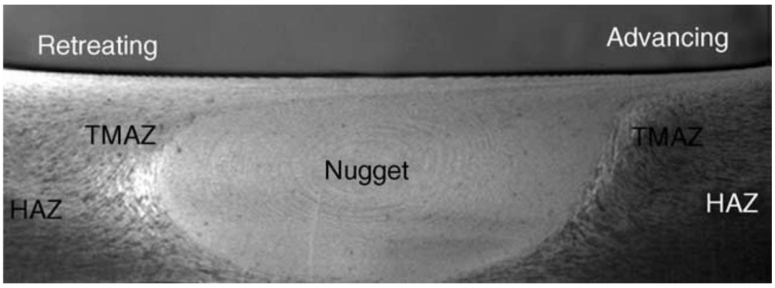
Retreating
Advancing
TMAZ
Nugget
TMAZ
HAZ
HAZ

Figure 4: Typical microstructure zones of FSW material. [10]

### 2.2.1 Tool Geometries

The geometry of the tool plays a very important role in the FSW process and many different types of tool setups have been developed throughout the years. This review will only focus on fixed shoulder and probe geometries, other options do exist, such as bobbin type tools, but are out of focus for this work. Shoulder geometries will be mentioned briefly, but the focus will be on probe geometries as probe geometry design is the focus of this thesis.

The two main purposes of the shoulder are to create/maintain frictional heat with the base material and to maintain enough forging pressure for welding while containing the heated material under the shoulder. The outer surface of the shoulder is typically cylindrical, but conical shapes have also been used. The external profile of the outer surface usually has no influence on the weld. The most common shoulder ends are flat, concave, and convex shapes. Usually the angle of concave and convex shoulders is quite low (between 6-10°). Different geometry features can be added to the shoulder face, regardless of shape, for more frictional heat generation or better material flow properties. Scrolls are the most common feature, but other options are used (Figure 5). [11]

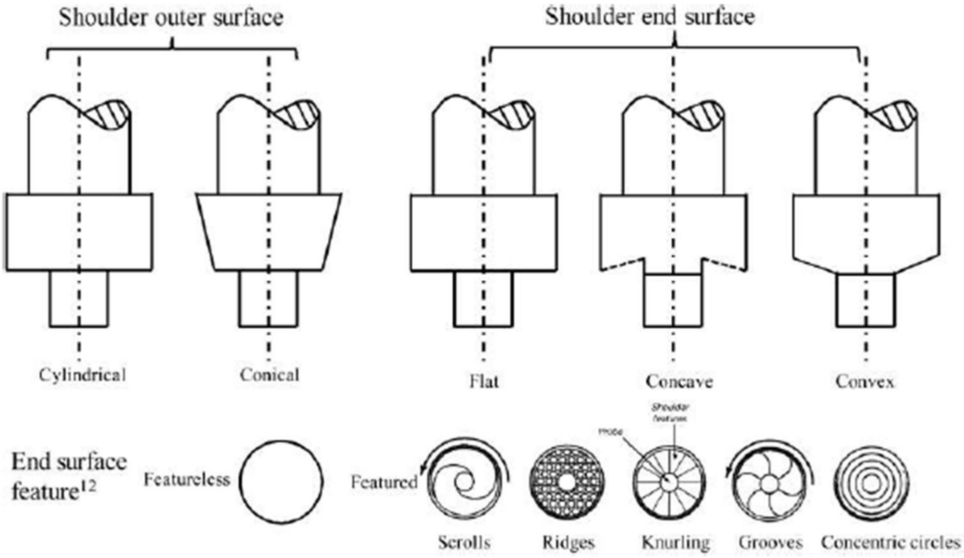

Figure 5: Different common shoulder shapes and features. [11]

The probe of the FSW tool deforms the base material by shearing material from the advancing side and moving that material to the retreating side. Some of this material may circulate multiple times around the probe, in the SZ, before being deposited somewhere behind the tool. At the same time, the probe also produces frictional and deformational heat. Figure 6 highlights some of the most common probe designs. Probes can to broken into two major categories, cylindrical and tapered, based on their side profiles. The tip of the probe is most commonly flat, but domed tips can be used to reduce probe stress during plunging. The trade-off with a domed tip is that the weld quality near the tip if often compromised compared to a flat tip and the cost of manufacturing is higher. [11]

A smooth cylindrical probe is possibly the simplest probe and is the easiest to manufacture. Cylindrical probes work well in thin plates, while threads, flutes, or more extreme features can be added to further increase their effectiveness. However, for thicker plates the efficiency of cylindrical probes decreases, as they require more machine power, higher rotational speeds, and lower weld travel speeds to make effective welds. Tapered probes can be more efficient when welding thicker plates. The taper on the probe also increased the pressure inside the weld zone, increasing the effectiveness down the length of the probe. Geometric features (threads, flats, flutes) can be added to increase the stirring ability or heat generation of the tapered probes as well.

Features such as threads and flutes may increase the effectiveness of the probe, but also often increase the stress in the probe and can be worn away during welding (mitigating their effect) or even cause total probe failures if the localized stress gets too high. [11]

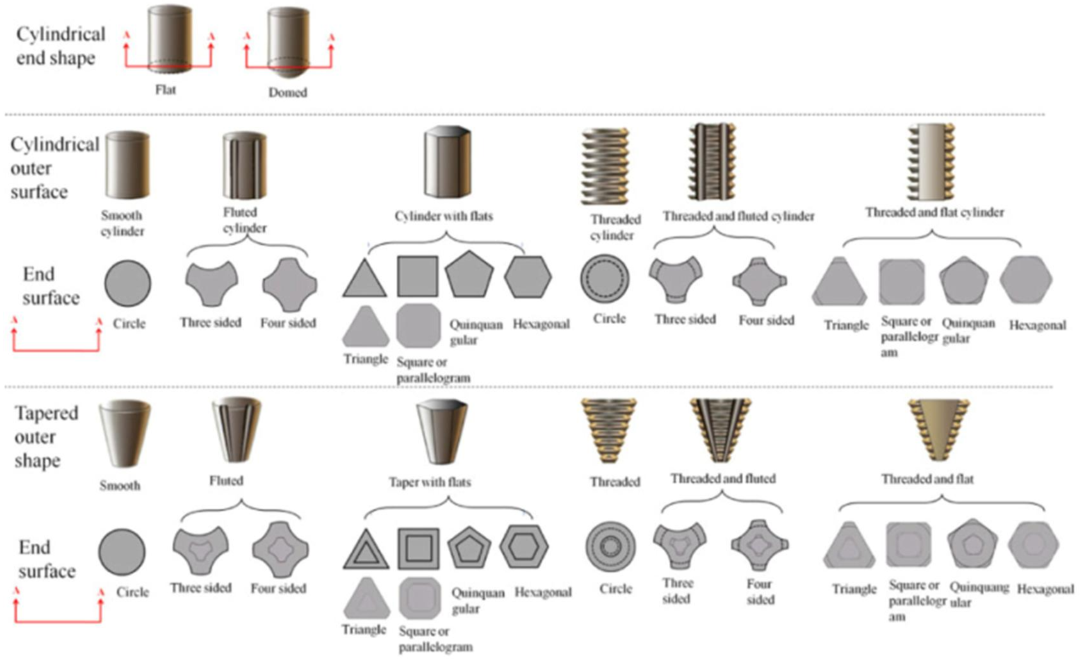
Cylindrical end shape
Flat
Domed
Cylindrical outer surface
Smooth cylinder
Fluted cylinder
Cylinder with flats
Threaded cylinder
Threaded and fluted cylinder
Threaded and flat cylinder
End surface
Circle
Three sided
Four sided
Triangle
Square or parallelogram
Quinquangular
Hexagonal
Circle
Three sided
Four sided
Triangle
Square or parallelogram
Quinquangular
Hexagonal
Tapered outer shape
Smooth
Fluted
Taper with flats
Threaded
Threaded and fluted
Threaded and flat
End surface
Circle
Three sided
Four sided
Triangle
Square or parallelogram
Quinquangular
Hexagonal
Circle
Three sided
Four sided
Triangle
Square or parallelogram
Quinquangular
Hexagonal

Figure 6: Different common FSW probe designs. [11]

While the traditional probes serve most applications well, welding of thicker materials requires more complex probe design. The Whorl$^{TM}$ type probes, developed by TWI, were designed to weld plates up to 60 mm thick. TWI accomplished this by increasing the swept volume of the probe (the dynamic to static volume ratio). Large left-hand threads were added to a tapered probe, which helped increase the forging pressure and material flow around the probe. This probe was further improved into the MX Triflute$^{TM}$ design, which made higher quality welds in thick materials over the Whorl$^{TM}$ type probe. [12]

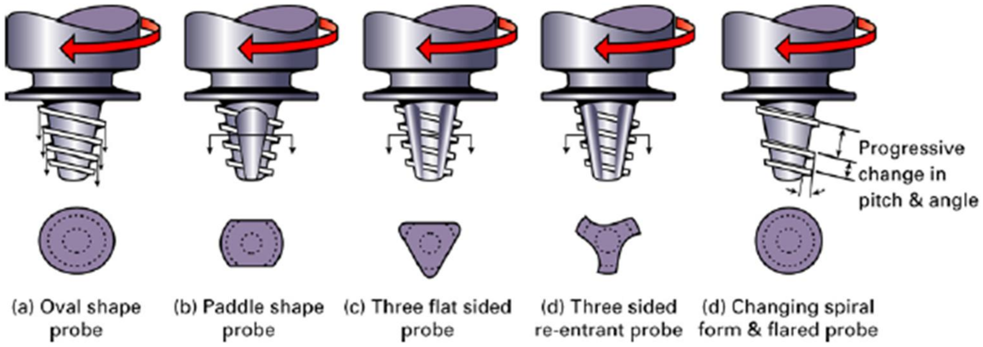
Progressive change in pitch & angle

(a) Oval shape probe (b) Paddle shape probe (c) Three flat sided probe (d) Three sided re-entrant probe (d) Changing spiral form & flared probe

Figure 7: Different variations of the Whorl$^{TM}$ type probe. [12]

The MX-Triflute$^{TM}$ probe design forms the basis of the probe jointly developed by SKB and TWI specifically for the purpose of sealing copper canisters. This process will be discussed more in the Canister FSW Tool Design (section 2.4) portion of this chapter.

## 2.3 FSW of Copper Canisters

The Swedish Nuclear Fuel and Waste Management Co (SKB) and The Welding Institute (TWI) initially developed the use of FSW for sealing 50mm thick copper canisters for nuclear waste disposal. Originally, SKB developed Reduced Pressure Electron Beam Welding (RPEBW) for the joining method, but viewed FSW as a possible alternative beginning in 1997. Posiva Oy developed conventional EBW parallel to SKB welding development.

Oxygen Free Phosphorous (OFP) Copper was chosen to be the canister material due to its high corrosion and creep resistance. Oxygen free copper was used because oxygen negatively affects corrosion resistance; oxygen content was required to be less than 5 ppm. Phosphorous was added to increase creep resistance, 30-100 ppm was doped into the alloy [7]. Other impurities, such as sulfur and hydrogen, were also limited by the EN 1976 standard for copper and copper alloys [13]. An 850 mm diameter cast ingot is the raw material for hot forming processes like extrusion, pierce, and draw methods [7, pp. 91-99]. Copper ingots for the lids and bottoms are hot forged [7, p. 110]. Copper plates are currently only used for weld tests (casted and hot rolled). The copper is formed into 1.05 m diameter tubes using a pierce and draw technique. The canisters can have three different lengths of 3.55 m, 4.75 m, and 5.22 m [7].

To begin the joining of the lid to the canister they are both installed into the custom canister FSW machine developed by ESAB, shown in Figure 8. Once the cylinder and lid are clamped in place, a pilot hole is drilled at the start of the weld to relieve stress on the probe during plunge. In total, the weld consists of five stages: dwell, start, downward, joint-line, and parking, (numbered in Figure 8). The beginning and end of the weld are above the weld joint line, this was done to minimize the risk of damaging the joint line during plunge, and to allow the exit hole to be machined off after welding is completed. [3]

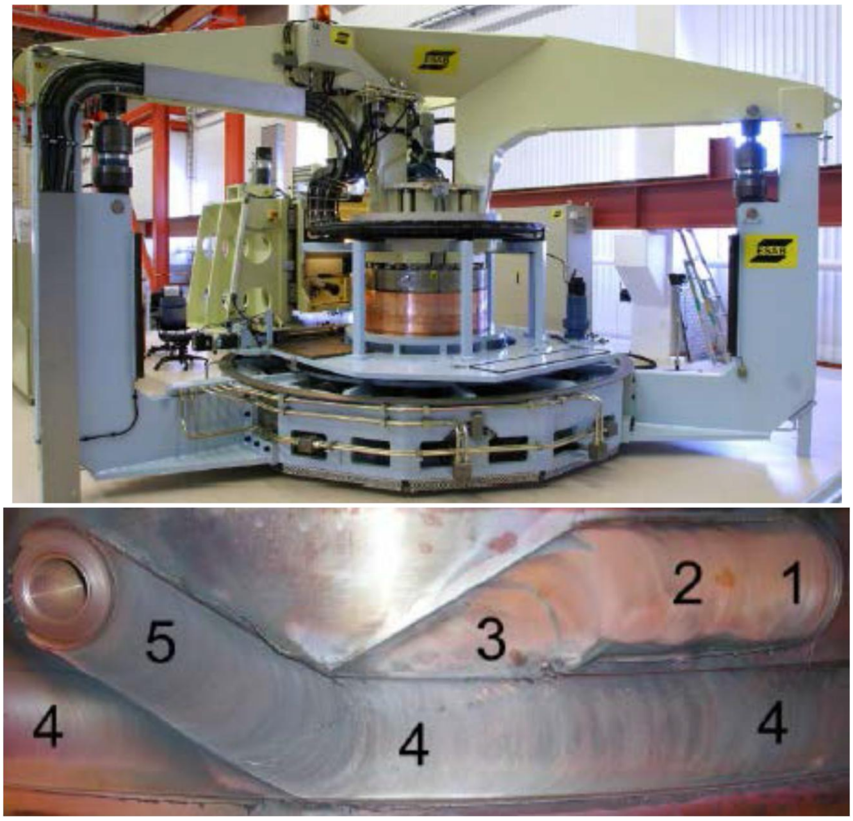

Figure 8: ESAB canister weld machine and weld process order. [3]

In total, the weld length is 400 degrees, or 3.7 m, and takes roughly 45 minutes to complete. The weld process is temperature controlled to maintain an average of 845±10 °C but the weld and rotation speed are approximately 82 $\frac{\mathrm{mm}}{\mathrm{s}}$ and 400 rpm (which are the values used in the simulations). During welding the weld speed is held constant, so the only control variables for maintaining temperature are the rotation speed and axial force. Argon shielding gas is used to protect the copper from impurities, especially atmospheric oxygen and hydrogen, during welding. Originally, the lid was to be used as a backing support for the axial load during welding, but this produced excessive flash so the joint was redesigned. The weld joint also serves as a centering mechanism for the lid, which leads to a more complex joint. After welding, 55 mm from the top and 5 mm from the side are machined off the canisters to remove flash and the entry/exit holes. Figure 9 shows the current weld joint lines and machining lines diagram. [3]

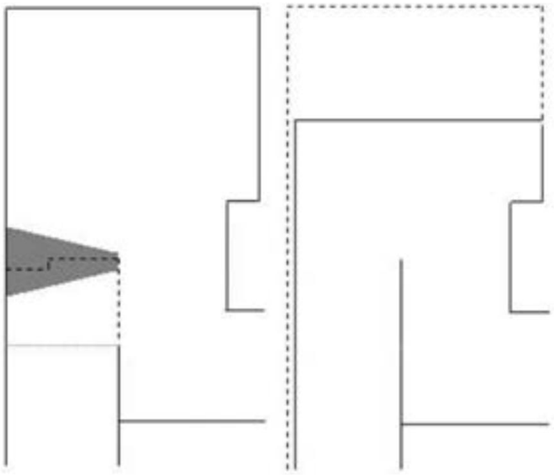

Figure 9: Joint line diagram for welding (left) and machining (right). The thin grey line on the welding joint diagram is the old weld joint line. [3]

The control system for the FSW process uses three thermocouples implanted in the probe and shoulder to monitor the temperature during the weld. The closed-loop cascade control system takes a weighted average of the temperature reading and can vary the spindle rpm or power input to maintain a temperature window of 845±10 °C. Figure 10 shows a graph of how the spindle rpm changes to maintain a relatively constant temperature throughout the weld and shows where the thermocouples sample the temperatures from inside the tool. [3]

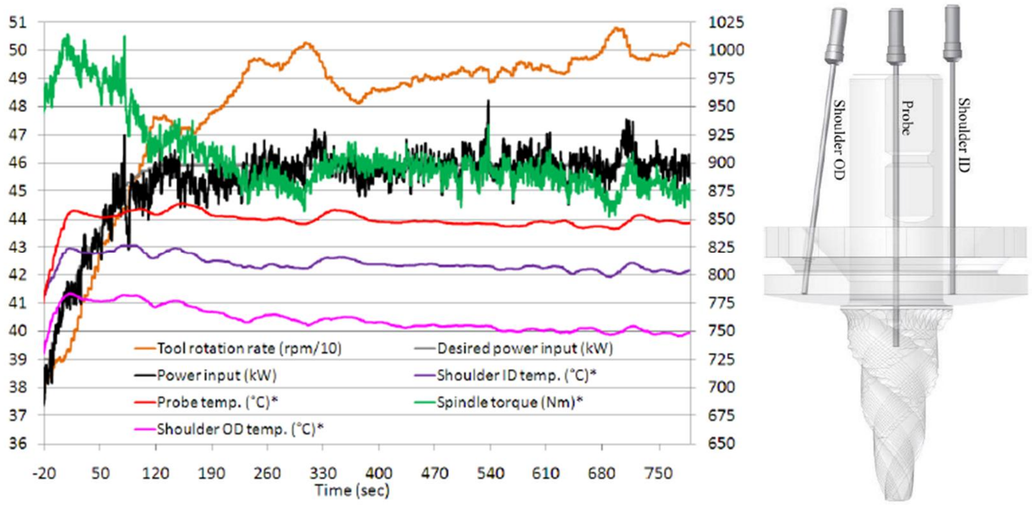

Figure 10: Representative FSW control system plot, *notes value on right y-axis; and diagram showing the shoulder outer diameter, inner diameter and probe thermocouple locations. [3]

## 2.4 Canister FSW Tool Material

Due to coppers high melting temperature, and high FSW operating range, a great deal of work has gone into R&D of a probe that can withstand the high temperatures and loads. The current material for the probe is a nickel superalloy Nimonic 105 with a chromium nitride (CrN) coating. The shoulder is a tungsten based alloy called Densimet D176. While the shoulder material is also important, it is outside the scope of this work, so the focus will be mostly on the probe development. It should be noted that while Nimonic 105 is the current probe material, it was observed that there were possible areas of improvement. It was simply the best the researchers found within the congruent development cycle of the FSW process, tool, and material back in 2004. Andrews' report mentioned that while there are likely better materials for FSW of copper available, Nimonic 105 had acceptable properties, was easily workable, and had an economical price. [14]

The criteria used by Andrews at TWI during the search for tool materials were:

- To have sufficient fracture toughness to survive the initial stage, or plunge sequence.
- To have adequate high temperature strength to withstand the high compressive and shear loads experienced throughout the weld cycle.
- To be economically viable to generate a probe geometry that provides sufficient friction heating and metal movement.
- The probe must not lose dimensions or shape when producing welds up to 3.5 m long.
- To be inert when welding copper.

This led to the exploration of 17 different materials in four families; cemented carbides, cubic boron nitrides, refractory metals, and superalloys. Cubic boron nitrides and refractory metals were not considerably developed due to underperformance and prohibitive costs, leaving cemented carbides and superalloys as the main alternatives. The first probes were made of a cemented carbide H10F, due to its accessibility and low cost. However, the probes proved prone to sudden fracture and rupture during the plunge and starting stage. Further development was done on these probes as the initial alloy was deemed too hard for the application. Two new alloys were used with lower hardnesses and were more successful. Nevertheless, trails with cemented carbides were ceased, namely due to the materials sudden fracture tendencies. Development of an acceptable cemented carbide probe was likely possible given enough time, but the development timeline did not allow for it. [14]

For the superalloys, three subcategories were considered, forged, cast, and powder metallurgy. While cast and powder based probes did successfully create 1.0 m welds, they were not developed further due to their brittle tendencies. This left forged superalloys as the most promising candidates. Four forged alloys were considered in the study done by Andrews, Nimonic 105, Nimonic 90, Inconel 718 and Waspaloy. All four of these alloys were able to create successful welds, but Nimonic 105 was the only one that did not show signs of twisting deformation during a 3.3 m weld. Hot shearing of the material caused this deformation and Nimonic 105 was the only alloy tested that showed no signs of deformation (hot shear) at 20 m of weld and 1000 °C. Within the constraints of the study, Nimonic 105 was found to be the best probe material, but it was noted that this was a limited study of possible materials and a better candidate likely exists and could be implemented with more R&D. [14]

Andersson and Westman conducted a second study at SKB on the most viable nickel based superalloys during the time Andrews was also researching probe materials. This study focused heavily on the creep rupture strength of the different alloys. Using 1000-hour creep strength, they created the chart seen in Figure 11 to evaluate the alloys. From this, they concluded that Inconel

Ma 6000, Nimonic 115, and Udimet 700 were the best options, with Nimonic 105 and Udimet 520 also being acceptable. Some cast alloys were also considered acceptable in terms of creep strength, but unpredictability in the cast structure made them less reliable for FSW applications. [15]

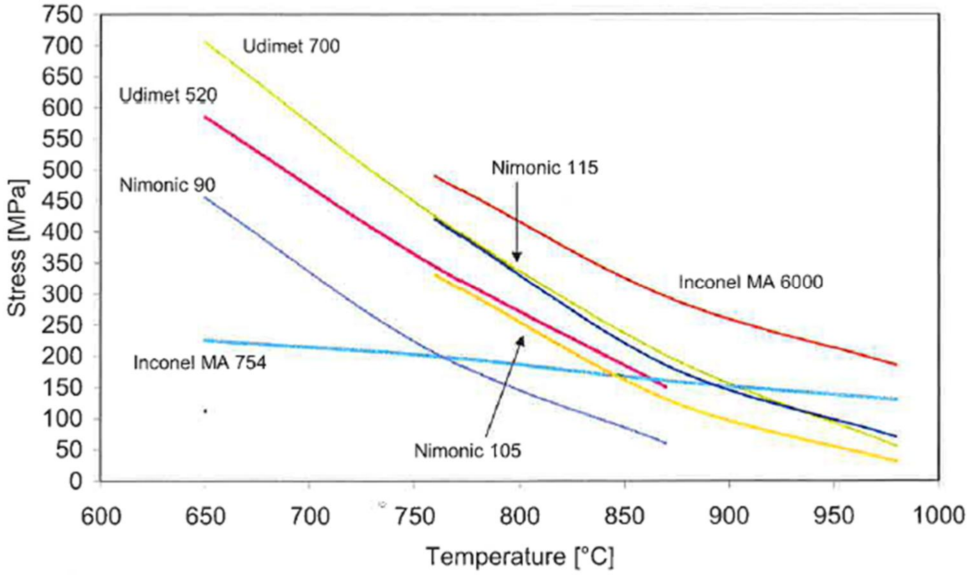

Figure 11: Superalloy 1000-hour creep rupture strengths. [15]

Westman noted some exceptions for the cast materials that had more reliable properties, these were cast alloys Inconel 738LC and Inconel 792 [15]. As part of a doctoral thesis, Savolainen developed useful probes made of Inconel 738LC and Inconel 939 (a different cast alloy) [16], [17]. It should be noted that Savolainen's thesis focused on the durability, reliability, and microstructural properties of FSW OFP copper, not probe development [16].

Later in SKB's probe development, Cederqvist added a chromium nitride (CrN) coating, applied by physical vapor deposition (PVD), to improve fracture toughness and crack resistance of the probe. TiN and AlTiN coatings were also considered, but CrN was chosen because it was the most inert when welding copper [3].

### 2.4.1 Material and Coating Microstructural Analysis

Recently (in 2015) Nenonen performed microstructural analysis of one used and one new probe; Posiva supplied these probes. His analysis focused on the structural comparison between the new and used probes of the Nimonic 105 base material and the CrN coating. Additionally, he reviewed materials alternatives for any possible advances, since the 2004 reports, which would allow for a better material choice over Nimonic 105. His review focused on the advantages and disadvantages the materials might have over Nimonic 105, plus the current market availability of the material alternatives. Table 1 is a summary of the selected material groups reviewed by Nenonen and a brief description of how they compare to Nimonic 105 [6].

Table 1: The material groups selected for review. [6]

| **Material group** | **Advantage in comparison to Nimonic 105** | **Disadvantages** | **Availability** |
|---|---|---|---|
| **Conventional powder metallurgy origin wrought nickel superalloys** | Better strength at elevated temperatures.<br>Mostly lower ductility, but some alloys, such as Astroloy has almost as good tensile elongation. | Fracture rate in some powder metallurgy alloys is unacceptable | Commercially available, but usually only in large batches |
| **Tungsten-Rhenium alloys and its composite with PCBN** | Excellent strength at elevated temperature | Fracture toughness might not be good enough for reliable performance.<br>High price. | Materials are commercially available and there are companies manufacturing customized tools for FSW applications |
| **Ni-Al-V**<br>[Mochizuki. 2013] | Better strength at elevated temperatures. | There is no data on ductility. | Research material, not commercially available. |
| **Co-Al-W**<br>[Sato. 2006]<br>[Ishida.2008]<br>[Sugimoto. 2013] | Higher strength above 800 °C. | The strength under 800 °C is lower than strength of Nimonic 105.<br>There is no data on ductility. | Research material, not commercially available. |
| **Co-Ni**<br>[Makineni. 2014]<br>[Makineni. 2015]<br>[Knop. 2014] | Better strength at elevated temperatures. | There is no data on ductility. | Research material, not commercially available. |
| **Ni-Ir**<br>[Nakazawa. 2015]<br>[Nakazawa. 2016] | Better strength at elevated temperatures. | There is no data on ductility.<br>Iridium is very expensive. | Research material, not commercially available. |

Nenonen found that new powder metallurgy alloys, (development of PM probes was stopped back in 2004 due to their fracture rate), have been developed to reduce their fracture rate. He identified Astroloy as one potential option. W-Re and PCBN (Polycrystalline cubic boron nitride) are very hard current FSW tool materials, but complex geometries might make them prohibitively expensive to manufacture. Some newly developed Ni and Co based intermetallic alloys, such as Ni-Ir, show promise as material options. The issue with these new materials is that data on their material properties (ductility, thermal stability, etc.) is limited and many of them are not commercially available. [6]

The material analysis Nenonen performed was compared to the 2002 report of Nimonc 105 and Nimonic 90 done by Westman [15]. The initial inspection included macroscopic analysis of the used probe. This analysis showed signs of a hairline fracture on the third MX feature (Figure 12), however, a fracture was never found in the prepared sample. Observation of the residual copper showed how the copper was flowing during welding. This showed a thin layer of copper pressed against the tip of the probe that remained stuck to the probe while the rest of the copper followed above it. The vertical stripes in the copper show how copper was flowing out against the tip in thin shear layers.

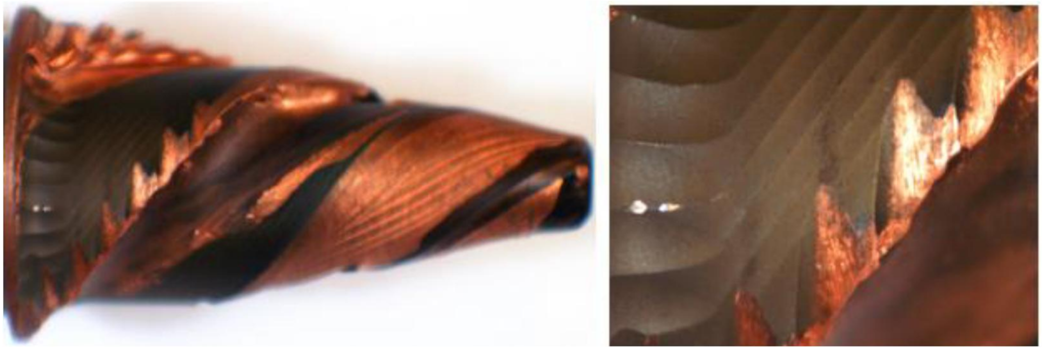

Figure 12: Used probe and evidence of a possible fracture trailing the MX feature. [6]

Microstructural analysis by Nenonen comparing the new and used probes confirmed the results of the study done by Westman [15]. The grain structures and composition of the Nimonic 105 were similar between the new probe, used probe, and Westman's results. It was found that the elevated heat and stress do not noticeably affect the microstructure of the Nimonic 105. The only noticeable difference between the new and used probes was a small, 10 µm thick, deformation zone under the coating layer on the used probe. However, the coating comparison between the two probes are quite different. Nenonen found inconsistent thickness in the CrN coating between probes, likely caused by imprecise PVD application. The average thickness of CrN on the individual probes was between ±2 µm but the new probe was 3.5 µm thick and the used probe was 5.0 µm thick on average. Nenonen found that along the leading edge of the flutes a layer of copper stuck to the probe and protected the CrN coating, while along the trailing edge the coating was worn thin or fractured. [6]

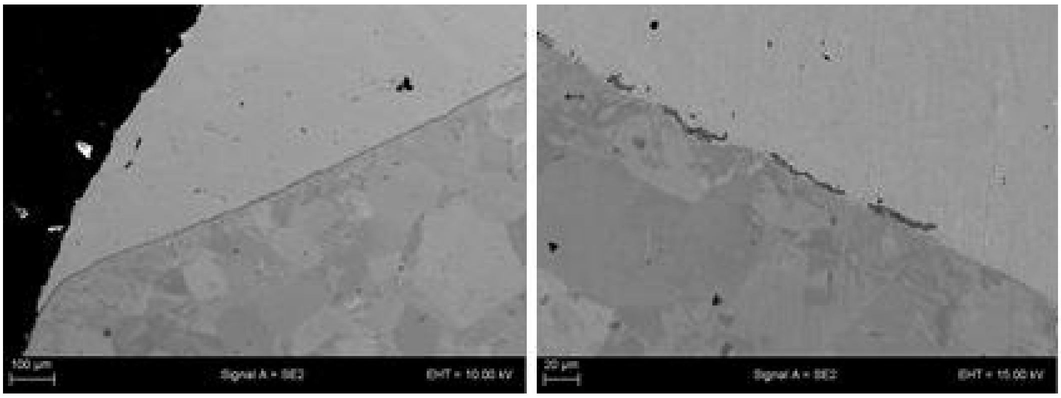

Figure 13: Leading edge protected CrN layer (left) and trailing edge damaged CrN layer (right). [6]

Close examination of the Nimonic-CrN-Copper boundary layer of a used probe revealed that the CrN layer had appeared to absorb some of the phosphorus from the OFP-copper; this is the lighter half of the CrN layer in Figure 14. Aluminum oxide ($Al_2O_3$) was also found in the Nimonic near the surface of the CrN (the small black dots in Figure 14), which is known to form on the surface of nickel-based superalloys at high temperatures causing increased brittleness. [6]

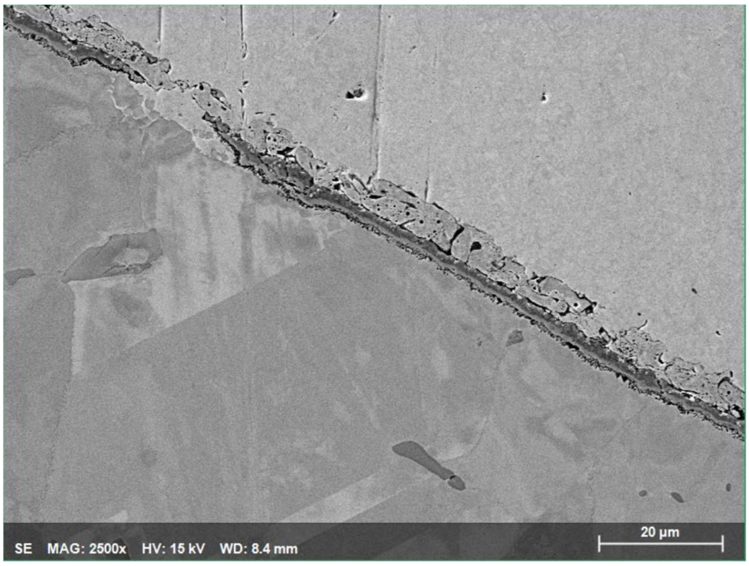

Figure 14: Damaged CrN boundary showing phosphorus absorption and $Al_2O_3$ formation. [6]

The findings in both the Nimonic 105 and CrN coating, along with the literature review of new candidate materials, led Nenonen to the same conclusion as Andrews. That while Nimonic 105 is an acceptable choice for the probe material, there are likely better options to investigate further. Some of these new materials include traditional powder metallurgy based alloys like Astroloy, Rene 95, and Udimet 720Li, or new nickel and cobalt based superalloys like Ni-Al-V, Ni-Ir, Co-Al-W and Co-Ni. A plan to test these new materials and compare their performance to the incumbent material, Nimonic 105, was proposed by Nenonen and forms the basis of the Low Cycle Fatigue (LCF) test developed in this work [6].

LCF is common when a material is subjected to a relatively high alternating stress, less than the ultimate tensile strength (UTS) but more than the endurance limit (which is the high cycle fatigue limit). LCF is even more common in materials at high temperatures, where local plastic deformation initiates crack growth, even if the global system behaves elastically [18]. High stresses and high temperatures are both common in FSW, making FSW tools susceptible to LCF failures. The test proposed by Nenonen, and developed in this work, is designed to characterize different probe materials performance in FSW and their susceptibility to LCF failure.

## 2.5 Canister FSW Tool Design

As with the material selection, the design of tool geometry was largely done simultaneously with the process development. This lead to an acceptable, but likely not ideal, geometry design for the probe. Initially a Whorl$^{TM}$ type probe (see Figure 7) was used to weld 10 mm thick copper. However, Whorl$^{TM}$ type probes would have been impossible to directly scale up to 50 mm thick copper, as the probe diameter would have become a prohibitively large 60 mm to maintain probe strength and stiffness. Around this time, TWI developed a derivative of the Whorl$^{TM}$ probe that facilitated the welding of thicker materials. The MX Triflute$^{TM}$ concept, represented in Figure 15, became the foundation of the probe geometry. While the MX Triflute$^{TM}$ concept allowed welding of thick copper, it needed improvement to eliminate some of its flaws. One persistent flaw during the design was a triangular shaped void on the advancing side of the weld, as seen in Figure 15. [14]

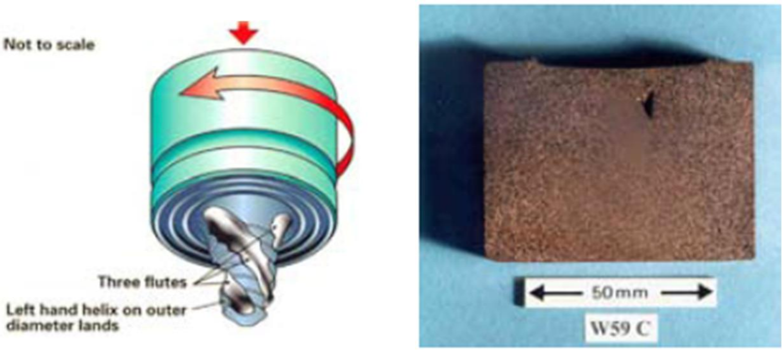
Not to scale
Three flutes
Left hand helix on outer diameter lands
50 mm
W59 C

Figure 15: MX Triflute concept and advancing side triangular flaw. [14]

Different variations of the Triflute$^{TM}$ design were developed and tested until a critical observation in the flute design led to a breakthrough. Examination of the probe flats revealed copper behaved less like a fluid at high temperatures compared to aluminum, for which the MX Triflute$^{TM}$ was originally designed. This led to copper not completely filling the flutes and leading to the void formation. Figure 17 shows examples of different probe designs; Figure 16 is a representation of the flute designs. [14]

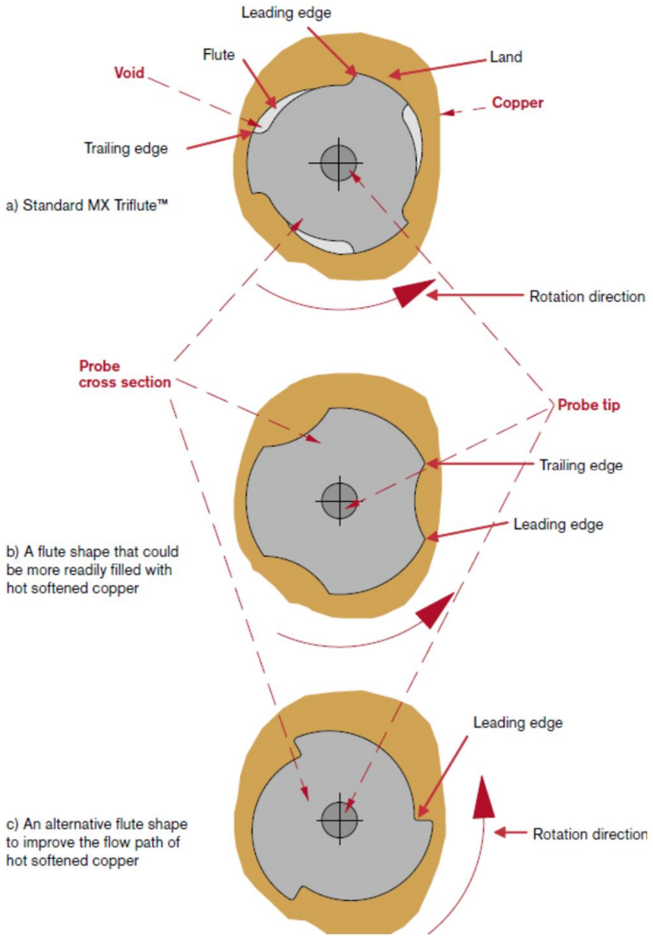
Leading edge
Flute
Land
Void
Copper
Trailing edge
a) Standard MX Triflute™
Rotation direction
Probe cross section
Probe tip
Trailing edge
Leading edge
b) A flute shape that could be more readily filled with hot softened copper
Leading edge
c) An alternative flute shape to improve the flow path of hot softened copper
Rotation direction

Figure 16: Standard flute design flaws and new flute design concepts. [14]

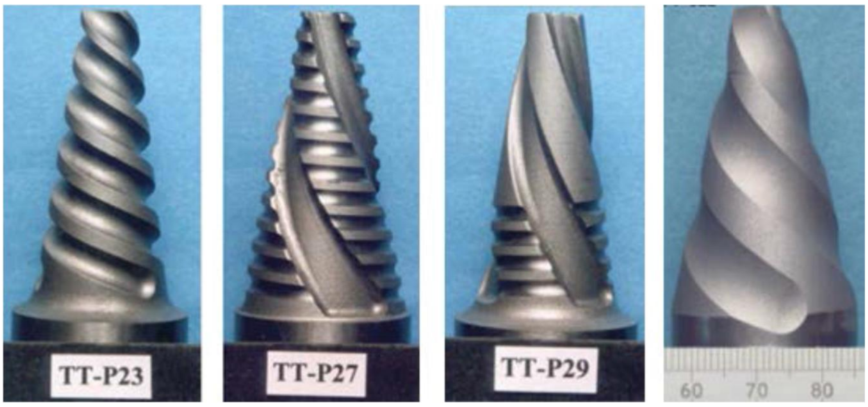

Figure 17: Early probe concepts. [19]

Continued work led to the A023 MK7 revision of the probe, which SKB patented [20], and became the working probe concept. Cederqvist further improved the probe and shoulder in 2010 by replacing the flat shoulder with a scrolled convex one and reducing the MX features on the probe. The shoulder was modified from a smooth concave shoulder into a convex shoulder with helicoidal scrolls. The convex shape enables reducing, or completely avoiding, the tool tilt angle, and the scrolls conduct the material inward, i.e., from the periphery into the center of the shoulder. The scrolled shoulder also allowed for more stable probe temperatures and minimal flash generation [21]. The reduction of the MX features from 35 mm to 17 mm of the probe length was a safety factor against probe fracture as the MX features are a stress concentrator. A version of the probe without the MX features was also tested, but the processing window was much smaller as heat generation was too low without the MX features. Figure 18 shows the A023 MK7 probe as developed by TWI and the improved current probe with a scrolled shoulder, reduced MX features, and CrN coating. [3]

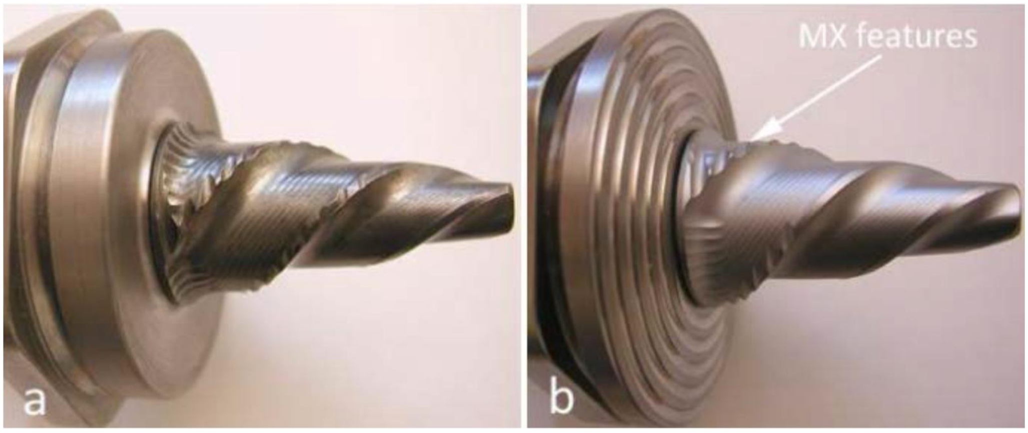

Figure 18: A023 MK7 probe as developed by TWI (a) and current probe design (b). [3]

### 2.5.1 Analytical Design Improvements

While the current probe does make acceptable welds, there may be room for improvement in probe life reliability and quality of the stirring zone made possible with design improvements. One of the larger issues is the poor mixing of material near the probe tip, namely due to the reduction in forging force caused by an increasing helix angle near the tip. Figure 19 highlights this problem on the probe and outlines the effects of this changing angle in the weld. This present design could also increase the risk of joint line mislocation, due to increased deflection of the probe tip from the changing force angle. High deflection of the probe also increases the bending stress in the probe, which reduces its life and makes it more susceptible to premature failure.

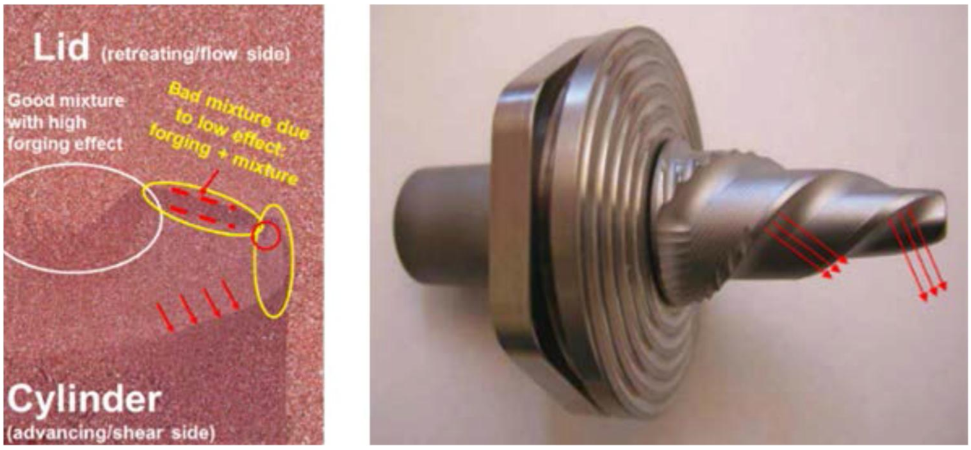
Lid (retreating/flow side)
Good mixture with high forging effect
Bad mixture due to low effect: forging + mixture
Cylinder (advancing/shear side)

Figure 19: Poor quality mixing of the weld and associated helix angle change.

Nenonen proposed an analytical method to improve the geometry of the probe using three evaluation criteria and the current probe design as the baseline [6]. These criteria were:

- The **static volume** of the probe is the amount of space (given in $mm^3$) the probe naturally occupies when it is stationary. A small increase of static volume is preferable for an increase of probe strength without increasing the forces instantaneously acting on the probe.
- The **dynamic volume to static volume ratio**. The dynamic volume of the probe is the amount of space (given in $mm^3$) the probe occupies during one full rotation, i.e. the swept volume. A higher dynamic to static volume ratio enables a bulk stirring effect with low instantaneous forces, which correspond to the static volume. The dynamic to static volume should be increased as much as possible for better a stirring effect if the static volume is able to withstand the instantaneous forces.
- The **contact surface area** of the probe (given in $mm^2$) is the sum of all the face areas that are exposed to the base materials to be welded; i.e. the sum of all the external 2D faces in the models. Increase of contact area surface should be minimal to avoid increases of drag loads.

Table 2 lists the values of these criteria for the original probe and their objective in new probe designs.

Table 2: Analytical probe design evaluation criteria. [6]

| **Parameters** | Static volume ($mm^3$) | Dynamic to static volume ratio | Contact surface area ($mm^2$) |
|---|---|---|---|
| **Values** | 13,320 | 1.22 | 3,144 |
| **Objective** | Small increase of static volume is preferable for increase of probe strength | Dynamic to static volume should be increased as much as possible for better stirring effect | Increase of contact area surface should be minimal to avoid increase of drag loads |

A small static volume increase to the probe could increase probe strength by adding more material to the core of the probe. This also would allow more material to be cut away in the flutes, increasing their size and effectiveness. Too large of a static volume is limited by other design constraints, the length of the probe cannot exceed 50 mm and the root diameter cannot change. Larger flutes would also increase the dynamic to static volume ratio, improving the probes ability to move material. However, large flutes can also increase impact loading and cause probe fatigue. This problem can be avoided with a better probe material, or careful manufacturing methods designed to keep stress concentration low. Contact surface area increases should be avoided if possible because a larger area of the probe contacting weld material increases drag loads. High drag loads can decrease the efficiency of the probe and increase the bending stress, which is detrimental to probe life.

In the final design proposals, tool type B was made in an attempt to mitigate the issues associated with the early designs. The final designs used a smaller angle at the tip from which is an improvement over the angle at the tip of the original. Four similar designs (A - D) were chosen as candidates for a new probe. Probe B was thought to be the most promising in terms of the criteria used to evaluate the designs, but this was difficult to validate without testing. [6]

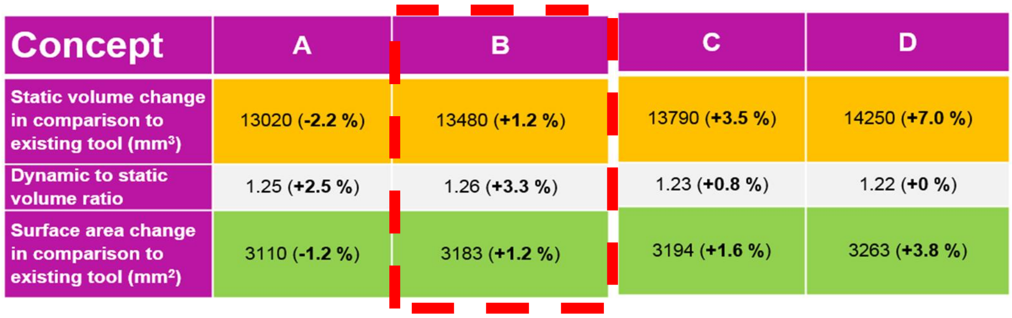

| Concept | A | B | C | D |
|---|---|---|---|---|
| Static volume change in comparison to existing tool ($mm^3$) | 13020 (**-2.2 %**) | 13480 (**+1.2 %**) | 13790 (**+3.5 %**) | 14250 (**+7.0 %**) |
| Dynamic to static volume ratio | 1.25 (**+2.5 %**) | 1.26 (**+3.3 %**) | 1.23 (**+0.8 %**) | 1.22 (**+0 %**) |
| Surface area change in comparison to existing tool ($mm^2$) | 3110 (**-1.2 %**) | 3183 (**+1.2 %**) | 3194 (**+1.6 %**) | 3263 (**+3.8 %**) |

Figure 21: New probe concepts analytical criteria evaluations. [6]

Manufacturing and testing of probe concepts is very expensive and is a major reason SKB stopped the probe development once they had a working probe. A large portion of this present work is to use simulations as a lower cost alternative to compare relative probe performance. The probe concepts listed in this section, along with the original probe design, are the probes used in creating, and evaluated in, the numerical model.

## 2.6 FSW Modeling

Most work, as typical of FSW, has been done in the modeling of FSW of aluminum. While the material properties are vastly different from copper, the modeling approaches are still valid. FSW is a highly complex process with many interconnected fluid dynamics, thermodynamics, and solid mechanics (stress, strain, etc.) phenomena. Accurately modeling every process at once is often an unrealistic task and many times the modeling approach is to focus on predicting key aspects of the FSW process instead of trying to characterize the process as a whole. While the main topic in this section is on the CFD approach to numerical modeling of FSW, some other methods do exist and will be briefly mentioned in this introduction. Many different techniques exist apart from the ones mentioned in this brief review including solid FEM, ALE, CEL, and Meshless methods. Microstructural modeling of the grain size of different weld zones is also an important modeling approach, but is outside the scope of this thesis. More thorough reviews of FSW modeling approaches and their respective results have been done and can be reviewed for more information on these topics [22] [23].

While not necessarily modeling of FSW, characterization of welds using microstructural analysis, tensile and bending tests, and hardness profiles are useful tools for determining the properties of the welds under different parameters and tool profiles. Savolainen did this specifically for OFP copper as part of a doctoral thesis at Aalto University [16]. Kumar and Raju tested different probe properties in copper welded with the same parameters [24]. Their study focused on the microstructural changes across the stirred zone, TMAZ, HAZ, and base material of copper welded with cylindrical (smooth and threaded) or polygonal pins. They found that the square probe created welds with the best mechanical properties, based on hardness and tensile tests, due to the high dynamic to static volume ratio and pulsating effect caused by the pin geometry [24]. A few years later Cartigueyen and Mahadevan completed a similar study with copper and found similar results with hexagonal and square pins. They found that smooth cylindrical and triangular pins were unable to complete successful welds due to low heat generation [25].

Tracers and markers inserted into the base material is another useful tool for modeling FSW. This process involves taking dissimilar material and placing it in the path of the weld tool to analyze the before and after locations of the tracer material. One problem with this method is tracer material can change the properties of the base material and it can be difficult to observe dynamic weld phenomena. Schmidt et al. used 0.1 mm copper foil as a tracer to observe the flow patterns of AA2024-T3 butt welds [26]. They used X-ray imaging plus 2D and 3D computer tomography (CT) images to show the position of the copper foil in the weld. The foil was placed both parallel and perpendicular to the weld direction. This information was used to predict the size and shape of the stirred zone and shear layer as well as flow characteristics in the flow zone [26].

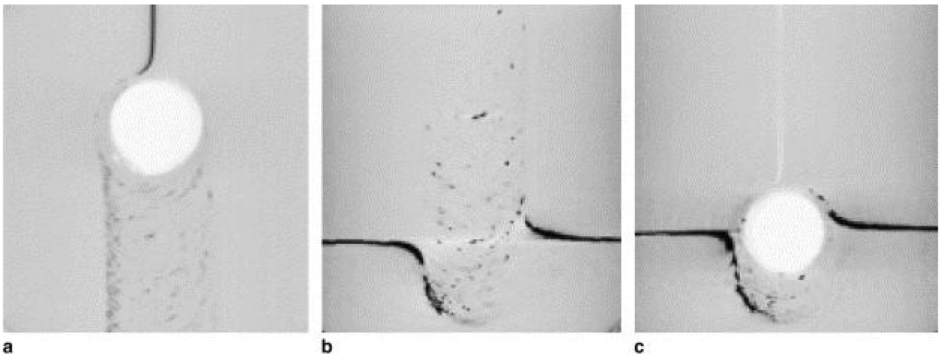

Figure 22: 2D CT images of tracer material at weld mid-plane: (a) tracer is parallel to weld; (b) tracer is perpendicular to weld; (c) perpendicular tracer with weld stopped at the tracer line. [26]

Källgren used a tracer technique with brass rods interested into OFP copper in parallel and perpendicular orientations to the weld. This was combined with a particle tracking FEM model that tracked the movement of discrete points as a conical spinning probe moved through them [27]. Similar to Schmidt's method, the tracers were used to model the size and shape of the stirred zone. Figure 23 shows how a 52 mm long brass rod inserted into the weld path was used to predict the size and shape of the weld nugget of a 50 mm long probe. Results such as these were compared to the predictions done by the FEM model, as seen in Figure 24. Overall the results between the brass tracers and the FEM model match quite well, it is only near the shoulder where the model over predicts how far back the brass particles are pushed [27].

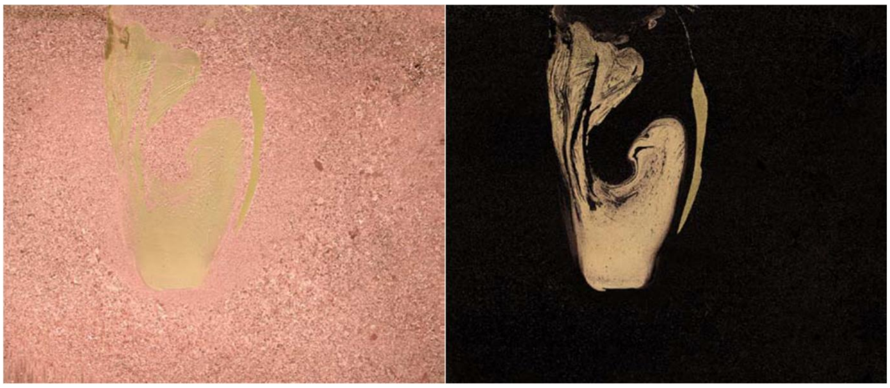

Figure 23: Brass rod modeling the shape of the weld nugget. The brass was inserted in line with the probe and parallel to the weld path: (left) original image; (right) copper darkened. [27]

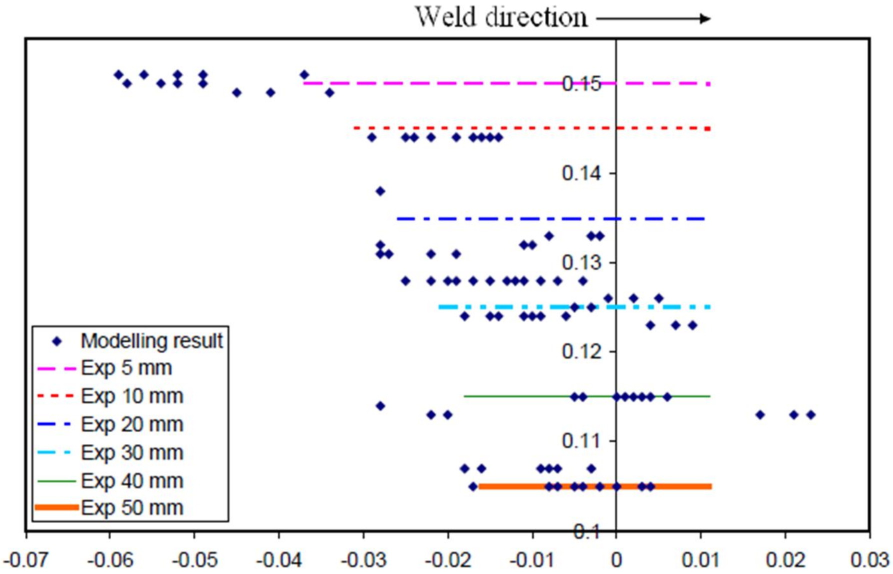

Figure 24: FEM tracer predictions compared to where brass was actually found in weld. [27]

### 2.6.1 General Numerical Modeling

Numerical modeling of FSW attempts to predict key weld phenomena, like material flow properties or void formation, without the need for experimental trails. In 2005, Colegrove and Shercliff developed a 3D, steady-state model using the CFD software package Fluent [28] (an earlier version of the software used in this work). Their work modeled a threaded pin profile in a Rotating Reference Frame (RRF) using a strain rate and temperature dependent material model based on the Shepperd-Wright flow stress [29]. The mesh used is purely static and, while not the most complex model in terms of variable conditions, this approach has been heavily used since. In this model all heat generation was assumed to be caused by viscous dissipation and the material was assumed to completely stick to the probe. They found that this model greatly over-predicted the size of the deformation zone and heat generation but said these issues could be resolved by using a material slip model and by changing the viscosity model near the solidus temperature [28] .

Nandan et al. developed a model very similar to the one created by Colegrove and Shercliff. This model was used for simulating FSW of aluminum alloys [30] and mild steels [31]. The primary difference was the addition of a tool/material interface to define the frictional heat generation and material slip on the probe surface. Frictional heating was determined using a source heat input based on the material properties and a constant “sticking coefficient”. The method was similar to the analytical method of determining the proportions of heat generated by sliding/sticking material proposed by Schmidt [32]. This improvement allowed for a more accurate representation of the temperature fields, with the predicted and experimental temperatures through time matching very well [30] [31]. Through improvement and optimization of this model, Nandan found that four highly sensitive parameters greatly affect the temperatures and torques of the tool. These parameters were the friction coefficient, the extent of slip between the tool and the workpiece, the heat transfer coefficient at the bottom of the workpiece, and the extent of viscous dissipation converted to heat [33].

Ji et al. [34] simulated the effects of different tool (shoulder and probe) geometries using a refined version of Colegrove and Shercliff’s model. Their model converts the hyperbolic sine model into its natural logarithm equivalent and improves the mesh region divisions. They used their model to test the effects of different shoulder geometries and pin thread profiles. Chen et al. [35] created a transient simulation using a similar tool/material boundary to Nandan's model. This model allowed the development of the temperature and flow fields to develop through time once near steady state. They also improved the simulation accuracy by adding temperature dependence to more properties in the material calculation domains. Su et al. [36] developed a model using the same flow stress equation (Shepperd-Wright) but used an additional term to modify the equation near the melting point of the material. They also used a new method of calculating the tool/material boundary and used it to compare a conical probe to a "triflat" design. Their model calculated a constant frictional coefficient and material slip rate on the probe surface then used these values to influence the flow stress and volumetric heat generation.

### 2.6.2 Copper Numerical Modeling

Compared to the large amount of work done on modeling FSW in aluminum, very little work has been done for modeling copper specifically. As part of a doctoral thesis in 2010, Källgren produced multiple models for material flow and temperature distributions of 50mm thick copper [27]. This work was done with the assistance of SKB (and others), and is closely related to the work done in this thesis. These models used a discrete tracer technique to track material flow; the material was modeled as a shear and temperature dependent non-Newtonian fluid using EQ 1 to define the viscosity [27].

$$\eta = \eta_0 \dot{\gamma}^{-\beta} \exp\left[ \frac{2 v_m \zeta_0 / k_B}{T - T_0 + \sqrt{(T - T_0)^2 + \frac{4 v_a \zeta_0}{k_B} T}} + \varphi \right] \tag{1}$$

To model heat input, both a 2D and 3D version of Rosenthal's steady state general plate solution were used [37]. These models assume a constant heat source moving at a constant speed, and calculate heat transfer through the material accordingly. The boundary between the TMAZ and HAZ was modeled by finding an equilibrium between the shear strength of the material and the shear stress around the probe. While these models predicted the thermal zones quite well, one of its major limitations was the simplification of the tool geometry to a simple conical shape. This limited the flow direction around the probe to mostly rotational. This allows for a somewhat accurate prediction of the stirred zone, with some over-prediction of the size near the shoulder, but eliminates the flow characteristics caused by complex geometry features.

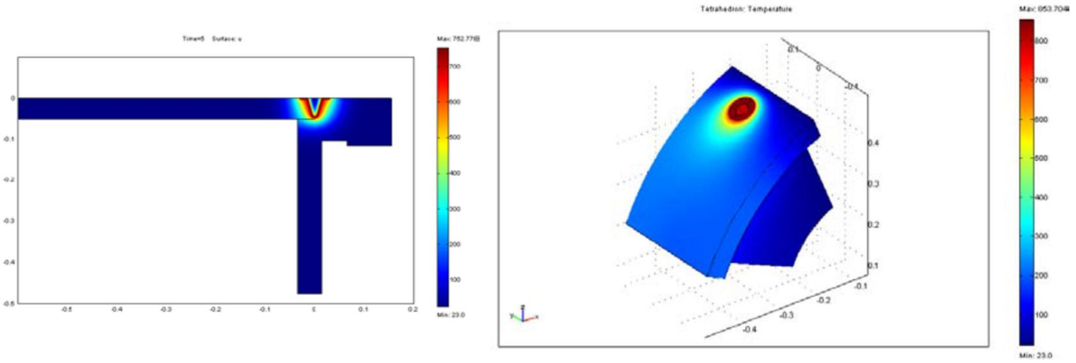

Figure 25: 2D and 3D thermal model of canister FSW. [37]

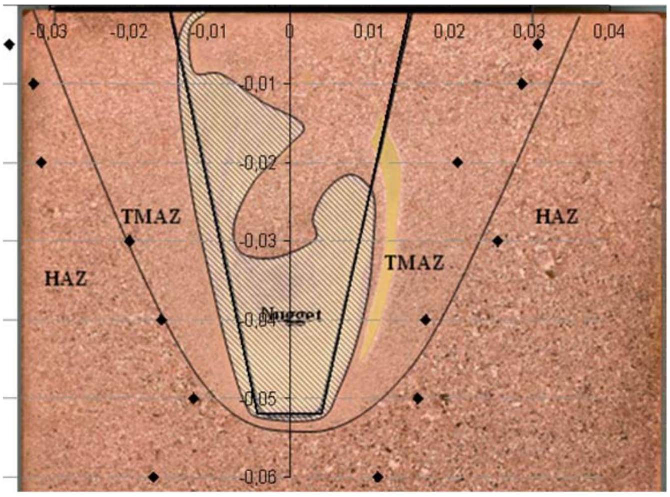

Figure 26: TMAZ and HAZ boundary by shear stress to shear strength balance. Black dots are the modeled points and black line is the observed HAZ/TMAZ transition. [27]

Pashazadeh et al. modeled temperature fields, effective plastic strain distributions, and material flow properties in copper sheets using DEFORM-3D software [38]. They used an Arbitrary Lagrangian Eulerian (ALE) technique and particle tracking to predict the size and shape of the stirred zone while also measuring the average particle speed to show the fluid velocity in the region. The material model was assumed to be a rigid-viscoplastic (common in metal forming FEM) with adaptive remeshing to prevent distortion. Overall, the model predicts the shape of the stirred zone quite well, and shows reasonable temperature distributions. The model also showed a reduction in hardness in the HAZ due to annealing from the FSW heat, and very high values of plastic strain on the advancing side near the surface of the probe [38].

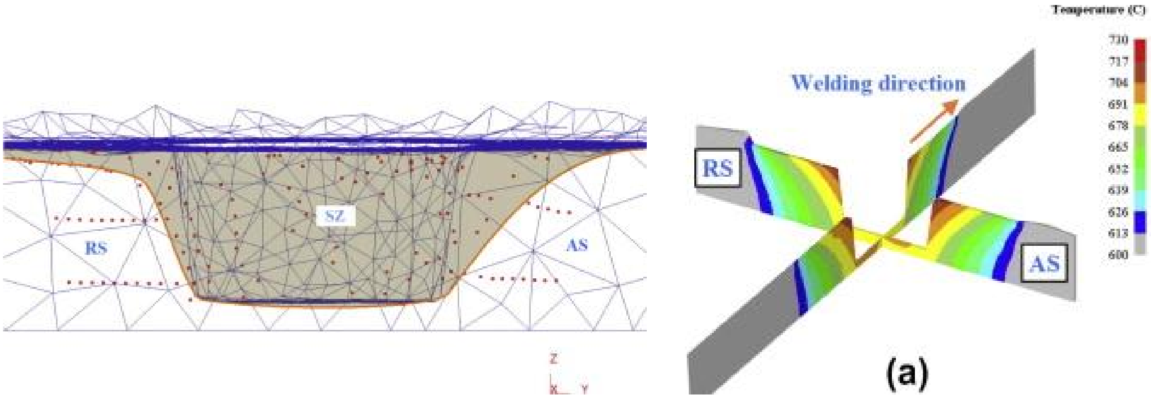

Figure 27: Stirred zone size based on particle tracking (left), and temperature contours (right). [38]

Some work has also been done in the modeling of copper to aluminum dissimilar FSW. Hadi et al. created a 3D model, using particle tracking in Comsol, that modeled the effects of welding copper to different aluminum alloys [39]. This model uses the Shepperd-Wright hyperbolic sine flow stress [29] to determine a strain rate and temperature dependent viscosity of both materials. Energy is modeled by a modified sticking-sliding Coulomb model dependent on contact conditions of the probe and shoulder, originally proposed by Schmidt et al. [32].

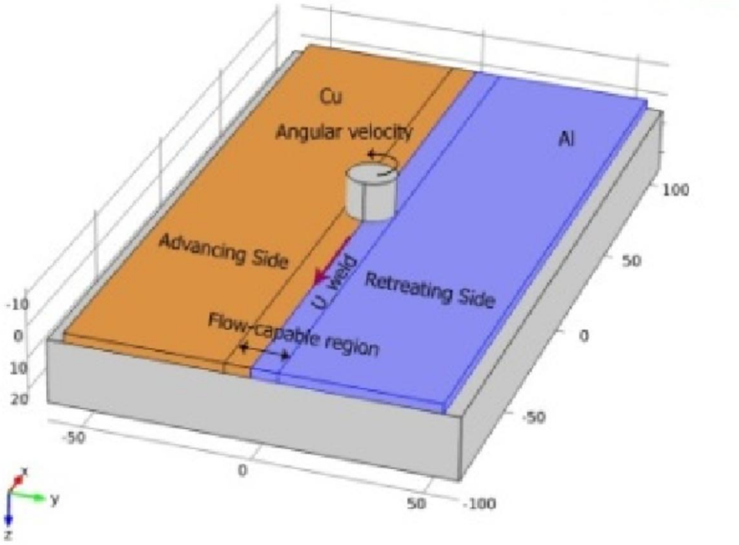
Cu
Angular velocity
Al
Advancing Side
U_weld
Retreating Side
Flow-capable region
100
50
0
-50
-100
-10
0
10
20
-50
0
50
x
y
z

Figure 28: Hadi dissimilar material (Cu-Al) fluid and solid modeling domain. [39]

This model focused on predicting the mixing of the two materials and their working temperatures at different tool offset positions. Both materials (aluminum alloy and copper), the probe, and a backing plate were all meshed and modeled; this allowed for accurate heat transfer prediction and good resolution to compare changes in temperature due to probe offsets. Particle tracking from the joint line was the primary way material mixture was measured between the two plates. As with the temperature, the particle tracking showed variations in the mixing ability tied to the offset of the probe. [39]

# 3 Numerical Modeling Approach

## 3.1 Introduction

Ansys Fluent was the CFD software used in this work. Similar to many other works, this model is based purely in an Eulerian reference frame. This reference frame calculates all variables from static control volumes and allows fluid to pass through these volumes freely [40]. This is different from the Lagrangian method of tracking discrete cells that move with the fluid. Figure 29 demonstrates the difference of how both methods would calculate material movement across one time increment; notice how mesh remains fixed and the material points move in the Eulerian method while the mesh nodes move with the material points in the Lagrangian method.

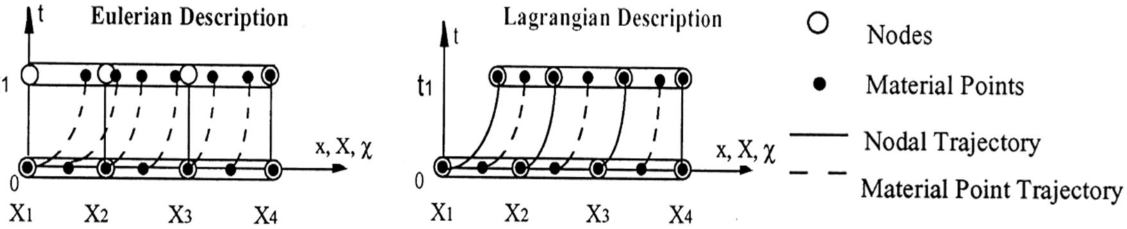

Figure 29: Eulerian vs. Lagrangian computational methods. [40]

Eulerian domains tend to be more stable, but require larger computational areas than Lagrangian domains. Eulerian domains are also inherently limited by their static nature when trying to simulate highly deformed fluid domains. However, Lagrangian domains have a tendency to create highly distorted and unstable meshes when subjected to extreme deformation conditions. These extreme conditions are common in FSW applications and simulations, so, purely Lagrangian methods are typically not feasible. Techniques have been developed to stabilize the Lagrangian method; Arbitrary Lagrangian-Eulerian (ALE) and Coupled Eulerian-Lagrangian (CEL) are two of them.

The reason an Eulerian mesh was chosen over a more complex technique like ALE or CEL was because those methods use much more processing power and tend to limit the size of the simulated domain. It was determined to be more beneficial to simulate a full-scale probe, with a complex geometry and material model using a simpler, and more stable, computational domain.

Due to the size of the simulation, a dedicated high-power PC was used for all calculations. This allowed the simulations and models to be developed on a standard PC and then imported to a more powerful system for dedicated computing. The specifications of the computing machine are as follows:

- (2X) Intel Xeon X5680 CPU @ 3.33 GHz (12 processors each), 24 total processors
- 1.5TB internal storage, with 1 TB remote storage
- 32GB dedicated RAM with an additional 32GB available (64GB total)
- Nexus RX-1.1K 1100W power supply
- Windows 7 Enterprise operating system

The model was set up to be somewhat modular, allowing different probe geometries to be easily interchanged and simulated. As long as the proportions of the probe (length, root diameter, etc.) remain relatively unchanged, the base geometry and mesh of the model can be adapted to new probe designs with very little effort. This was an intentional design choice that allowed the creation of a quasi-assembly line where meshes for models of different probe designs could be quickly created (typically in less than 20 minutes), and then exported for processing on the dedicated high-power PC. Duplicates of every geometry, mesh, and simulation results files were organized such that they could all be accessed from the same Workbench (Ansys's project management program).

## 3.2 Geometry and Mesh

A 3D model of the original probe and 3D models of some possible alternatives were previously created using CREO Parametric [6]. These models were converted into generic .STP files for import into the ANSYS Workbench geometry modeling system DesignModeler. The fluid domains were all created in DesignModeler due it its update linking ability with the Ansys Meshing software, allowing automatic updates between the geometry and mesh. The entire simulated domain was built with DesignModeler parametric tools and then the .STP probe models were imported as simple geometry files. This import of the probe model caused the 3D modeling history of the probes to be lost, meaning that the probe could no longer be edited once imported into DesignModeler. All edits to the probe design would have to be done using CREO Parametric and a revised .STP file would have to be created for import into DesignModeler.

Once the probe geometry was imported, it was centered in the rotating region (RR) of the simulated domain. The RR is the portion of the domain that will move using the sliding mesh technique (discussed in the next section). The RR is the grey region of mesh in Figure 32 and Figure 33, which includes both the shoulder and probe geometries. This entire region is a 50 mm tall axisymmetric cone (probe) with an 80 mm diameter cylinder on top (shoulder). This region approximates the highly stirred zone around the probe and is required to use the sliding mesh, as the actual complex probe geometries are not axisymmetric. Axisymmetry is required so that the RR mesh always remains in contact the meshes from the other regions and no gaps are created during any point in time or position of the sliding mesh. This region is designed to be as small as possible in order to maximize the probe geometry effects, instead of having the RR move most of the fluid, with the boundary only 0.5 mm from the probe outer surfaces (and shoulder surface). A simple Boolean subtract creates a negative of the probe geometry in the RR, as seen in Figure 30. This becomes the walls of the probe that interact with the fluid moving in the RR, creating complex 3D material flow.

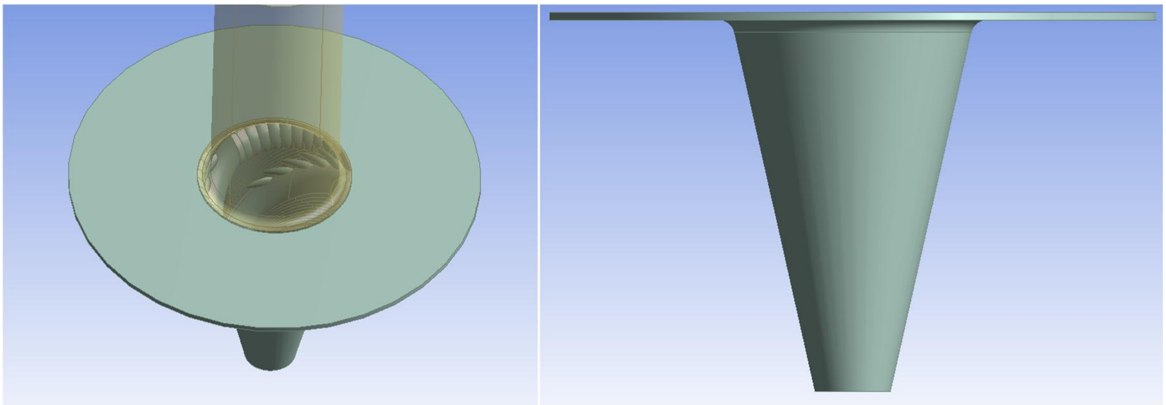

Figure 30: RR region with probe negative (left) and RR side view (right).

The model geometry consists of six individual regions, but only four separate parts. The distinction between parts is important when meshing interface zones between separate parts. Manual interfaces are not needed between different regions of the same part, but have to be defined at the contact between different parts. Figure 31 highlights the six different regions. From the probe outwards, there are the rotating region (RR), inner, middle, outer, and fluid. Including the probe, these are the six geometry regions, but, the outer and fluid regions are combined into one part, and the probe solid geometry is suppressed when meshed, leaving the remaining four parts. The overall size of the simulated domain is a rectangle with dimensions 600 x 300 x 100 mm. The global origin is located at the center of the probe tip.

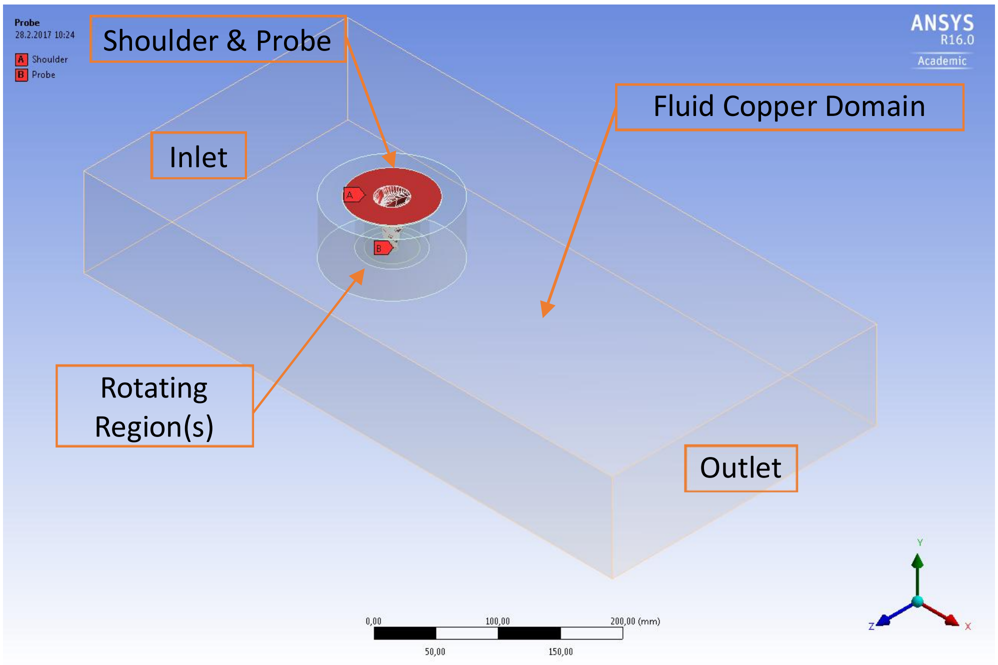
Probe
28.2.2017 10:24
A Shoulder
B Probe
Shoulder & Probe
ANSYS
R16.0
Academic
Fluid Copper Domain
Inlet
A
B
Rotating Region(s)
Outlet
Y
Z
X
0,00
100,00
200,00 (mm)
50,00
150,00

Figure 31: Geometry regions within the computational domain.

The mesh was created using the Ansys Meshing platform and is comprised almost entirely of unstructured tetrahedral elements, with the exception of boundary layers. Due to the size of the simulated domain and the complexity of the probe geometry, a large number of elements were needed to create a stable simulation. The mesh is focused around the probe and in the fluid near the RR. The definition of multiple regions in the geometry allow for more precise control over the mesh quality within each region. A very fine mesh was used in the RR and on faces where the RR met other regions (inner, middle, and outer). A very thin boundary layer of triangular prism elements was included on the probe faces to improve accuracy and stability of the near field elements. In total, the simulation contains between 1-2 million nodes and 3-5.5 million elements, depending on the final mesh criteria and probe geometry.

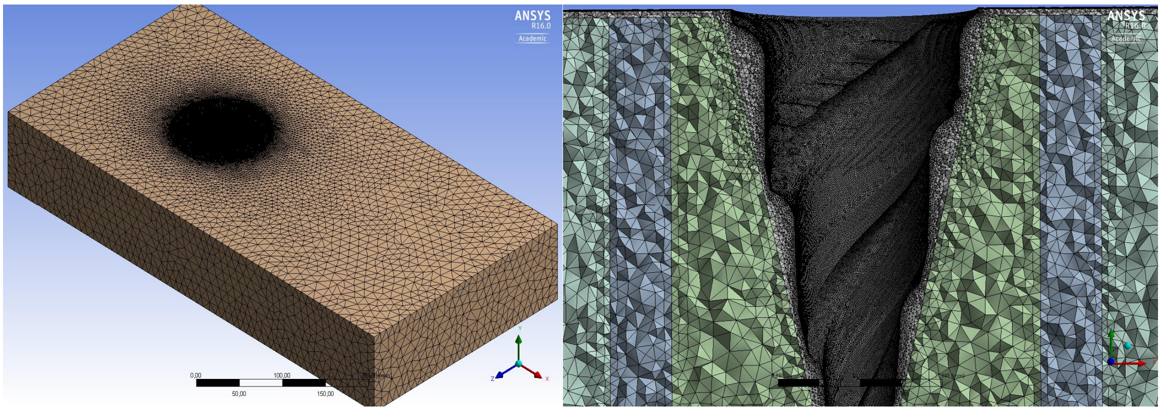
ANSYS
R16.0
Academic
0,00
100,00
50,00
150,00
ANSYS
R16.0
Academic

Figure 32: Global mesh (left) and RR fine mesh (right).

Away from the probe the overall size of the mesh gets quite coarse, as a method of reducing the size of the simulation away from the relevant probe zone. The global maximum element size in the fluid domain is 10 mm and it makes up a relatively small amount of the total mesh count, Table 3 shows each region’s element count and its average percentage of the total mesh elements. As seen from the table, the RR has over 2/3 of the total mesh count. The outer, middle, and inner regions have a maximum size limit of 4 mm, which makes them more precise than the fluid region but much lower than the RR.  The RR has a global maximum size of limit of 1 mm, making it roughly 10 times more precise than the global fluid mesh.

Table 3: Approximate mesh element count divisions per simulated region.

| Region | Element Count | Percentage of Total |
|---|---|---|
| Fluid | 250,000 | 6.1% |
| Outer | 550,000 | 13.3% |
| Middle | 200,000 | 4.8% |
| Inner | 295,000 | 7.2% |
| Rotating Region (RR) | 2,810,000 | 68.6% |

In order to capture the complex geometry of the probes, a face-sizing rule was added to all surfaces of the probe in the RR. A maximum element size of 0.2 mm was established on all faces of the probe and a 0.2 mm boundary layer was added over this surface.

Mesh stability is another reason why the size of the mesh needs to be precise in the RR (and other regions too, but the requirements are not as rigid in those regions). The quality of the mesh determines both the accuracy and stability of the simulation. Distortion of the elements negatively influences the mesh quality and can lead to errors in the simulation results, or even complete divergence of the simulation if the mesh distortion is high enough. There are many metrics used to determine the mesh quality, but some of the primary ones are skewness, smoothness, and aspect ratio, as seen in Figure 34. The aspect ratio is the length of the longest cell side to the shortest; an aspect ratio close to one is the most desirable. Smoothness is the measure of how a cells size compares to its neighboring cells. Ideally, a cell should not change its size by more than 20% of its neighbor. Skewness is the measure of how a cells actual volume compares to its ideal volume. For tetrahedral elements a skewness of zero means the element has the same volume as a perfect isohedron, which is ideal. A skewness close to one means that the element has very little volume relative to the size of its faces and this can lead to localized errors and mesh instability (Figure 34).

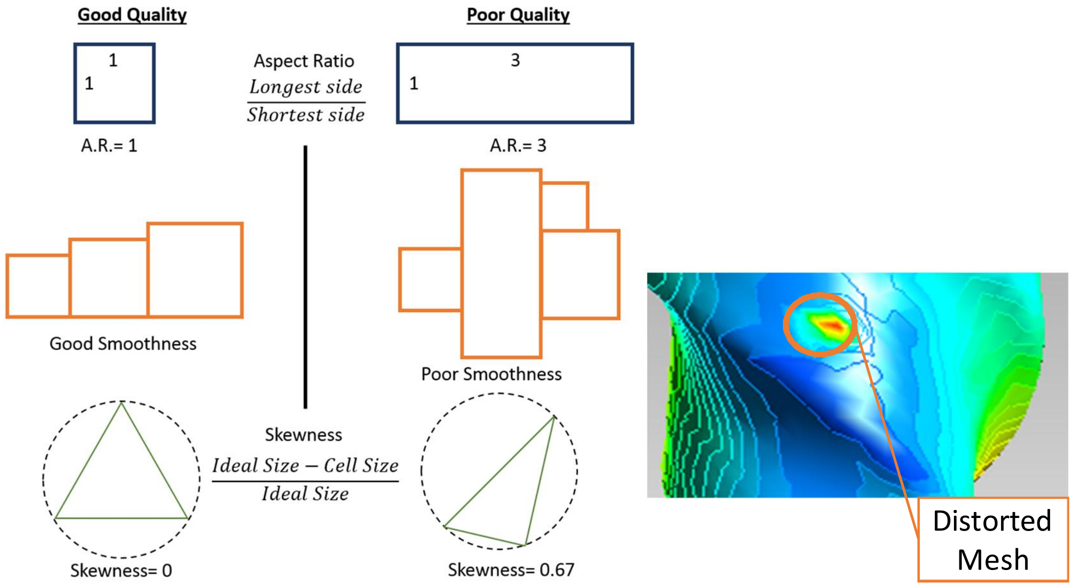

Figure 34: Mesh quality criteria and errors in results caused by low quality mesh elements.

### 3.2.1 Interfaces and Solid Walls

In Fluent the contact between different regions and parts has to be defined. The options available for this are conformal interface, nonconformal interface, inlet/outlet, and wall (also periodic, symmetrical and others not applicable to this simulation). Fluent automatically defines, and meshes, contacts between different regions of the same part as conformal interfaces. This allows the definition of different conditions in these multi-region parts but good accuracy when calculating the interface between them. Each part can be defined as a fluid or solid region prior, or post meshing, but the interfaces between contacting parts has to be defined before meshing for a conformal mesh to work. No solid regions are defined for this model; walls bound all fluid-solid contacts so no meshed solid regions are required. Walls are simply used to define the boundaries of the simulation; fluid is not allowed to pass through walls and must flow around them according to the boundary conditions defined.

All probe and shoulder surfaces are defined as ideal walls in this model. This allows the fluid to interact with the walls (probe and shoulder) as if the probe were actually there, but inside the probe is completely empty. Not having a solid probe greatly reduced the total number of cells in the mesh because the entire solid region of the probe is avoided completely. This region would be very complicated to mesh due to its complex geometry (as least as complicated as the probes fluid-wall boundary, but likely more so). Eliminating this region of the mesh reduces the size of the simulation files, the amount of computation power needed, and the runtime per iteration. However, by not having this region any information of what is occurring inside the probe is lost, such as internal stresses or heat transfer patterns. This was determined to be an acceptable trade, as Fluent is not specialized for FEM stress calculations, and there would still be a possibility of importing the surface loads (calculated from the wall stresses) into a dedicated FEM model. This possibility is discussed more in the future work as an option for having a sister FEM model developed to simulate what is happening inside the probe while the CFD model developed in this work simulates what happens outside the probe.

Fluid-fluid contacts between different parts are, by default, defined with nonconformal interfaces. A nonconformal interface allows more flexibility when meshing as each region can be meshed independently. The trade-off is that values crossing nonconformal meshes have to be interpolated cross the mesh mismatch, introducing errors. This can be overridden and forced to be conformal using manual meshing control, but due to the sliding mesh theory (discussed in the next section) conformal meshes are very difficult to maintain through timestep updates. Instead, a finer mesh was used on nonconformal interfaces in an attempt to reduce the introduced interpolation error by adding more sample points to interpolate from.

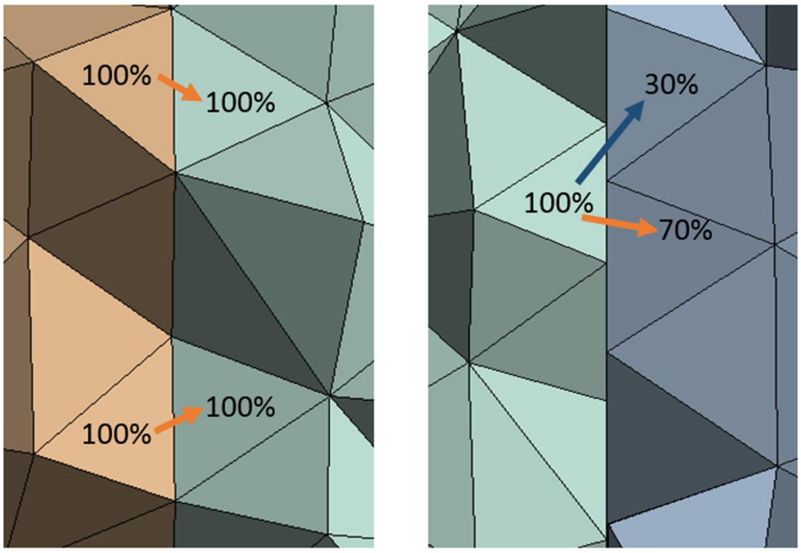

Figure 35: conformal (left) and nonconformal (right) interfaces between mesh regions.

Multiple regions of the same part avoid this problem by automatically defining a conformal interface between the contacts of these regions. In a conformal interface the cell face from one mesh region contacts only a single cell face from the another mesh region. This means that the mesh faces line up perfectly on both sides of the interface and no interpolation is required. In this case, the face fluxes are simply balanced between the two cells sharing the interface. In a nonconformal interface, the cell face from one region can be in contact with two, or more, different cell faces from another region. This means that the flux leaving a single face from one region has to be divided as it enters multiple faces in another region. The default method for estimating this flux division is linear interpolation, i.e. if one face shares 75% of its area with another face, that face receives 75% of the flux. Other, more complex, methods do exist for calculating the flux across a nonconformal interface but this model only used the default basic interpolation method. Figure 35 shows the difference between the two interface methods.

## 3.3 Sliding Mesh

With the core of the model based on an Eulerian mesh, the strategy to include tool rotation through time was a rigid sliding mesh technique. The sliding mesh method allows different parts to move across interfaces in the simulation domain. This allows the entire mesh of a part to move in the domain while the individual cells remain rigid and unchanging. Conditions of every cell zone are defined in the Fluent solver, including sliding mesh motion in translational and rotational directions. For this model the rotating region is defined as rotating at 42 $\frac{\text{rad}}{\text{s}}$, roughly 400 RPM. Based on this condition, the cells in the RR are updated to their new positions every timestep, prior to the solving of the systems governing equations. The scalar values of each cells variables are updated by:

$$\frac{d}{dt}\int_V \rho\phi dV + \int_{\partial V} \rho\phi\left(\vec{u}-\vec{u}_g\right) \cdot d\vec{A} = \int_{\partial V} \Gamma\nabla\phi \cdot d\vec{A} + \int_V S_\phi dV \qquad (2)$$

Where ϕ is any scalar variable (temperature, viscosity, etc...), V is the volume of the cell, ρ is the density of the fluid, $\vec{u}$ is the fluid velocity, and $\vec{u}_g$ is the mesh velocity. The terms on the right side of the equation are for species diffusion and source generation, neither of which are used in this model (apart from the heat flux through the boundaries of the simulation). This equation integrates every scalar variable across the volume of the cell with respect to time and position (XYZ). This is the most general form of the equation, and is defined for use on a fully dynamic mesh. In a fully dynamic mesh the dimensions, as well as the position, of cells in the mesh can transiently change based on the definition of the model (a piston compressing a mesh inside a cylinder is a common application). A sliding mesh simplifies a dynamic mesh by keeping the dimensions, and thus the volume, of the cells constant and only updating their positions through time. This simplifies the time derivative term of the equation to:

$$\frac{d}{dt}\int_V \rho\phi dV = \frac{[(\rho\phi)^{n+1} - (\rho\phi)^{n}]V}{\Delta t} \qquad (3)$$

Where ϕ is any scalar variable, V is the constant volume of the cell, t is the timestep size, and n denotes the value at the respective timestep (it is not a power operator). These new values become the initial values for the current timestep's iterations and are determined by balancing the above equation with the flux through every cell face caused by the mesh velocity. [41]

The length of the timestep is critical to the stability and accuracy of the simulation, typically the smaller the timestep the better, but this increases computation time. The Courant–Friedrichs–Lewy (CFL) condition, or Courant number, is a necessary condition to the stability of a CFD simulation. This condition states that the time domain step cannot be larger than any calculation steps occurring in that domain. Fluent has the ability to adapt the timestep to maintain stability with Courant numbers up to 250 in some situations, but low Courant numbers are more desirable. For determining the sliding mesh timestep needed, the tangential speed at the tip of the shoulder was used with the mesh size at that location to calculate approximate acceptable timesteps based on how far the cells on the shoulder moved over the timestep. This allowed the corrections made by Fluent between timestep updates to be small.

# 4 Model and Solver Theory

## 4.1 Introduction

Ansys Fluent is a Finite Volume Method (FVM) based CFD program designed for modeling fluid flow, heat transfer and chemical reactions in complex geometries [41]. This makes the model inherently fluid based. Because FSW is a solid-state process there is should be no liquid/melted material; but in the simulation, being fluid based, the entire calculated domain is technically fluid. This CFD approach approximates the softened material around the FSW tool as a highly viscous fluid. Far from the tool, the fluid becomes so viscous that it essentially behaves as a solid. However, solid-state to fluid approximations are limited, and even a highly viscous "solid-like" fluid is still a fluid and still flows a little bit, making residual stress and deformation difficult (if not impossible) to simulate using a CFD approach. CFD based models, such as this one, focus on simulating the material flow properties in the SZ (nugget) and TMAZ during welding while solid mechanics based models typically focus on post weld properties such as grain size, hardness profiles, and residual stress/deformation.

A FVM solver treats mesh elements, or "cells", as control volumes and uses integrals of conservation laws to maintain the fluxes through the cell faces. Essentially, what goes into the cell through a face must either be stored in the cell or exit through its other faces. The conservation equations are calculated from cell centers (Fluent's sister program CFX uses a more complex cell vertex FVM approach) and these solutions are converted into face fluxes. This process is iterated through until convergence of all the face fluxes and cell centers occurs. Basically, the governing equations are solved for a control volume and those results are stored in the cell center. These results are then converted into surface integrals, also known as face fluxes, along the cell interfaces and balanced with all neighboring cells control volumes and surface integral solutions. This is different from traditional FEM, which calculates solutions based on the nodal boundaries (grid vertexes) and balances the element based on the surface solutions.

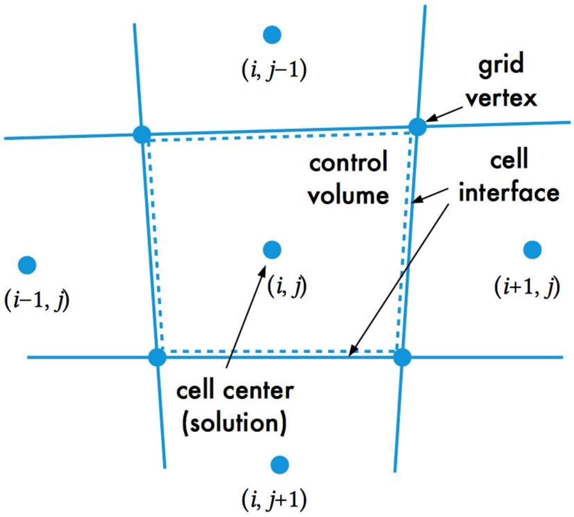

Figure 36: Example of a cell centered FVM grid. [42]

In this model, the sliding mesh simulates the rotation on the tool probe only. Instead of translating the probe through the fluid domain, the fluid flows past the probe at a constant rate of 0.00136 $\frac{\mathrm{m}}{\mathrm{s}}$, equivalent to the weld speed of 82 $\frac{\mathrm{mm}}{\mathrm{min}}$. All the copper material is treated as a laminar, incompressible, non-Newtonian fluid moving with an initial constant velocity through the simulation domain. This simplification limits the need of a sliding mesh for only the rotational component of the probe while the velocity of the fluid simulates the weld travel.

To maximize the computing power of the PC used in this work, double precision variables with parallel processing was used. Double precision variables allowed more information per cell to be carried in the solver system. This reduces the truncation errors associated with single precision variables in areas where gradients in the solutions are high. This costs more memory when computing, as the system has to carry twice as many characters per variable (it is not exactly double when converting from a 32-bit to 64-bit system but the exact conversion is not important here). It is possible that single precision variables could have sufficed for this model, but the memory use increase was acceptable in order to maintain the highest possible accuracy. Partitioning allowed the batches of the cells in the mesh to be divided among the multiple cores of the processors. This allowed multiple processors to calculate the solutions to different parts of the mesh and then compile those results into the final solution. This reduced computation time over a single processor attempting to iterate through all 5 million elements.

## 4.2 Governing Equations

The three primary conservation equations that Fluent solves in this model are continuity (mass), momentum, and energy; their general form are equations ( 4 ), ( 5 ), and ( 6 ), respectively [41].

$$\frac{\partial \rho}{\partial t}+\nabla\cdot(\rho\vec{v})=S_m \tag{4}$$

$$\frac{\partial}{\partial t}(\rho\vec{v})+\nabla\cdot(\rho\vec{v}\vec{v})=-\nabla p+\nabla\cdot(\overline{\overline{\tau}})+\rho\vec{g}+\vec{F} \tag{5}$$

$$\frac{\partial}{\partial t}(\rho E)+\nabla\cdot(\vec{v}(\rho E+p))=\nabla\cdot\left(k_{eff}\nabla T-\sum_j h_j\vec{J}_j+(\overline{\overline{\tau}}_{eff}\cdot\vec{v})\right)+S_h \tag{6}$$

Where v is the velocity vector, P is the pressure vector, ρ is density, E is the enthalpy, and T is the temperature (in kelvin). With the assumption of a laminar, incompressible, non-Newtonian fluid, and some simplifications to the material model, a more specific form of these equations can be acquired. One important consideration is that in a moving frame, like a sliding mesh, the velocity definition is relative to the motion of the mesh. This relative mesh velocity allows the mesh speed to be accounted for at each timestep and is included in all velocity terms in moving cells.

Due to a constant density (ρ) and no source generation terms ($S_m$), the continuity equation becomes:

$$\nabla\cdot(\rho\vec{v})=0 \tag{7}$$

Essentially, this means that the mass flow in $\frac{\mathrm{kg}}{\mathrm{s}}$ per unit volume ($m^3$) should total to zero for all cells with respect to space (XZY components), the time term drops away because density is constant [40]. With no gravitational or declared body forces, the momentum equation simplifies to:

$$\frac{\partial}{\partial t}(\rho\vec{v})+\nabla\cdot(\rho\vec{v}\vec{v})=-\nabla\mathrm{p}+\nabla\cdot(\overline{\overline{\tau}}) \tag{8}$$

The equation controls the conservation of Newton's second law F=ma per unit volume ($m^3$). The first term on the left is the change in force with respect to time; the second is with respect to XYZ space. $-\nabla \mathrm{p}$ and $\nabla \cdot \bar{\bar{\tau}}$ are the surface forces acting on the cells due to pressure and stress; $\bar{\bar{\tau}}$ is the stress tensor, which is defined by Fluent in general form as [41]:

$$\bar{\bar{\tau}} = \mu\left[(\nabla\vec{v} + \nabla\vec{v}^T) - \tfrac{2}{3}\nabla\cdot\vec{v}I\right] \tag{9}$$

Due to incompressible flow, the volume dilation term is unused, which simplifies the stress tensor to:

$$\bar{\bar{\tau}} = \mu[(\nabla\vec{v} + \nabla\vec{v}^T)] \tag{10}$$

Where $\mu$ is the dynamic viscosity and $\nabla\vec{v} + \nabla\vec{v}^T$ are the velocity and velocity transpose vectors. The sum of these vectors creates a 3x3 matrix, which defines the stress acting on every face of a 3D element (XYZ). This equation is also defined by using the rate of deformation tensor $\bar{\bar{D}}$, which is crucial for determining the viscosity of the fluid; this will be discussed in the material model section.

With no species diffusion (J) or volumetric generation ($S_h$), the energy equation simplifies to:

$$\frac{\partial}{\partial t}(\rho E) + \nabla\cdot\big(\vec{v}(\rho E + p)\big) = \nabla\cdot\big(k_{eff}\nabla T + (\bar{\bar{\tau}}_{eff}\cdot\vec{v})\big) \tag{11}$$

This equation is enthalpy based conservation of energy in Watts ($\frac{J}{s}$) per unit volume ($m^3$). The first term on the left is the change in enthalpy with respect to time; the second is with respect to space/momentum and pressure (the pressure work term is negligibly small with incompressible flow). Heat generation occurs from the viscous heating term $\bar{\bar{\tau}}\cdot\vec{v}$ only. No other heat generation occurs in this model. The assumption was that viscous dissipation was the primary cause of heat generation and that due to the complexity of the probe surfaces a Coloumb friction model was an unnecessary modeling complication. The conduction term $k\nabla T$ is used to pull heat from the model based on the boundary conditions and to balance the system.

The convergence of these equations is monitored to determine when the model has reached a steady state solution for each timestep. Additionally, the viscosity of the fluid is tracked to determine when the material model (discussed later in this section) and the governing equations have reasonably converged. Finally, the average temperature of the RR is tracked through every timestep to confirm when the transient solution has reached a steady state temperature regardless of timestep. Once all three of these criteria (governing equations, fluid viscosity, and RR temperature) are either converged, or are no longer changing with time, the simulation is considered complete.

### 4.2.1 Solver Method; Segregated or Coupled

The order in which the governing equations are solved can affect how well the simulation repeatedly converges to the correct results. There are many different methods for solving these equations, but Fluent offers two general categories, segregated or coupled. Each of the methods has many different sublevels that can be manipulated based on the situation, but the major change occurs in how the system handles the equations on the top level. The Pressure-Velocity coupling is the critical aspect of the solver; Figure 37 shows how the different methods proceed through the iterative process.

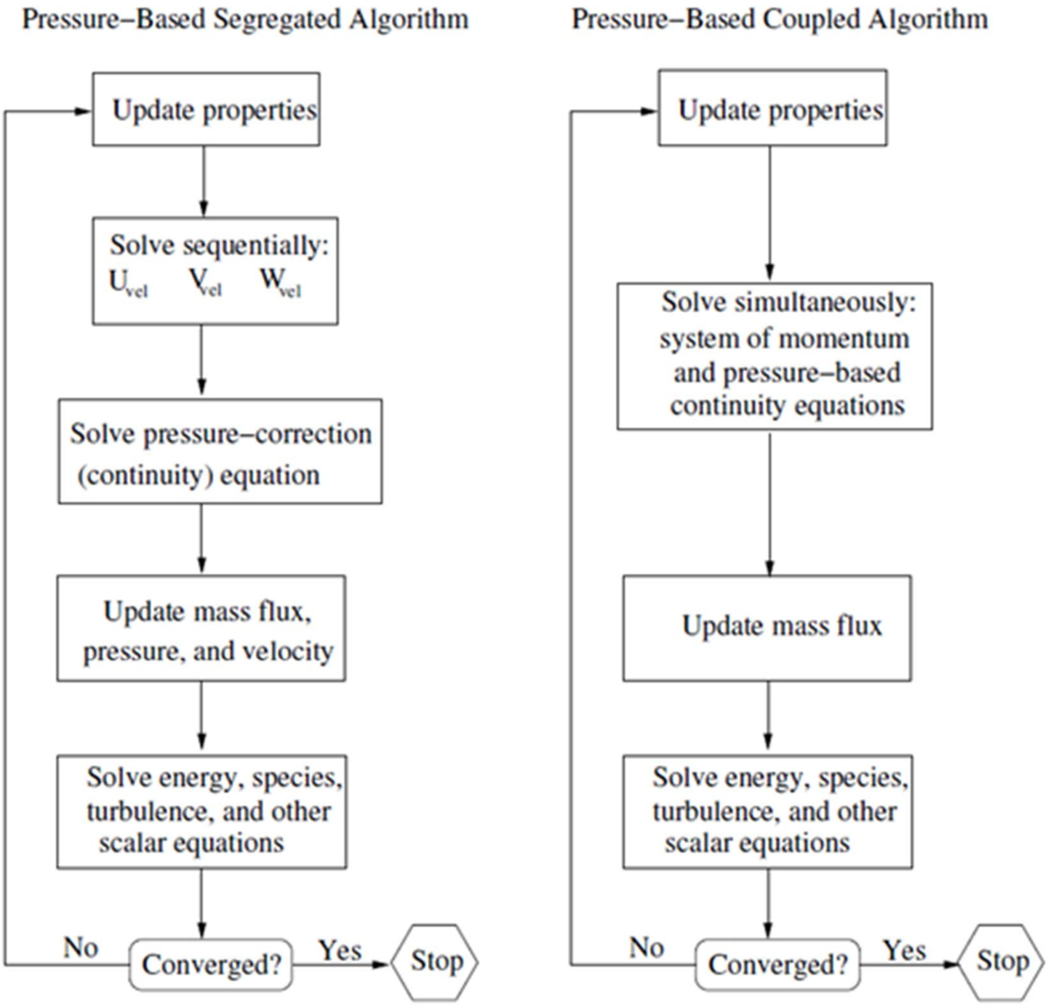
Pressure–Based Segregated Algorithm
Update properties
Solve sequentially:
U vel V vel W vel
Solve pressure–correction (continuity) equation
Update mass flux, pressure, and velocity
Solve energy, species, turbulence, and other scalar equations
No
Converged?
Yes
Stop
Pressure–Based Coupled Algorithm
Update properties
Solve simultaneously: system of momentum and pressure–based continuity equations
Update mass flux
Solve energy, species, turbulence, and other scalar equations
No
Converged?
Yes
Stop

Figure 37: Pressure based solver methods. [41]

Because all the governing equations are linked through velocity and pressure, it is important to declare how these variables depend on each other. Segregated solvers tend to be faster, simpler, and less computationally intensive; for most cases this approach behaves well and works as intended. Using a pressure correction equation to step through the governing equations sequentially is normally a good method for reducing computation cost, with very little increase in convergence time. However, this approach starts to weaken when there are very large changes in velocity and pressure within a small space or timeframe. This causes the pressure correction equations to "swing" and become more unreliable. Figure 38 shows the pressure along the two points of the original probe during four identical simulations, with the only difference being the solver method. It is important to notice that the pressure patterns for all four simulations match quite well, but the segregated solvers tend to over predict then under predict, depending on which side of the "swing" the iterations stopped. Eventually this swinging does decrease and the simulation does converge to the correct value, but the iteration count becomes prohibitively long.

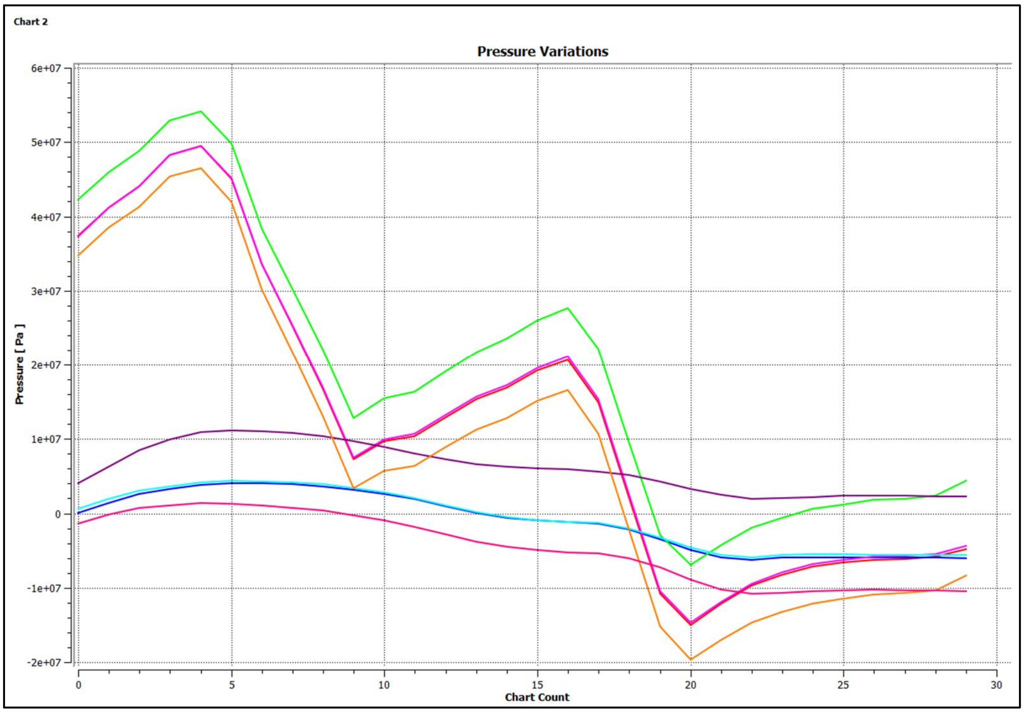

Figure 38:  Two coupled vs. two segregated solver pressure results comparison. The segregated solver solutions bound the coupled solver solutions, i.e. green and orange (segregated) bound the pink (coupled), while purple and red (segregated) bound the blue (coupled).

A coupled solver overcomes this need to use a pressure correction equation by solving the momentum and continuity equations concurrently. The two pink and two blue lines are the coupled solver solutions while the green, orange, purple, and red, are the segregated solver solutions. Using the coupled solver results in an independent, faster converging solution, but uses much more RAM because all the variables must be available for access at the same time. For this work, a segregated solver was used until the simulation was near steady state for speed, and then a coupled solver was used to complete the solution for more reliable steady state results.

## 4.3 Material Model

As stated before, the primary material for this work is an OFP copper. The simulation treats this material as a laminar, incompressible, non-Newtonian fluid. The material's density, specific heat, thermal conductivity, and viscosity are all needed to define the governing equations within the model. To simplify the model only the viscosity was variable; density, specific heat, and conductivity were all constant. The values listed in Table 4 and were based on OFP copper at room temperature [43]. These values are constant because they had a relatively small effect on the overall simulation and because the primary goal was to compare different probe geometries, meaning every simulation would experience effectively the same errors in the material model. A more accurate material model with temperature dependent properties could possibly improve the accuracy of the steady state simulations, and is discussed in the future work section.

Table 4: Copper properties used in simulations. [43]

| Density ($\rho$) | Specific Heat ($c_p$) | Thermal Conductivity (k) |
|---|---|---|
| 8,940 $\frac{\mathrm{kg}}{\mathrm{m}^3}$ | 385 $\frac{\mathrm{J}}{\mathrm{kg}*\mathrm{K}}$ | 395 $\frac{\mathrm{W}}{\mathrm{m}*\mathrm{K}}$ |

With no meshed solid regions for the probe and shoulder, many material properties, such as yield strength or modulus of elasticity, were not needed. The only thing needed to fully define the solid materials in the simulation were properties that affect heat transfer. The properties required were density, specific heat, and thermal conductivity. Just like with the copper, constant properties were used for simplification of the model. The probe was made of the nickel alloy Nimonic 105 while the shoulder was made from the tungsten alloy Densimet D176 [3]. The properties used for these are listed in Table 5 and were sourced from their respective manufacturer's datasheets [44] [45]. Additionally, no coatings were considered, or simulated, because of the inability to easily define more than one material on a single surface in Fluent.

Table 5: Probe and shoulder material properties. [44] [45]

| | Density (ρ) | Specific Heat ($c_p$) | Thermal Conductivity (k) |
|---|---|---|---|
| Nimonic 105 (probe) | $8{,}010\,\frac{\mathrm{kg}}{\mathrm{m}^3}$ | $419\,\frac{\mathrm{J}}{\mathrm{kg}*\mathrm{K}}$ | $10.89\,\frac{\mathrm{W}}{\mathrm{m}*\mathrm{K}}$ |
| Densimet D176 (shoulder) | $17{,}500\,\frac{\mathrm{kg}}{\mathrm{m}^3}$ | $130\,\frac{\mathrm{J}}{\mathrm{kg}*\mathrm{K}}$ | $74\,\frac{\mathrm{W}}{\mathrm{m}*\mathrm{K}}$ |

To determine viscosity, a viscoplastic model of the flow stress in the material was used. Originally developed in the work done by Sheppard-Wright [29], the model defines a temperature and strain rate dependent flow stress given by:

$$\sigma_e = \frac{1}{\alpha} ln\left(\left(\frac{Z}{A}\right)^{\frac{1}{n}} + \sqrt{\left(\frac{Z}{A}\right)^{\frac{2}{n}} + 1}\right) \tag{12}$$

Where A, α, and n are material constants and Z is the Zener-Hollomon parameter, defined as:

$$Z = \dot{\varepsilon} e^{\frac{Q}{R*T}} \tag{13}$$

Where Q is the materials activation energy and R is the universal gas constant. As seen by these equations, both strain rate ($\dot{\varepsilon}$) and temperature (T) affect the Zener-Hollomon parameter, which is the driving force of the modeled flow stress, $\sigma_e$. This material model is quite common in many simulations, in both its logarithmic and hyperbolic sine form, because of its compatibility with many numerical solvers and easily definable constants. Unlike other models, this model has no strain dependence, something most CFD software does not solve for by default. This makes this model very well suited for FSW modeling using a CFD approach.

To define viscosity from the flow stress, a ratio to the effective strain rate is used:

$$\mu = \frac{\sigma_e}{3\dot{\varepsilon}} \tag{14}$$

Returning dynamic viscosity in Pa*s. The viscosity function can be represented by a 3D curve with strain rate and temperature as the XY plane. This gives the viscosity an overall decreasing function along both axes, as seen in Figure 39. The material constants Q, A, α, and n play a large role in determining the flow stress, and can have major effects on the viscosity behavior. Determining these constants is critical for an accurate model.

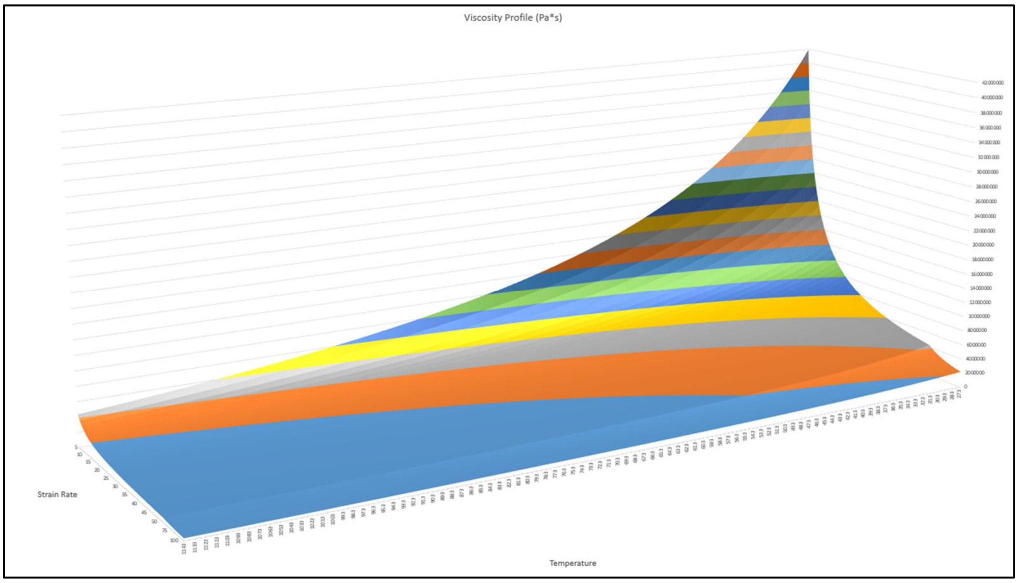

Figure 39: Representative 3D viscosity curve of strain rate range 5-100 s$^{-1}$.

Determination of the material constants for copper was done through a combination of data fitting and research. A large amount of work has already been done for determining these constants for aluminum alloys, and this process could be adapted for OFP copper. Sheppard-Jackson developed a method of multiple regression analysis of a linearized version of EQ 12 and solved the constants for many aluminum alloys [46]. Tello et al. refined this process using Matlab's *fminsearch* function to do a least squared minimization of the error between modeled and experimental values [47]. For this work, optimization of the constants was done using Excel's GRG Nonlinear Solver method. This method allowed Excel to find local optimal solutions of the material constants that minimized the total error ($E$) between modeled and experimental data. The function minimized was:

$$E = \sum\left[\sigma_{mod}(T, \dot{\varepsilon}) - \sigma_{exp}(T, \dot{\varepsilon})\right]^2 \tag{15}$$

Where $\sigma_{mod}$ is the modeled flow stress at a given temperature and strain rate, given by EQ 12, and $\sigma_{exp}$ is the experimental flow stress data for the same temperature and strain rate. The solver manipulated the values of A, α, and n to minimize $E$, the sum of the errors in the system. The nominal activation energy for OFP copper was known to be 198 $\frac{\mathrm{kJ}}{\mathrm{mol}}$ [48], which meant that only the values for A, α, and n needed to be determined. In order to accurately fit the model, flow stress data was needed across a wide range of temperature and strain rates. This data was rare for copper and rarer still for an OFP alloy of copper. A workaround for this problem was to use pure copper and copper alloys with similar compositions to OFP copper. In total, data from OFP copper [48] [49], OFHC copper [50], DHP copper [51], UNS C12200 copper [52], and ETP copper [53] was used. While these coppers have somewhat different compositions, they all have reasonably similar hot flow characteristics, allowing for an accurate enough copper model. More data, with purely OFP copper flow stresses, could give an even more accurate model and is discussed in the future work.

With the experimental data, flow stress curves could be fitted across constant strain rate and temperature lines, Figure 40 & Figure 41 show the best fit curves for the flow stresses with strain rates from 0.001-100 s$^{-1}$ and temperatures from 573-1223 K. Table 6 lists the values of A, α, and n used. Overall, the model showed a good match to the data across most temperatures and at low strain rates, but begins to have errors at high temperatures and strain rates above 10 s$^{-1}$. This is likely due do a change in the deformation rate controlling mechanism not accounted for in this version of the model.

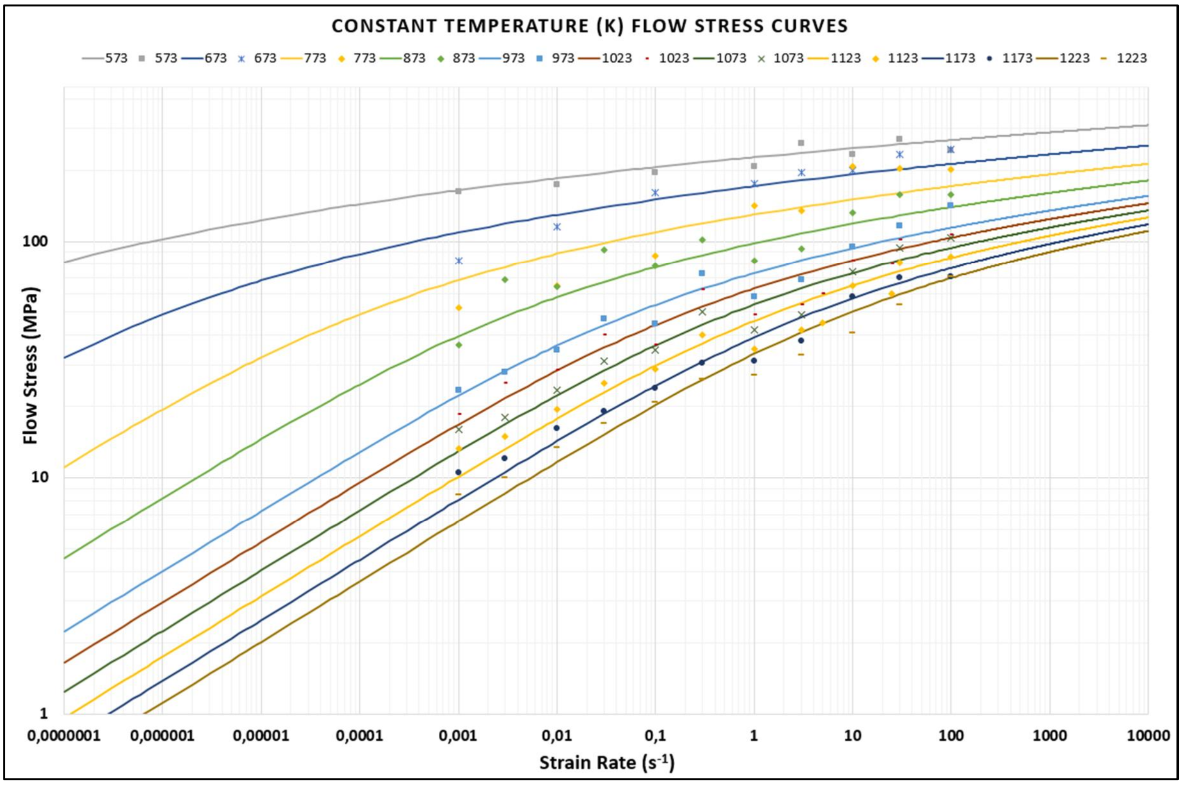

Figure 40: Constant temperature flow curves; lines are modeled and points are experimental values.

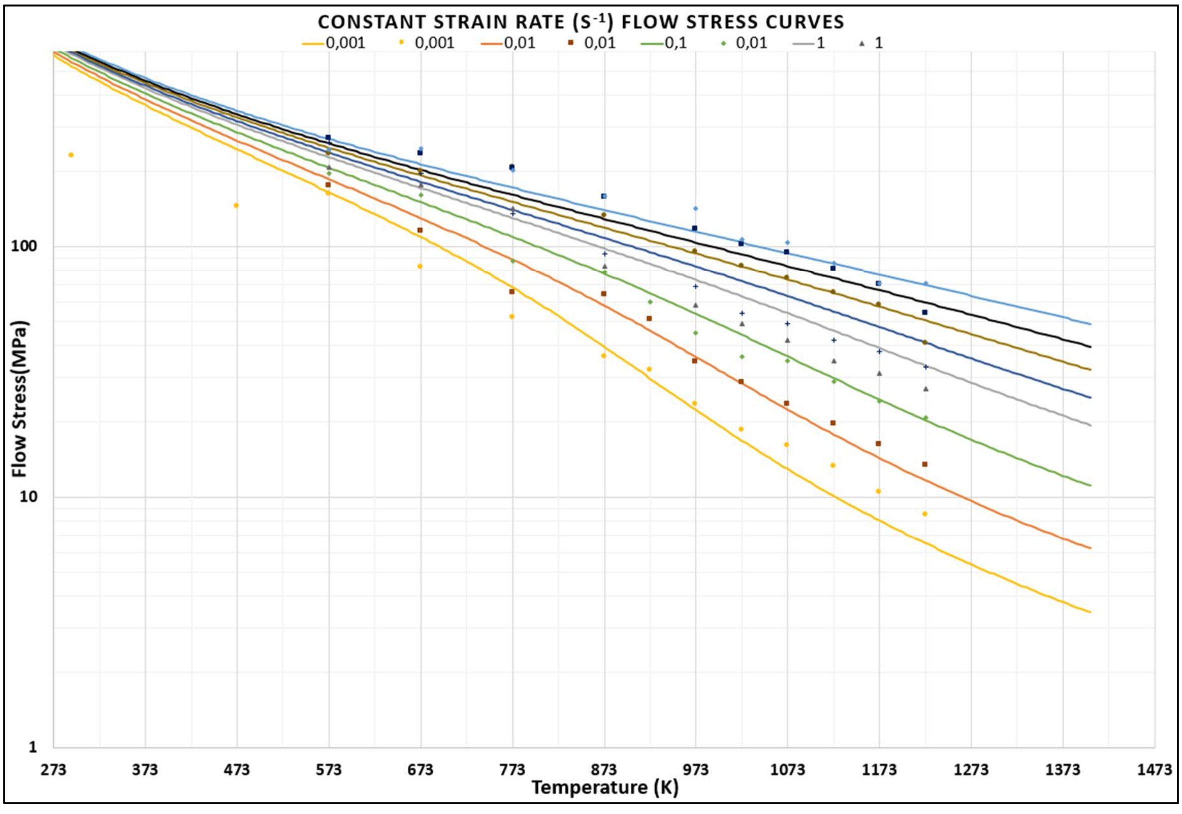

Figure 41: Constant strain rate flow curves; lines are modeled and points are experimental values.

Table 6: Material model constants.

| Q | A | α | n |
|---|---|---|---|
| 198,000 $\frac{\text{kJ}}{\text{mol}}$ | 197,663,757 $s^{-1}$ | 2.8470x$10^{-8}$ Pa | 3.8974 |

These errors at high strain rates and temperatures are most likely caused by a change in the controlling mechanism for the activation energy. Prasad and Rao showed apparent changes of the rate controlling activation energy depending on the temperature and strain rate region. They suggest that at both high temperatures (700-950 °C) and high strain rates (3-100 $s^{-1}$) the activation energy for self-diffusion becomes the controlling mechanism over dislocation diffusion or lattice diffusion [54]. This change in activation energy meant that the material model could be improved by having the different zones in the simulation domain behave according to the temperature and strain rate most common in that area. A second set of constants and a new activation energy was determined for strain rates above 5 $s^{-1}$ and the model was re-optimized with the high strain rate data split into its own zone. This allowed the model to transition from the different zones and predict the flow stresses more correctly for all regions. Figure 42 & Figure 43 show the improvement to the curve fits at the high strain rates and Table 7 shows the improved material constants with their respective activation energies.

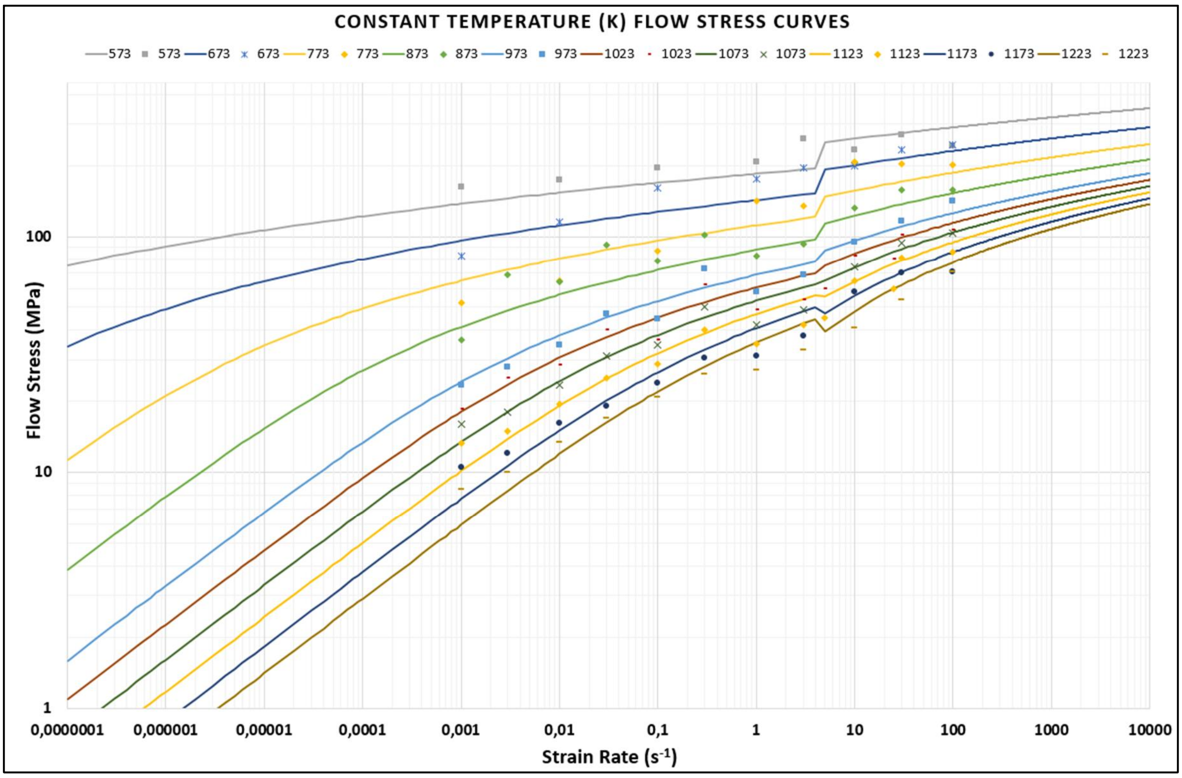

Figure 42: Constant temperature flow curves; lines are modeled and points are experimental values.

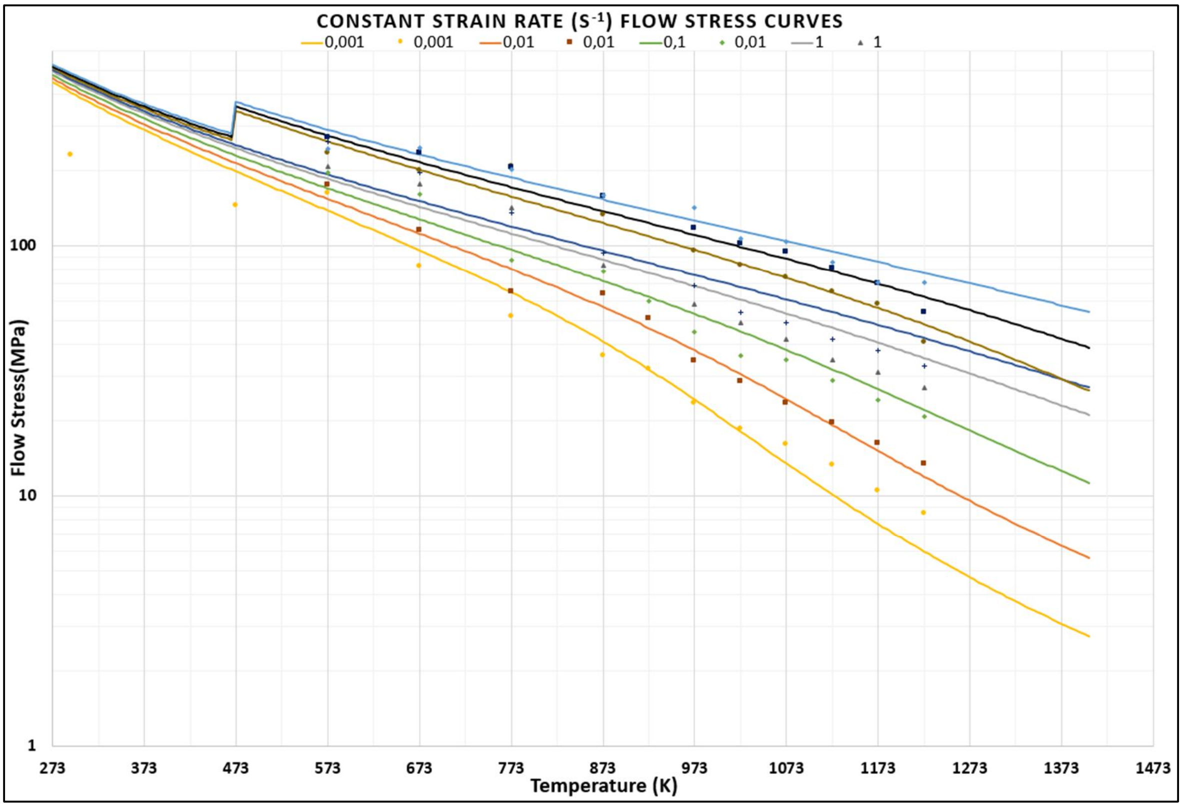

Figure 43: Constant strain rate flow curves; lines are modeled and points are experimental values.

Table 7: Improved material constants.

| Q | A | α | n |
|---|---|---|---|
| 198,000 $\frac{\mathrm{kJ}}{\mathrm{mol}}$ | 15,403,124 $s^{-1}$ | 4.6693x$10^{-8}$ Pa | 3.1525 |
| Q2 | A2 | α2 | n2 |
| 146,936 $\frac{\mathrm{kJ}}{\mathrm{mol}}$ | 1,551,620 $s^{-1}$ | 4.4473x$10^{-8}$ Pa | 1.7359 |

As seen from the figures above, a multi-zone material model has a noticeable improvement in data fitting over the traditional model. However, the ideal solution would be to have a more advanced, fully continuous, model to eliminate the jumps in flow stress (and viscosity) occurring at the strain rate where the material constants change; this possibility is discussed more in the future work.

### 4.3.1 Iterative Viscosity Function

To convert the material model into something usable by Fluent a User Defined Function (UDF) was written to define a custom cell viscosity. Fluent uses the UDF during the update properties portion of the iterative loop [41] and defines a scalar viscosity at a cell center based on that cell's strain rate magnitude and temperature. Temperature is already defined as a scalar at the cell center by default, but strain rate magnitude is defined as:

$$\dot{\varepsilon} = \sqrt{2 * \overline{\overline{D}} : \overline{\overline{D}}} \qquad (16)$$

Where $\overline{\overline{D}}$ is the rate of deformation tensor, given by:

$$\overline{\overline{D}} = \left(\frac{\delta u_j}{\delta x_i} + \frac{\delta u_i}{\delta x_j}\right) \qquad (17)$$

Originally, the stress tensor $\bar{\bar{\tau}}$ was defined by the velocity vector in EQ 10; but for determining viscosity, it is more useful to define $\bar{\bar{\tau}}$ as a dependent of $\bar{\bar{D}}$. By substitution, it can be shown that:

$$\bar{\bar{\tau}} = \mu\bar{\bar{D}} \tag{18}$$

Is equal to EQ 10, creating a numerical connection between the material model and the governing equations. This connection is an interdependent loop that must be solved iteratively; i.e. the viscosity depends on the temperature, but the temperature depends on the stress tensor (due to viscous heating), and the stress tensor is partially defined by the viscosity. Figure 44 is a diagram showing how Fluent begins, and iterates through this loop, attempting to find acceptable convergence between the material model and the governing equations.

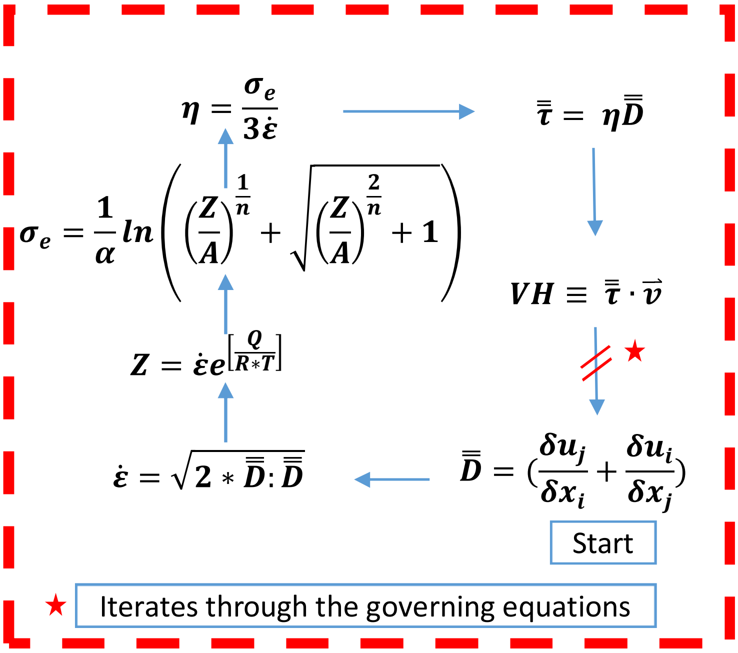
$\eta = \frac{\sigma_e}{3\dot{\varepsilon}}$
$\bar{\bar{\tau}} = \eta\bar{\bar{D}}$
$\sigma_e = \frac{1}{\alpha}ln\left(\left(\frac{Z}{A}\right)^{\frac{1}{n}} + \sqrt{\left(\frac{Z}{A}\right)^{\frac{2}{n}} + 1}\right)$
$VH \equiv \bar{\bar{\tau}} \cdot \vec{v}$
★
$Z = \dot{\varepsilon}e^{\left[\frac{Q}{R*T}\right]}$
$\dot{\varepsilon} = \sqrt{2 * \bar{\bar{D}}:\bar{\bar{D}}}$
$\bar{\bar{D}} = (\frac{\delta u_j}{\delta x_i} + \frac{\delta u_i}{\delta x_j})$
Start
★ Iterates through the governing equations

Figure 44: UDF iterative loop.

## 4.4 Boundary Conditions

The boundary conditions can be defined on the walls, inlet, and outlet of the simulation and can dramatically affect the outcome. The two categories of conditions defined for this model are related to the momentum and thermal properties of the boundaries. For this model, there are four groups of boundary conditions; the inlet, outlet, outer walls, and tool walls (probe and shoulder). Some global conditions were also set to define the entire domain. For the global operating conditions, the temperature was set to 293 K (20 °C), operating pressure was set to 0 Pa, and gravitational effects were turned off.

The inlet was set to introduce material at a constant velocity of 0.00136 $\frac{\mathrm{m}}{\mathrm{s}}$ (82 $\frac{\mathrm{mm}}{\mathrm{min}}$) and the global temperature and pressure. This allowed the material to flow past the probe at the weld travel speed, simulating the transverse movement of the tool without having the tool move through the mesh. The outlet simply allowed fluid out of the system with no pressure gradient, making the entire inlet-outlet flow system purely momentum based. The outer walls were designed to have minimal interference on the simulation and were used to balance the steady state temperatures. These walls were set to have the same velocity of the fluid so there would be no influence on flow from the walls (setting a zero stress slip condition would have also worked). Thermally, the walls were set to have a constant heat transfer coefficient of 25 $\frac{\mathrm{W}}{\mathrm{m^2K}}$ to simulate the effect of ambient air-cooling. While this is not quite a perfect representation because realistically the copper is not surrounded evenly by air on all sides, this value is just a dummy variable used to balance the system to a reasonable steady state.

The probe and shoulder walls are set to be rotating at the same speed of the sliding mesh in the rotating region (RR) at 42 $\frac{\mathrm{rad}}{\mathrm{s}}$, which simulates the weld rotation speed. Both the probe and shoulder are treated as ideal walls with no slip or frictional heat generation occurring. Any material that comes in contact with the wall instantly becomes stuck to the wall and is assumed to move at the same speed as the wall. However, a constant slip condition can be added to include material slip on the walls, reducing the heat generated by deformation (similar to Colegrove's suggestion [28] and Schmidt's work [32]). A more realistic tool-material boundary could be developed in the future that attempts to simulate the frictional effects of complex geometry, but is outside the scope of this work.

As stated in the governing equations, the probe and shoulder behave as heat sinks using simple conductive heat transfer through the surface. A wall thickness is given so Fluent calculates simple one-dimensional heat transfer using Fourier's law of heat conduction and the defined material constants for the wall [41]. Just like with the heat transfer coefficient for the outer walls, this conductive wall system is used as a dummy variable that remains constant across all the simulations. A very large heat transfer coefficient was given to the surfaces of the probe and shoulder to simulate forced cooling of the tool, unlike the ambient cooling of the base copper.

### 4.4.1 Initial Conditions

The initial conditions are the starting point for the simulation and are important to model stability, poorly defined initial conditions lead to long convergence times and system instability. To speed up simulation time for this model, two sets of initial conditions were used. The first set was used to define a simpler, steady, non-sliding mesh simulation using a rotating reference frame (RRF). Then, the results from the RRF simulation were used as the initial conditions for the sliding mesh simulation. This allowed a near steady-state temperature to be reached much more quickly, due to the nature of a steady-state simulation, which was imported into the transient simulation for more accurate flow calculations. Because plunging was not simulated, a constant velocity of 0.00136 $\frac{m}{s}$ and temperature of 293 K was given to all the fluid initially. A temperature of 673 K to the RR, and 373 K to the inner region, was patched into the fluid in order to put the initial viscosity into a realistic territory with steady state. This simulation was ran until the temperature, velocity, and viscosity reasonably converged using RRF and those results became the initial conditions for the sliding mesh simulation. Figure 45 shows the two stages of the initial temperatures.

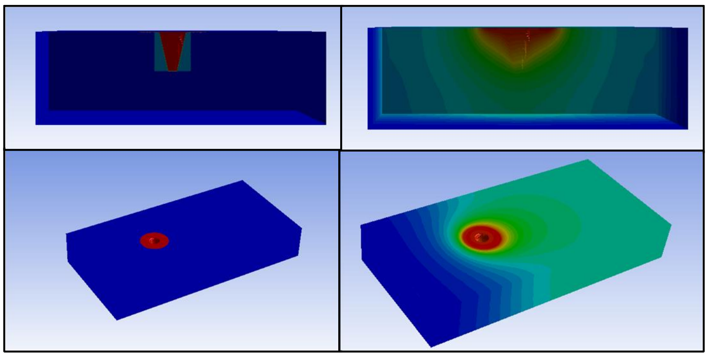

Figure 45: Initial conditions for RRF (left) and sliding mesh (right) simulations.

# 5 Model Validation

## 5.1 Introduction

This section is dedicated to tying the model to the actual evidence found in the process of welding the copper canisters. This model is limited by design and many assumptions were made in its creation that drive it away from perfectly simulating the FSW process. However, the goal of the model was to create a reliable method for qualitatively comparing probe geometry changes while remaining quantifiably accurate enough to support its findings. The primary method of validation was to look at the material evidence left behind on a used probe. This meant looking at residual material to determine how the material was flowing around the probe during welding and comparing that analysis to the simulation predictions. Additionally, predicting the size of the weld zone using different model flow zones allowed for rough predictions of the weld size. This could be compared to cross sections of weld samples to determine if the model predicts this size of the weld regions reasonably well. Finally, determining the predicted forces and torques acting on the surface of the probe due to the fluid, and relating those to the loads registered by the FSW machine confirmed if the model was operating within the same processing window as the actual FSW application.

Model validation uses two of the parameters that define the model most: the material model based viscosity, and the mass-momentum-pressure coupling from the governing equations. The viscous patterns of the material flow on the probe are used to show what is occurring in the near field. Isosurfaces of the viscosity and strain rate (because they are inversely related) in the fluid can be used for predicting the size and shape of different high-flow and low-flow zones. Cross sections of these isosurfaces can be compared to sliced samples of the welded canisters to compare how these flow zones compare to the actual weld zones. By looking at the pressure caused by the fluid acting on the probe walls it is possible to relate those pressures to the flow evidence seen on the actual probe. Integrating those pressures across the face area of the probe can give the predicted forces acting on the probe, which can be compared to the actual forces registered by the FSW machine.

Some comparative analysis of probe B to the original probe is included in this section as the results are mostly used for validating the model but also have some value in comparative analysis. This section mostly covers the work done in attempting to correlate the simulated FSW model to the actual FSW process. As the main work of this thesis was to develop a model that focused on probe geometries, the model was only validated as a way to confirm that it was at least somewhat realistic. Further validation and improvements to this model, which have not been completed in this thesis, could be done to further improve the models accuracy and reliability. This could include fully mapped weld zone size and shape (including nugget, TMAZ and HAZ), microstructural (grain size) and hardness analysis, weld temperature field comparison, and base material shear stress to yield stress correlation.

## 5.2 Viscosity & Strain Rate Zones

Relating the viscosity patterns in the model to the evidence presented on the probe validates some of the flow characteristics. Figure 46 compares the same simulated viscosity profile seen earlier, to an actual used probe. The copper is stuck in the flutes of the real probe down its length, just like in the simulation. Near the shoulder, a large trailing edge shows the transition from low viscosity sliding material behind the MX features to a high viscosity low flow zone inside the flute. The signs of wear Nenonen found on the trailing edge of the flutes, indicative of frictional sliding [6], further confirm this evidence. Near the tip, this high viscosity zone almost completely fills the flute; both the real probe and the simulation show this. This creates a high viscosity pocket of copper trapped against the flute that the rest of the material flows over, reducing the effectiveness of the flutes.

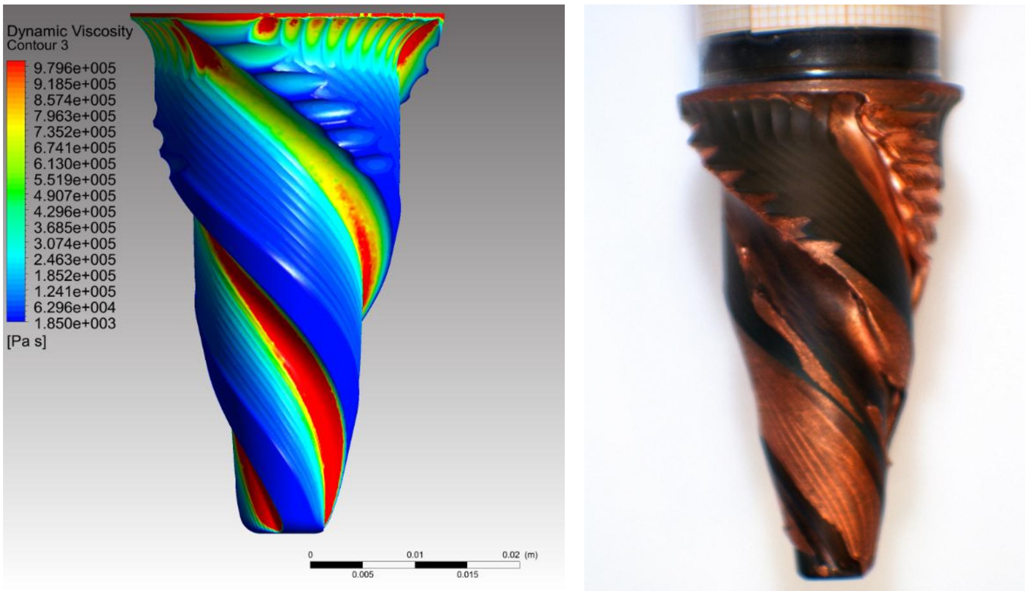

Figure 46: Simulated probe viscosity compared to residual copper evidence on the actual probe.

In a CFD based simulation of FSW there is a point when the "fluid" approximation of the material begins to break down. Determining the regions where the fluid simulated by the material model actually behaves similar to the fluid-like material inside the weld zone is important in predicting the weld process. There are different methods for predicting the size and shape of the weld zone but there is no definitively correct method. This model uses a constant strain rate and viscosity zone approach originally proposed by Colegrove and Shercliff [28] and Nandan et al. [30]. This method involves plotting a curve that follows a path where either the strain rate or viscosity are the same value across a weld cross section. This curve is assumed to be a boundary between different flow regions within the weld zone. The selection of the values for strain rate, or viscosity, to plot is essentially an educated guess as to what value best predicts the actual flow zones. Colegrove and Shercliff chose a strain rate of 2 $s^{-1}$ [28] while Nandan et al. chose a viscosity of $5^6$ Pa*s [30].

Even though they were not used in this work, other methods for predicting the weld zone exist and could be useful for further validation. Using the same shear stress balance method as Källgren to find the boundary between the HAZ and TMAZ [27] shows how the model predicts the size of the different weld zones. Unlike Källgren's model, which predicted a parabolic TMAZ (Figure 26) the model developed in this thesis predicts a zone shown in Figure 47. This zone is much closer to the probe near the tip and does not predict a very large zone under the probe. Figure 47 also compares the method used by Källgren to a constant 2 $s^{-1}$ strain rate curve (Colegrove's method). Overall, both methods agree quite well with each other in their predictions of the weld zone; whether they predict the actual weld zone correctly is open for discussion. When compared to a scaled image of a weld cross section it appears that the weld shape is somewhat under predicted, but in general, it matches reasonably well. Additional work is required to fully analyze how accurately the model predicts the different weld zones (perhaps microstructural analysis) but for the purpose how having a (reasonably accurate) comparative model, it is acceptable.

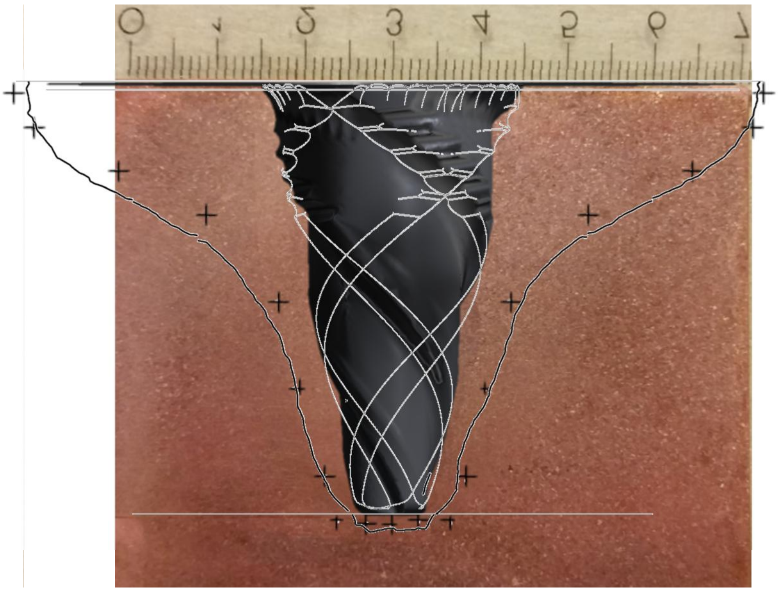

Figure 47: Predicted HAZ/TMAZ boundary using two different methods. The black dots are the shear stress balance method and the black line is a constant 2 $s^{-1}$ strain rate.

The difficulty when comparing the actual weld zones to a constant strain rate or viscosity curve is in selecting the correct value of the curve that realistically predicts the weld zone. In the current model, this can be done by plotting a curve where either the strain rate is so low or the viscosity is so high that the fluid is effectively undisturbed by the weld tool. Selection of the values where this occurs is very arbitrary and requires comparison to actual welds for validation. In this model it was found that a viscosity of $10^9$ Pa*s and strain rate of 0.01 $s^{-1}$ predicted the boundary of the no-flow zone reasonably well. Figure 48 shows how the $10^9$ Pa*s viscosity curve overlays on a weld cross-section. Visually this image appears to closely match the actual weld shape when predicting the boundary where the base material is unaffected. Figure 48 appears to best represent the entire low-flow zone while Figure 47 represents a higher flow zone, where the material is much less viscous and undergoes much higher strains. However, this $10^9$ Pa*s viscosity was only selected as the boundary because of the good visual matchup with the welds, further analysis of the copper weld zones could give a better understanding of the flow regions and more accurate predictions.

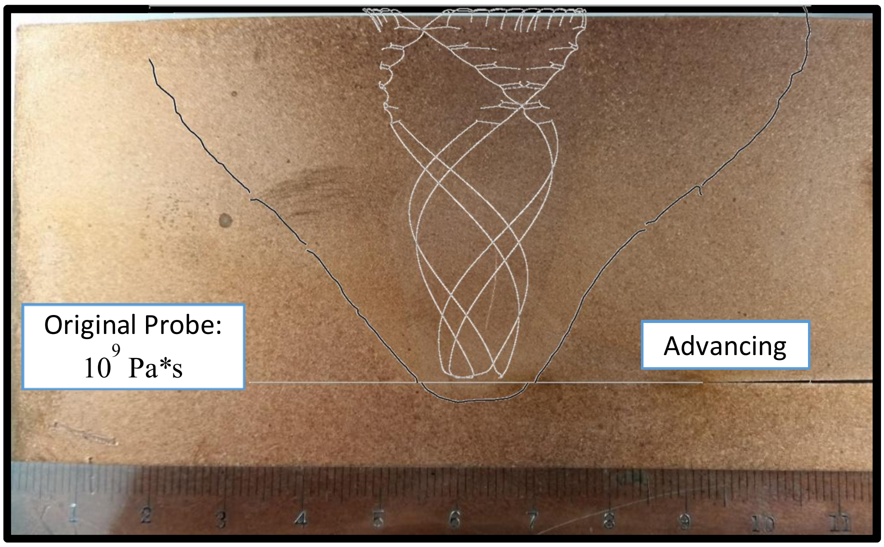

Figure 48: $10^9$ Pa*s viscosity curve plotted on a weld cross section. This curve was selected to best show the transition into a no flow region where the fluid is so viscous is essentially behaves solid.

A constant strain rate curve of 0.01 $s^{-1}$ predicts roughly the same size low flow boundary as the $10^9$ Pa*s viscosity curve. Again, this strain rate curve was arbitrarily selected to be the point where the strain rate was low enough to be considered noneffective on material flow. Though not used for validation, it is interesting to compare the sized of the different flow zones between probes. When comparing the high-flow zones of strain rate of 2 $s^{-1}$ [28] and viscosity of $5^6$ Pa*s [30] both the original probe and probe B exhibit similar sizes. However, when looking at the low flow zones of viscosity of $10^9$ Pa*s and strain rate of 0.01 $s^{-1}$ probe B shows a slightly expanded region near the tip of the probe. Figure 49 outlines these regions for comparison between probes. The red region drawn into the low-flow zones is the expanded region probe B has over the original probe. This information corresponds to other simulation results that show probe B has an increased stirring effect near the tip of the probe. This also means that probe B could have a larger TMAZ and affect the base material more during welding than the original probe design.

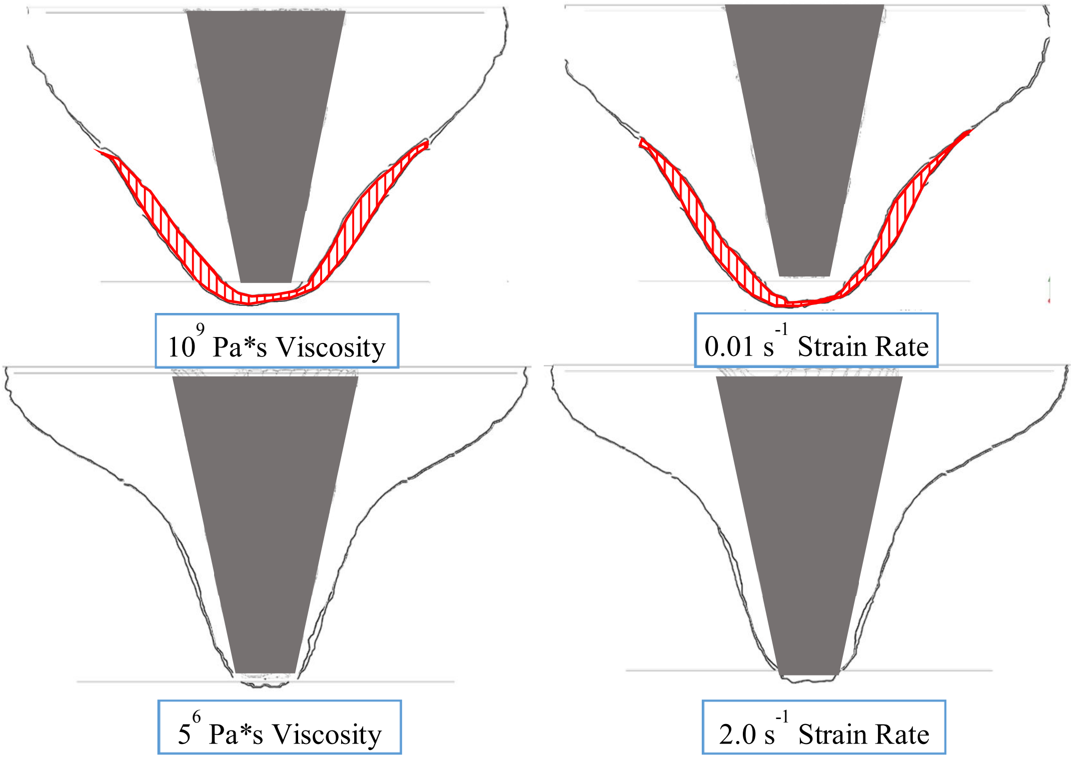

Figure 49: Prediction of the high-flow and low-flow zones for the original probe and probe B. The hashed red region is the increased size of the low-flow zone of probe B.

### 5.2.1 Strain Rate Cracking

Areas of high strain rate are susceptible to cracking due to the impact like nature of the stress they receive. In the CFD simulation, this has no effect on the walls, apart from the shear stress they induce in the fluid. However, in reality, the probe surfaces would share this loading and could either deform or crack if the loading was high enough. The simulation shows very high strain rate concentrations on MX features farther from the shoulder. Farther down the probe, the shoulder has less ability to stir and soften the material, meaning the MX features take the brunt of the loading. Evidence of cracking is seen on the MX features in works by both Nenonen and Cederqvist on the second, third, and fourth MX features. These are the same MX features simulated to have the highest loading, making them the weak point. It should be noted that the magnitude of the simulated strain rates could be unrealistically high due to the no-slip boundary condition.

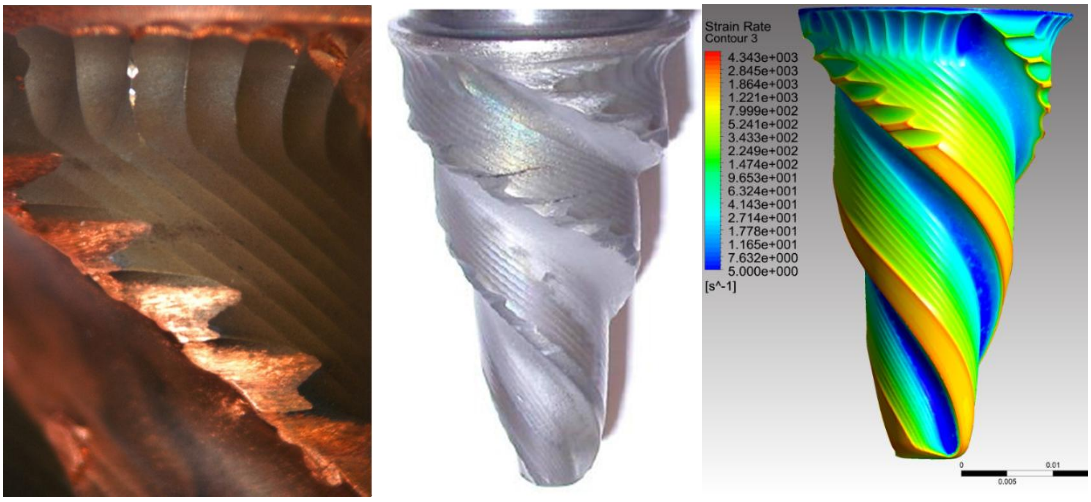

Figure 50: Evidence of possible MX feature cracking from Nenonen [6], Cederqvist [3], and correlation to high strain rates in the simulation.

## 5.3 Pressure

Pressure is the primary way loading is determined in a CFD system. The pressure couples the mass and momentum equations of the fluid, and monitoring the pressure can give key insights into the system. Fluent uses the pressure to balance the velocity and mass conservation laws with all the boundary conditions of the model. Interpreting these pressures can show how the material is behaving in the simulation; comparing this behavior to how the material behaves in the actual FSW process can help validate the model. High-pressure zones indicate areas of high loading on the probe. As the pressure decreases to zero it indicates a stability in the system where no forces are trying to accelerate the fluid. Negative pressure in the simulation means that the conservation equations are creating empty cells. Cavitation, or empty cells, are not possible in this model so the pressure becomes negative to mathematically pull fluid back into the cells, balancing the equations. Realistically a pressure below absolute vacuum is not possible; but, mathematically in a CFD simulation, the negative pressure balances the system.

In this model, a negative pressure occurs on the probe in areas where material slip would likely occur. Because a no-slip boundary condition in enforced on all walls, negative pressure keeps fluid stuck in the cells where slip would naturally occur. This negative pressure can also indicate possible void formations, if consistent negative pressure is found in areas where material slip is not expected. Detecting voids using pressure cues is not ideal, but it can give initial clues to possible problem areas with new design concepts.

By defining an incompressible flow with no-slip conditions at the boundaries, negative pressures are an unavoidable drawback of the current model. Proper interpretation of these pressure zones can give some information on how the mathematics of the model definitions are trying to account for what should be realistically occurring. Fortunately, the mathematical calculations of the model are not bound by reality (negative absolute pressure, pressure below vacuum, is physically impossible) so simplifications like no-slip boundaries can be accounted for. This also allows negative pressure to be viewed as areas where the mathematical model had to correct for errors caused by the simplifications made with the no-slip condition. Ideally, an accurate slip condition would be built into the model; this would also allow friction/sliding heating to occur. Implementing a slip condition of the complexity required for accurate predictions in FSW would be no easy task and the current model still gives valuable information from the pressures.

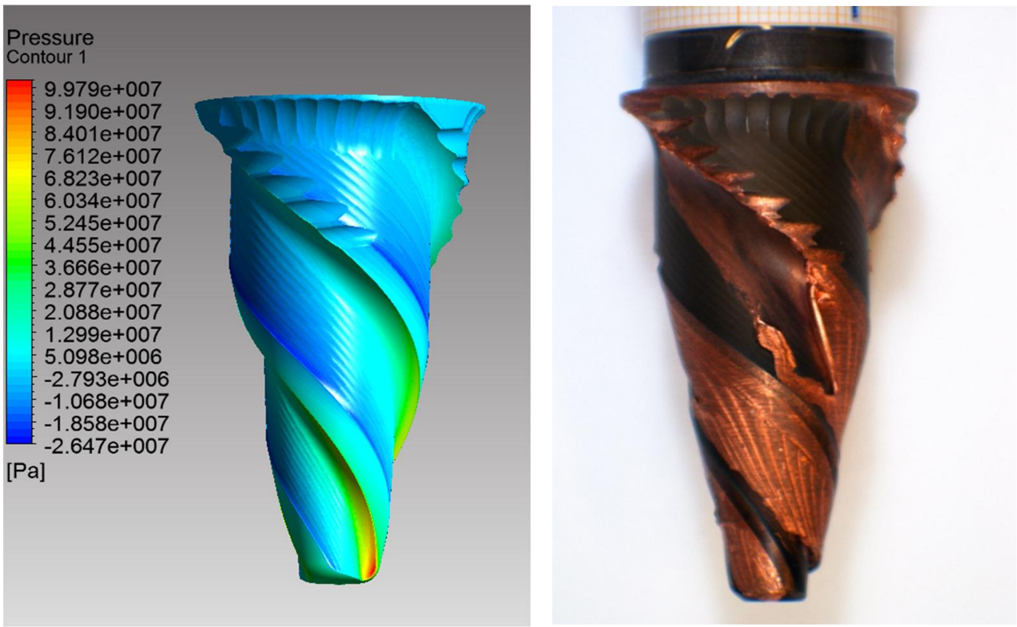

Figure 51: Simulated probe pressures with sliding sticking evidence on real probe.

The pattern for pressure on the probes begins low, usually negative near the shoulder and gradually increases down the probe, with a maximum pressure on the probe tip. The negative pressure along the trailing edge of the flutes is indicative of material slip around the top of the probes. The MX features have high-pressure concentrations on their leading edge and a large negative pressure on the trailing edge, suggesting a cutting-to-sliding transition. A positive pressure forms near the flutes, signaling a change away from sliding material to a more sticking effect. In these regions, material is more likely to remain trapped in the flutes; evidence of this is seen in the regions where material is present on the used probe after removal. Near the tip, the same low-to-high pressure transition occurs from the trailing edge to the flute, but the overall pressure is higher. This increase in pressure comes from a combination of sources, namely increased material viscosity (from lower heat generation and lower strain rates), lower probe tangential velocity, a reduction in material slip tendencies, and geometry changes (pressure localizations).

When compared to the original probe, all other probes tested have more negative pressure off the trailing edge of the flutes. Lower pressures could mean more sliding, and less sticking, material, but also could cause more wear on the probe due to the increased sliding friction. All the new probes also have a higher pressure concentration at the probe tip compared to the original. This increase in pressure is likely caused by a combination of the geometry creating a sharp point, which concentrates pressure, and the increased stirring effect near the probe tip applying more loads to the probe. Of these probes, the OHA has the largest pressure on the probe tip with a peak pressure of 104MPa. The peak pressure at the tip of the original probe is 92 MPa while probe B has a peak pressure of 97 MPa. The peak pressures were always found on the advancing side of the probe, with the retreating side pressures being between 10-15% lower on average. The full length of probes C1 and D1 mimic the effects of the MX features near the shoulder down the length of the probe. They create pockets of higher pressure underneath (in the valley) of each feature and a very low negative pressure off the trailing edge.

## 5.4 Pressure Integration (Forces)

Integrating (summing) the pressure acting on the walls over the walls area is the way Fluent calculates force vectors. Fluent also calculates a force from the shear stress between the fluid and wall, which depends heavily on the boundary conditions. The sum of the pressure and viscous (shear) forces is the reported force by Fluent. These forces can be projected onto any coordinate system and can be used to calculate torques around any axis. Comparing these forces between probes gives more clarity as to the direction of loading the pressure is causing. The Y force direction in the simulation is equivalent to the forging force direction of the actual process. The original probe shows a loss of this force towards the tip, while the new concept increases this force near the tip. This increased force on the new probe increases the forging capability near the tip, but also increases the loading. However, axial loading is the most preferable loading direction for increasing probe life because there is no bending stress, only compressive stress.

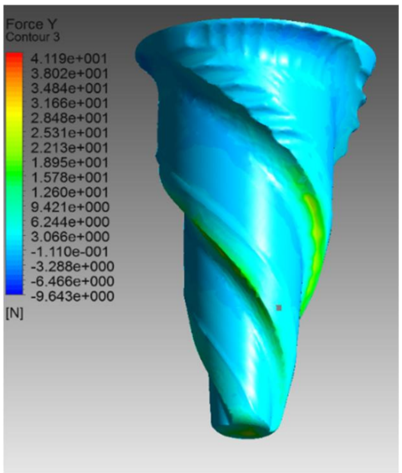

Figure 52: Y force contours (where positive Y-axis corresponds to the vertical axial direction pointing upwards, i.e. from the tip of the probe to the shoulder).

Ideally, these forces could be used to validate the model by comparing them to the forces seen in the actual FSW process. In theory this works, but it needs more refinement to make it more reliable. The biggest issue arises from the model creating negative pressure zones, which cannot exist in reality, that get erroneously included into the force calculations. Fluent primarily uses these forces for reporting the coefficients of lift and drag on airfoils, so their functionality is somewhat limited. Examples of these errors can be seen in Figure 52 where negative Y forces are calculated from the negative pressures off the trailing edges of the flutes and near the shoulder. This creates a force that artificially attempts to pull the probe down into the material, otherwise viewed as a negative lift coefficient from Fluent’s perspective. The no-slip condition, which causes the negative pressure, also creates errors with the viscous forces by forcing fluid to remain stuck to the probe in places where it would normally slip.

The errors in the simulations force calculations, combined with the probes axial nonsymmetry and simplified shoulder, make it impractical for validating the model with the forging force. The actual process forging force is approximately 89 kN [3], while this force varies in the model from 6 kN to 25 kN, depending on the pressure values at the given timestep. A large portion of this inaccuracy is because the force from the shoulder is not considered in the calculation, but the reliability of these values is also questionable. However, the X force, or leading force is a much more reliable calculation. Some of the errors with boundary conditions and negative pressure are still present, but are much less volatile thanks to the radial symmetry of the forces acting on the probe in the XZ plane. Many of the forces in this XZ plane counteract each other due to the spinning of the probe, so the total force is actually the closer to the gradient of pressure acting on the probes leading and trailing faces.

The leading force is important because it relates to the bending stress on the probe; calculating the bending moment the leading force exerts on the probe gives the effective distant of an equivalent single force acting on the probe (by solving M=F*d for distance). Table 8 shows how the model values of the original probe, and probe B, compare to the machine data of the leading force range. The instantaneous values of these forces are very unstable; in both the simulation and actual process they can fluctuate up to 10 kN. The models predicted range of forces for the original probe overlap the machine measurements, given the rapid fluctuations in time, but on average underpredict this force. This is likely due to the errors from the negative force and no-slip condition, plus any drag forces from the shoulder (which are not accounted for in the model). The torque predicted in the model is roughly 40% of the total torque registered by the machine. This is consistent to the results found in the fatigue testing of the ratio of probe torque to total torque. The total torque the machine registers is the sum of the probe torque, shoulder torque, and the torque needed to spin the machine. Overall, the model predicts forces and torques that are within the actual weld process operating window. The forces are reasonable, but somewhat low on average, and the torque fits within the estimates.

Table 8: Leading force, bending moment, axis length, and machine torque.

| | Actual Probe | Original Model | Probe B (new design) |
|---|---|---|---|
| Leading Force | 6.75 kN | 2.05 kN | 1.89 kN |
| Bending Moment | - | 62.7 Nm | 55.3 Nm |
| Effective Bending Axis | - | 30.5 mm | 29.2 mm |
| Machine Torque | 1000 Nm | 385.1 Nm | 397.2 Nm |

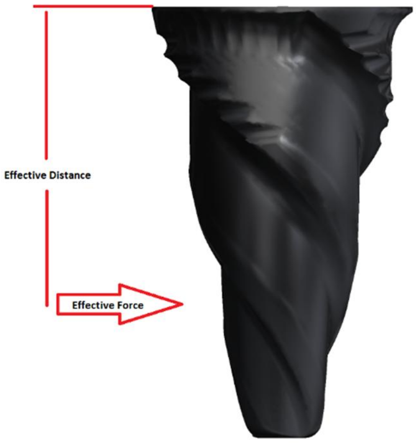

Figure 53: Effective bending axis diagram that characterizes the bending moment of the probes.

The probe B model has slightly less leading force versus the original probe model and an effective bending distance of between 1.0-2.5 mm less (depending on the timestep, the average is 1.3 mm). This implies slightly less bending stress in probe B, which improves probe life and reduces the risk of probe fracture. There is also a force perpendicular to the leading force (in the simulation this would be the Z-axis), that pushes on the probe from the advancing side. If viewed from Figure 53 this force would be pushing the probe into the page. The original probe and probe B both show about a 1.4 kN force for this Z force. Probe B also shows and increase of stirring torque on the probe, this is expected as probe B shows a greater stirring effect. Stirring more material increases the amount of torque required to rotate the probe. While the increased stirring would likely improve weld quality, the higher torque increases the shear stress in the probe and should be accounted for in the new probe design.

In the current model, these forces are all surface loads on rigid (ideal) body. The CFD based model used in this thesis does not account for any internal stresses in the probe. Importing these surface forces into a solid FEM model of the probe could show how the loads that occur during welding affect the stresses inside the probe.

The simulation also shows a cyclical variation in the leading force as time progresses through the transient solution. Figure 54 is a graph of how the leading force sampled at 0.005-second intervals fluctuates through time. One complete revolution is plotted (0.145 seconds) and compared to a linear trend line. The trend line assumes that the leading force should be constant across the three flutes rotation cycle (the forces repeat when each flute crosses the X-plane). This data shows that the X force only fluctuates by approximately 200 N from linear, which is a quite low amplitude when the average force is nearly 2,000 N. A reason why the force may not fluctuate as much as expected is that the force is evenly calculated around the entire surface of the probe, any alternating fluctuations likely would be canceled out by the opposite force on the other side of the probe. Regardless of the reason, this simple look at the dynamic loading shows that different areas/faces of the probe undergo different loading scenarios through time.

The time starts in Figure 54 when the first flute is directly parallel to the X-plane. One full rotation means each flute will cross through this plane once; these times are the red dots on the graph (.050 seconds apart). As the selection when time “starts” is arbitrary, these times were selected for graph clarity as they are the times when the leading force is the lowest. As seen from the graph, a cycle repeats every 120° of probe rotation, as each flute passes through the X-plane. The cycle alternates between local minima and maxima ever 30°, creating a pulsing force that has a frequency of twice the flute angle. Further investigation into the dynamic loading phenomenon could be done with more detailed analysis of the CFD model (perhaps exporting planar forces only, for differentiating between X shear force and X bending force), or by using a transient FEM solid model.

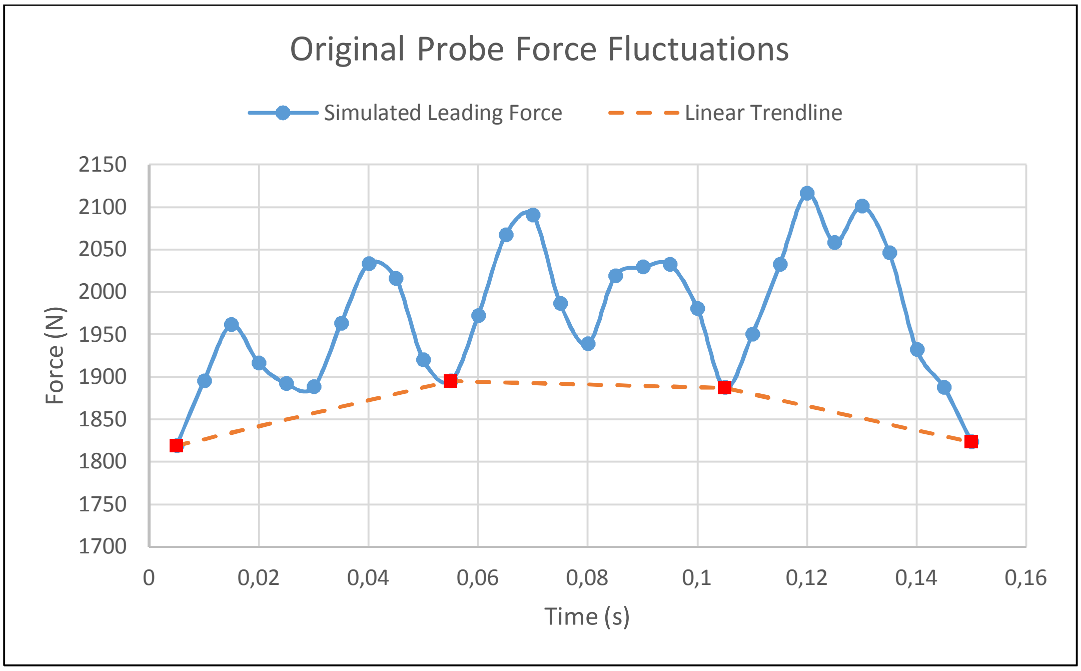

Figure 54: Original probe force fluctuations through one full rotation. The dotted line is a linear tread line assuming that all three flutes have similar constant forces. The red dots are the times when each of the three flutes reaches the same position.

# 6 Probe Comparison Results

## 6.1 Introduction

The use of a reliable model to compare design changes can accelerate the development cycle and reduce costs. Analysis of the simulation results of the current probe, and probe concepts created by the analytical design of Nenonen [6], can find the strengths and weakness of each design. While no probe simulated was perfect, the goal to minimize the weaknesses of the current probe showed how optimization through simulation is achievable. In total nine different probes were simulated to different extents, with the original probe and probe B simulated the most.

Comparison of these results gives an idea of whether a new concept performs better than the current probe and which variation performs the best overall. Evaluation of three major categories of probe characteristics determined the performance of the different probe designs. The material flow properties, heat generation (from deformation only), and viscosity of the material show how each probe behave.

A majority of the work done in this thesis was the setup and development of the model, with most of the simulations vetted on the original probe only. An older version of the model, with less mesh accuracy was developed prior to the final revision of the model and some of those results are included as well. This older model was primarily used for the initial comparison of the most promising new design concept, probe B, to the current (original) probe design. The results serve as a proof of concept for simulation based design improvements. The results from the more accurate final model mimic those of the original model but have greater resolution and are less prone to mesh quality errors. Also, any probes other than probe B and the original were only simulated in the final version of the model. These additional probe simulations show that the effect of very small probe geometry changes can be seen in the simulations, allowing for the possibility of further optimization of the probe design without the need for experimental trials of every design revision.

The power with using a comparative approach to improving the probe is that the model does not have to perfectly simulate the FSW process in order to be useful. A reasonably accurate model will give enough data to say which probe is better, even if there are errors when comparing the simulation to reality. As long as both simulations are ran using the same conditions, the error in the simulation can be assumed to affect both probes equally. For example, if a pot of 100° C boiling water is in 20° C room, while a thermometer reads 102° C for the water, and 22° C for the room, it is still easy to say that the water is 80° C hotter than the room regardless of the thermometer error. Of course, FSW is much more complicated than a thermometer, but the concept holds true as long as the simulation maintains reliability and relative accuracy.

With a FSW simulation there is such an abundance of phenomena to evaluate that often finding the critical elements becomes difficult. Post-processing of the results gives quantifiable values and qualitative comparisons to the key elements of the results. It is important to find the specific properties that prove both the reliability of the simulation and are significant to the design criteria. CFD-Post was the Ansys software used to post-process the raw results into more useful information. The criteria evaluated in this section focus on the performance of the original probe's weakest areas and how the new probe design (probe B) improves those areas. This is especially true near the probe tip. While the velocity characteristics, heat generation and viscosity profiles were considered the critical criteria for probe evaluation there are more properties available for analysis than are presented in this section.

## 6.2 Velocity Characteristics

The velocity of the fluid serves as one of the primary methods for characterizing the material flow properties during FSW. With full 3D flow, the velocity profiles can get very complicated very quickly, so some tools have to be used to simplify the flow field for evaluation. While analyzing the velocity characteristics for the entire simulated domain is possible, such a macroscopic view tends to wash out important intricacies within the simulation. Using reference locations such as planes, lines and surfaces gives a clearer, and simpler, picture of what is occurring within the simulation. However, these simplifications are only useful in the areas that are critical to the evaluation of the design changes. This velocity analysis centers on the magnitude and direction of the fluid velocity near the probe. Very far field results are not as useful, or accurate, in this simulation due to the lack of particle tracking in this model, so the focus was on what is occurring near the probe instead.

### 6.2.1 Velocity Streamlines & Vectors

The best use of streamlines, and vectors, are representing the overall 3D flow patterns; they can be sampled from the entire domain, a selected region, or a reference location. Streamlines represent the path a massless particle would take through the fluid at a given time. This is not to be confused with transient particle tracking through each timestep (an addition discussed in future work). A better representation for streamlines is a "snapshot" of how particles would behave if time were frozen at that instant. Streamlines are useful for a general view of how the fluid flow field is behaving and for confirming that the simulation is behaving as expected. Figure 56 represents the release of streamline particles from single lines parallel or perpendicular to the probe axis. Each streamline represents a single particle path and is constant colored, blue near the shoulder and red near the tip; the short blue-to-white streamlines represent the XZ plane distribution tendencies of the particles around the probe.

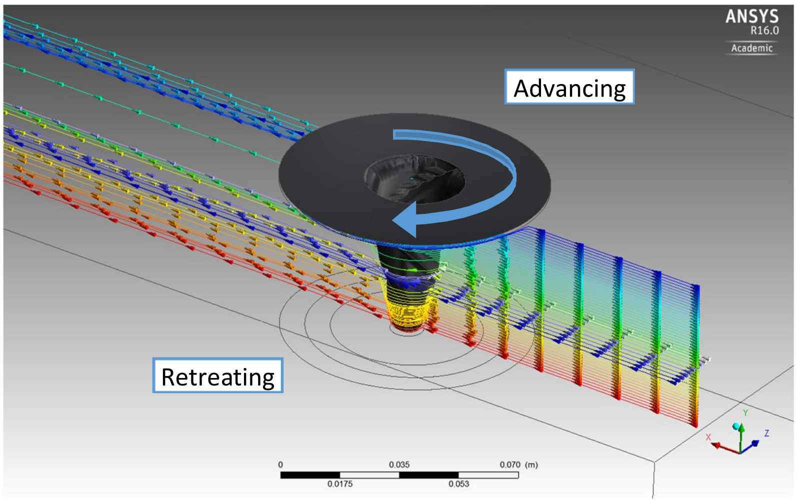

Figure 56: Original probe streamline example.

Analysis of Figure 56 shows the expected pull of fluid from the advancing to retreating probe side, without much stirring in the far field and heavy stirring of the fluid near the probe. The streamlines show clear 3D flow, with an upward and advancing side shift of fluid near the shoulder and a radial tendency near the tip. While there is axial (Y direction) velocity present, the streamlines show that the stirring velocity (XZ plane) is of much greater magnitude on average. Viewing the streamlines from the axial (Y) axis gives a projection of the overall stir quality of the probe. By comparing the original probe and probe B, it is possible to see that probe B appears to have more of a stirring effect overall. Figure 57 is a representative image from a single timestep showing the increased stirred zone and particle diffusion of probe B.

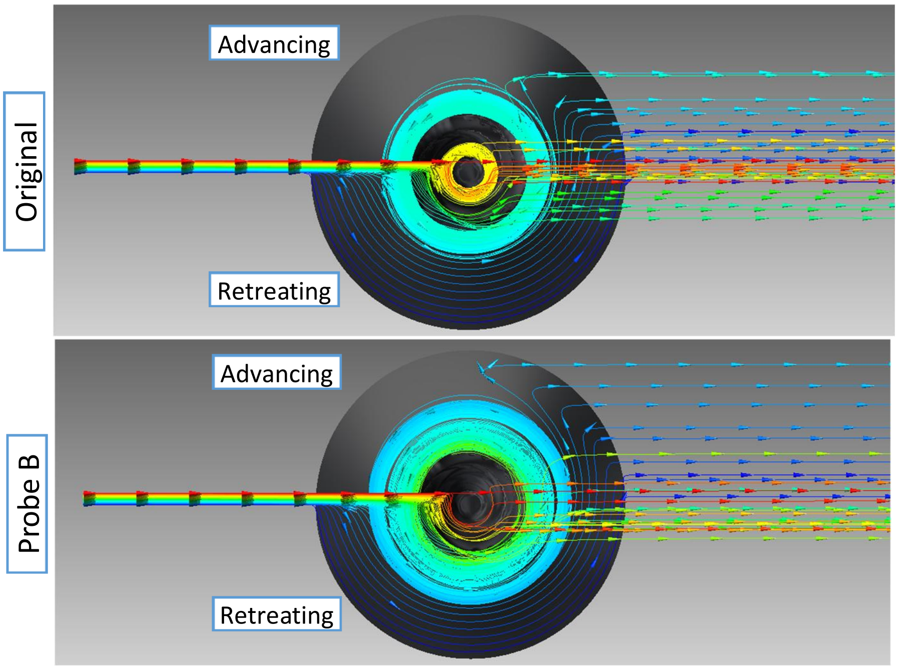

Figure 57: Streamline comparison, viewed axially from the tip up.

In this application, streamlines are only useful for finding general patterns, because they are very dependent on mesh quality and the timestep. In general, the overall flow fields appear to be quite similar in size between the probes, given the obvious geometry changes. Predictably, both probes behave identical near the shoulder, because no design changes occurred in this region. Looking along the probe length it is possible that the different probes have changes in velocity magnitude but it is difficult to determine using streamlines. Sampling vectors of 3D velocity magnitude off a reference plane gives a clearer picture of the changes occurring along the probe length. The sample plane travels up from the tip (reference of 0 mm) to the shoulder (50 mm) taking cross-sectional slices of the probe and velocity vectors. The sampling size of the plane is a circle offset 33% larger than the cross-section of the conical probe at the given height. This offset captures the highly stirred zone near the probe plus any slowly moving zones slightly farther away from the probe surface.

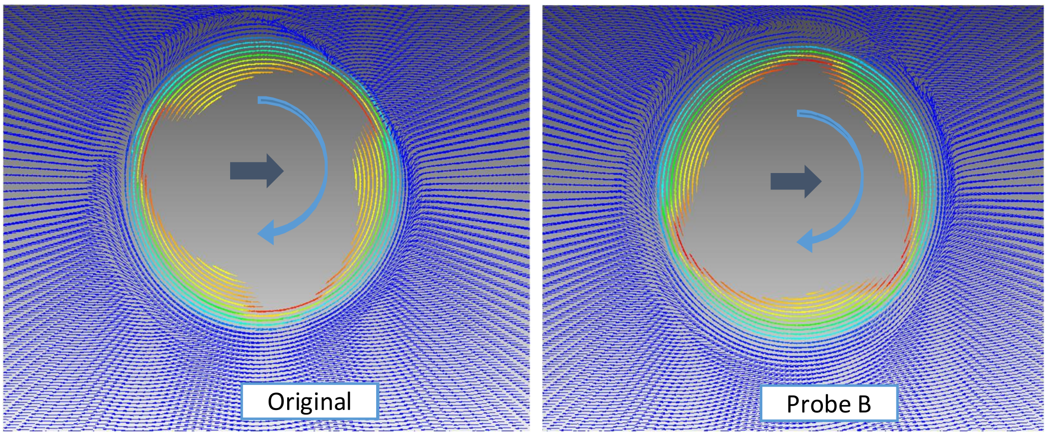

Figure 58: Cross-sectional plane velocity at 10 mm above the probe tip. Notice the increase in size of the stirred zone of probe B compared to the original.

Comparing the average magnitude of the velocities along this plane tells how well the probe moves fluid. The points on the graphs in Figure 59 represent the average fluid velocity on the plane in 1 mm increments. Probe B has a small increase in velocity magnitude from the probe tip up to approximately 35 mm. This increase is relatively small, between 4 $\frac{\mathrm{mm}}{\mathrm{s}}$ and 6 $\frac{\mathrm{mm}}{\mathrm{s}}$, compared to the overall velocity magnitude, but shows a clear increasing trend closer to the tip of the probe. Lower average velocity near the tip further amplifies the effect of the increase in velocity magnitude of probe B, with over a 10% increase in velocity magnitude under 10 mm above the tip. While this observation does not definitively make the probe B design better than the current design, it does show that the probe B geometry is more effective at moving fluid.

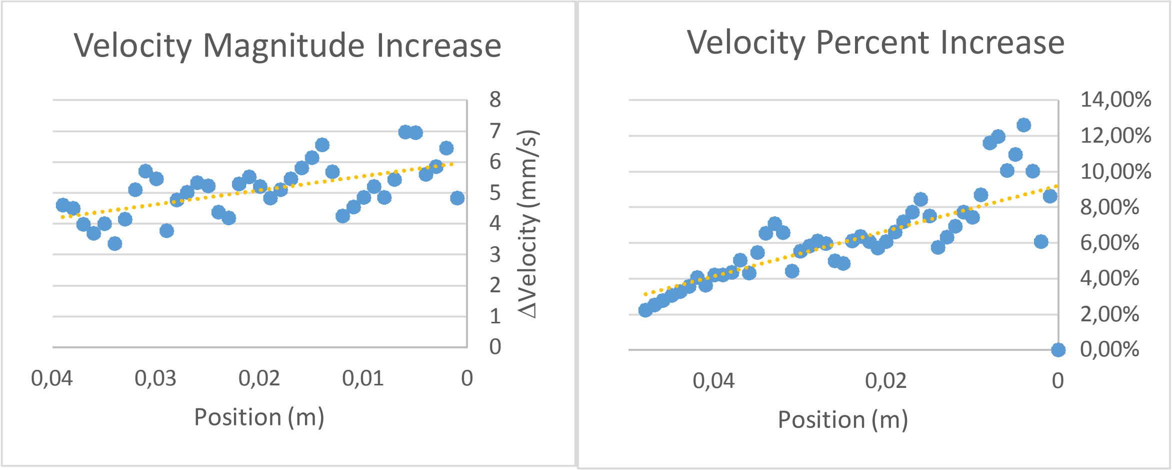

Figure 59: Comparative velocity magnitude graphs.

### 6.2.2 Axial Velocity Contours

Increasing the forging (axial) force the probe applies to the material near the probe tip was one of the primary reasons for the new designs. The axial velocity (Y velocity) of the simulation can represent this forging ability of the probes. Contour plots are the most effective tool for isolating and representing the axial velocity results. Contour plots on a surface of revolution (SoR) within the probe flutes and cross-sectional planes bisecting the probe are used in this work.

Creation of a conical SoR slightly smaller than the probe dimensions allows the investigation of the velocities inside the probe flutes. A contour plot of only the Y velocity eliminates the radial XZ velocities that would normally wash out the axial velocity. As the goal is to have a downward velocity, pushing fluid toward the tip, the scale of the plot is capped at zero as the maximum. This eliminates the unwanted shift of the scale caused by the MX features creating an upward velocity. The zero velocity seen where the SoR contacts the probe surface is caused by the no-slip condition present for all walls.

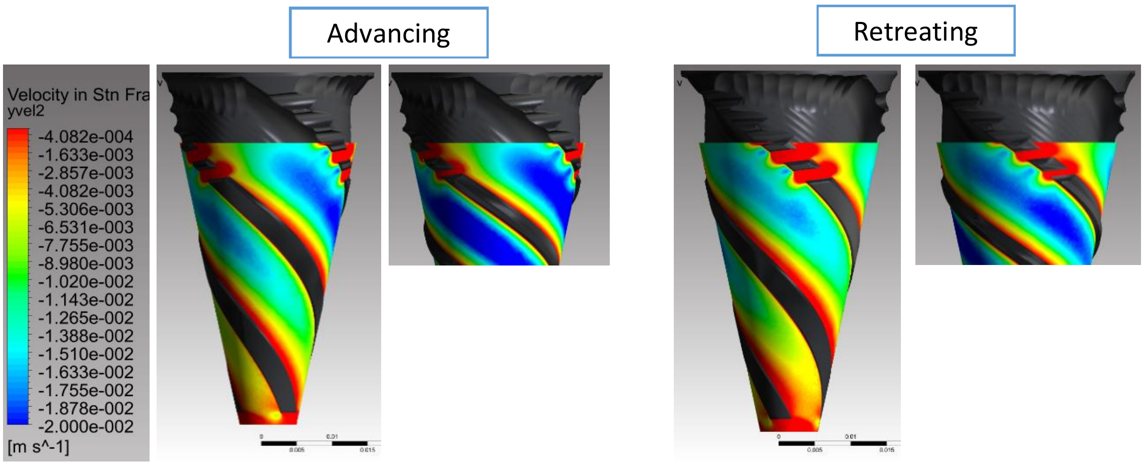

Figure 60: Fluid axial velocity on SoR inside the probe flutes viewed from both the advancing and retreating sides; Original on left and probe B on right.

As seen above, both probes exhibit a decrease in axial velocity from the shoulder to the tip. Near the tip the original design has almost no downward velocity, this is very clear on the retreating side image. Explanation for the decreasing velocity is the increasing helix angle in combination with a decreasing overall velocity. Decreasing probe volume near the tip causes less material flow and is unavoidable with conical probe profiles (cylindrical probes combat this problem but are unrealistic for this application). However, the helix angle from the original probe clearly causes a much large loss in axial velocity over probe B. Probe B maintains much better axial velocity, and by relation, forging force along the length of the probe. This increase in the forging force could lead to better mixing of material, reducing the risk of the poor mixing seen back in Figure 19.

Figure 61, a planar view of the axial velocity around the probes, excellently shows how different the forging force profiles of the two probes are. One characteristic present in both probes is the loss of axial velocity on the retreating side. This is most likely due to the tangential velocity of the probe moving away from the direction of travel, reminiscent of a helicopters dissymmetry of lift. The original probe loses almost all of its downward velocity near the tip, tending to push the material radially instead. Probe B maintains nearly constant downward velocity all the way to the tip. This downward velocity translates into a much more constant forging force near the probe tip, but could lead to some problems as well. On the flute tips of probe B there is a concentration of upward velocity from material being whipped off the probe surface, which could cause void formation. The sharp flute radius and non-vertical flute faces block downward flow and create a ramp-like zone for upward fluid flow. Nenonen previously discussed this as one of the possible flaws with an OHA angle design [6] and the simulation confirms it.

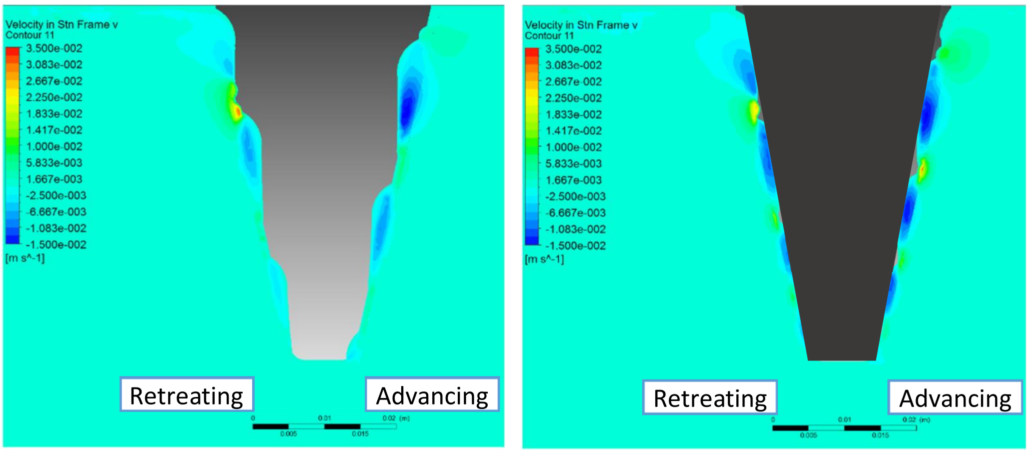

Figure 61: Cross-sectional axial velocity contours of the original (left) and probe B (right).

By comparing the nine different probe designs, it is possible to see how the geometry changes influence the vertical velocity patterns. Of all the probes simulated, the original design has the lowest downward velocity flow, but it also has the lowest upward flow and most uniform flow pattern. This uniform pattern is due to the free path of the flutes down the length of the probe. The OHA probe has large pockets of downward flow thanks to its large, screw like flutes. However, these flutes overlap and create “bubbles” of downward flowing material trapped in place by the overlapping flute underneath. The probe also has the highest amount of ramp like vertical flow off the edges of the flutes due to their very sharp radii. It is unknown if these issues would actually cause imperfections during welding; regardless, other probe designs show better flow characteristics and have other benefits (such as more strength).

The changing helix angle of probe A and probe B help reduce the flute overlap and allow for a more free downward flow path. These two probes have very similar flow patterns, which is expected as the only difference is that probe B a slightly different profile than probe A. Both of these probes show vertical shedding off the flute tips, the amount is less than the OHA probe but is still much more than the original design. Probe B1 had very little effect on the downward flow. Changing the probe profile, such as in probes C & D, helps reduce the vertical shedding of material off the flute tips by increasing the flute radius. This increase has very little effect on downward flow, although probe D does begin to show some reduced flow near the tip due to the increasing size of the inner tool body[3]

Of the probes simulated, probes A, B and C appear to have the most acceptable axial flow. All three of the probes maintain good downward flow throughout the length of the probe and the only noticeable area of concern if the vertical flow off the flute tips. However, this could become a nonissue if this upward flow does not create voids in these areas during welding. When compared to Nenonen’s analytical analysis (see section 2.4.1) [6] probe B has the advantage, with probe A being slightly less strong and probe C slightly less efficient.

## 6.3 Viscosity & Strain Rate

The viscosity and strain rate are inversely related by the nature of the Sheppard-Wright material model. Both of these values are very difficult, if not impossible, to measure during the actual FSW process but are very important to weld quality and probe life. This section will compare simulation results only; more analysis relating the viscosity and strain rates to probe evidence is in the model validation section. High viscosity regions near the probe highlight areas where the strain rate is low and material does not flow easily. Accordingly, high strain rate zones relate to places were the viscosity is low. Figure 63 shows the viscosity patterns on both probes, notice that the maximum viscosity is limited to $10^6$ Pa*s to clarify the results, as the maximum global viscosity is much higher.

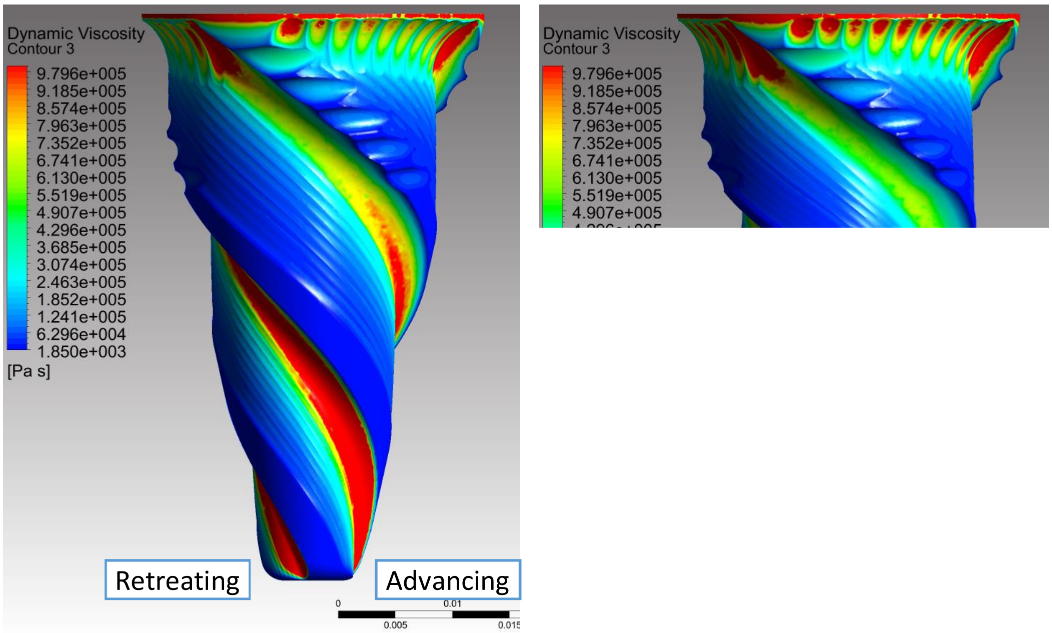
Dynamic Viscosity
Contour 3
9.796e+005
9.185e+005
8.574e+005
7.963e+005
7.352e+005
6.741e+005
6.130e+005
5.519e+005
4.907e+005
4.296e+005
3.685e+005
3.074e+005
2.463e+005
1.852e+005
1.241e+005
6.296e+004
1.850e+003
[Pa s]
Retreating
Advancing
0
0.01
0.005
Dynamic Viscosity
Contour 3
9.796e+005
9.185e+005
8.574e+005
7.963e+005
7.352e+005
6.741e+005
6.130e+005
5.519e+005
4.907e+005

Figure 63: Probe viscosity patterns viewed from the front, original (left) and probe B (right).

The original probe has a high viscosity channel all the way down the probe length. Near the shoulder, this channel transitions into a low viscosity region approaching the MX features, but near the tip this high viscosity region takes up almost the entire flute length. This illustrates that a pocket of high viscosity fluid could remain stuck in the flute, creating a pushing effect instead of a forging/stirring one. Probe B has a similar viscosity pattern near the shoulder (as expected because no design changes occurred there) but transitions into a lower viscosity region towards the tip. There is still a high viscosity region very near the probe tip on probe B, but the region is much smaller. This transition is caused by an increase in the strain rate from the greater material flow probe B has near its tip. This increase in strain rate also increases the heat generated from viscous dissipation, further reducing the viscosity.

When comparing all nine probes it is possible to see how different geometry features and probe profiles affect the viscosity of the fluid near the probe. Just as in the above figure, the viscosity is limited to $10^6$ Pa*s as the global viscosity reaches $4^{10}$ Pa*s (the simulation's upper limit) in the far field fluid. The OHA angle probe has the lowest viscosity down its length, indicating the highest stirring effect. This is reinforced by the results of the velocity contours as well, which show a large amount of fluid moved by this probe. However, as stated before, this probe is unrealistic for application. Of the more realistic probes, probe A behaves most like the original design, with a relatively large high viscosity region near the probe tip. Probe A is improved over the original, but probes B, C and D all have better viscosity profiles.

Probe B has much lower viscosity almost completely down the length of the probe, with a high viscosity region occurring very near the tip. Probe B1 does change the viscosity patterns near the shoulder, but the viscosity in that region is already so low due to the high shear stresses that the effect is barely noticeable. The removal of the MX features could affect the frictional component of viscosity but frictional effects were not accounted for in this model. Probe C shows slight improvement over probe B and probe D, with almost no high viscosity regions. This shows that either too thin or too thick of a probe can have a negative influence on the material flow. Probes C1 and D1 do slightly change the viscosity patterns by further lowering the viscosity in areas of the flutes near the MX features.

By combining these results with the analytical analysis [6] it can be determined that probes B and C are the most acceptable. According to the simulation, probe C would have the slight advantage over probe B, but probe B creates almost as good viscosity profiles with better analytical results. These results also show while both probes are an improvement over the original design, neither are necessarily fully optimized. Perhaps finding an optimal probe curvature, somewhere between B and D, and a proper helix angle transition could lead to a probe with better viscosity characteristics than probes B or C.

The strain rate contours show a mirror image of the viscosity and gives clarity to which sections of the probe undergo the highest stress. The MX features of both probes show very high strain rates, which does not affect the ideal walls of the simulation, but is a stress concentration point in reality. At the top of the probe, around the shoulder-probe interface, the strain rate is low (and viscosity high) signifying a low flow zone in this region. The MX features attempt to increase the flow in this region but have their own problems as stress concentrators. Ideally, removal of the MX features would be possible, but some design improvements would have to be done to improve the flow and heat generation in this region to keep flaws from forming here.

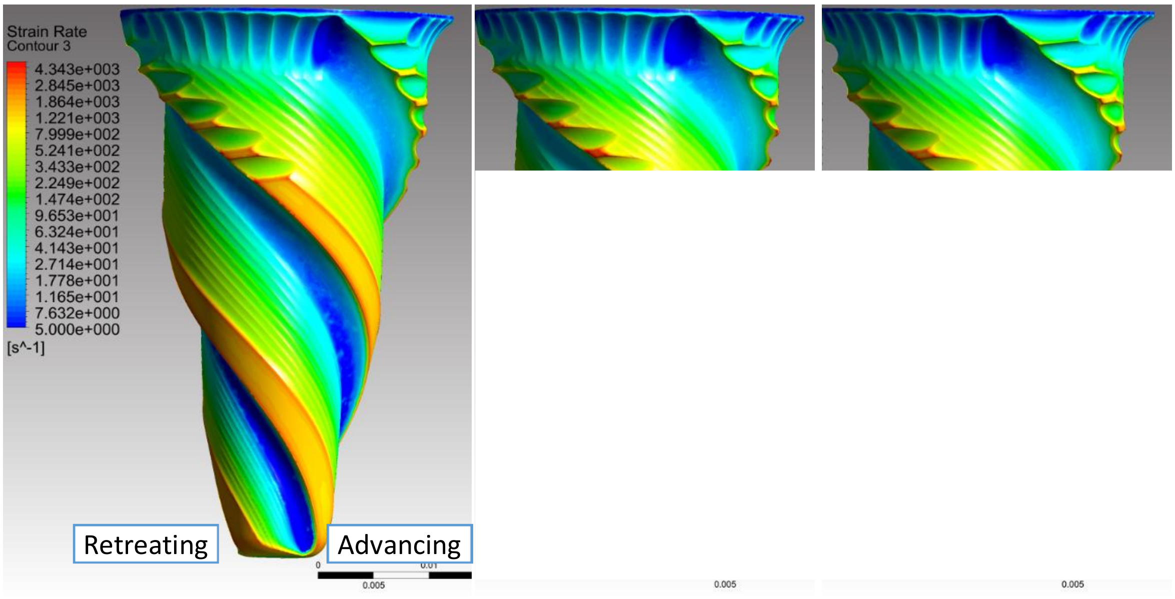

Figure 64: Probe strain rate patterns; original (left), probe B (middle) and OHA (right).

Both probes show high strain on the cutting edge of the flute and along the flutes trailing edge. Probe B has higher strain rates on average in this region due to its decreased surface area along the cutting edge. This does increase the flow of the material, but could also increase the stress in the probe. Probe B also has a strain rate concentration at the tip of the probe where the flute terminates into a very small point. This indicates that a stress concentration at the very tip of probe B is likely, which could lead to deformation, or cracking, at the probe tip. The original probe maintains a large surface all the way to the probe tip so this concentration is not present. The OHA angle probe is included in Figure 64 as it has the most different flute edge and the worst stress concentration. Revision of this region in order to smooth out this geometry feature could further improve the probe design and reduce the risk of probe tip cracking or fracture.

## 6.4 Heat Generation

The heat generated by the probes in the model is another way to understand how well material is flowing around the probes. As mentioned before, all heat generation in the model comes from viscous dissipation caused by the shear forces in the fluid. With a no-slip condition on all walls, no frictional heating, and dummy variables for heat transfer balance, the heat generation of the model is the governing system least based on the actual FSW application. In addition, a reduction of scale to the strain rate dependence term of the viscosity equation was required to keep the no-slip condition of the walls from producing abnormally high temperatures on the tool/material boundary. The ideal way to resolve the heat generation equations would be to implement a proper tool/material slip condition. Successful implementation of tool/material slip conditions is possible but requires careful consideration of how the tool surfaces contact material. Developing a tool/material slip condition for probes as complex as the ones modeled in this work would be a demanding task (discussed as a possibility for future work). For creating an accurate-as-possible model, a tool/material slip condition would be valuable. However, for comparative modeling using a reasonably accurate model, which is the focus of this work, the benefit of a tool/material slip condition over the present solution is arguable.

The model creates temperature fields that radiate from the shoulder down and the probe outward. Figure 65 is a representation of the original probes temperature field. On average, there is a small increase in temperature on the retreating side of the probe. Near the shoulder, the temperatures of the probes are slightly higher on the advancing side, due to the higher shear stress. This effect diminishes down the length of the probe and the steady state temperature near the probe tip is nearly even around the probe, these effects can be seen more clearly in Figure 67. The temperatures of the simulation were compared to the process control temperature of 845±10 °C [3] to confirm the relative accuracy of the heat generated. The process control temperature uses the weighted average measurements of thermocouples placed in the probe and shoulder locations shown in Figure 65. As a solid probe and shoulder do not exist in the simulation domain, only approximate temperatures could be compared. This meant an average temperature estimate to confirm the model was operating within the correct window was needed. The average of the temperature samples from the nearest possible positions to the thermocouple placement (the blue arrows in Figure 65) in the simulation was 882 °C. This is an over prediction of 37 °C above then nominal operating temperature.

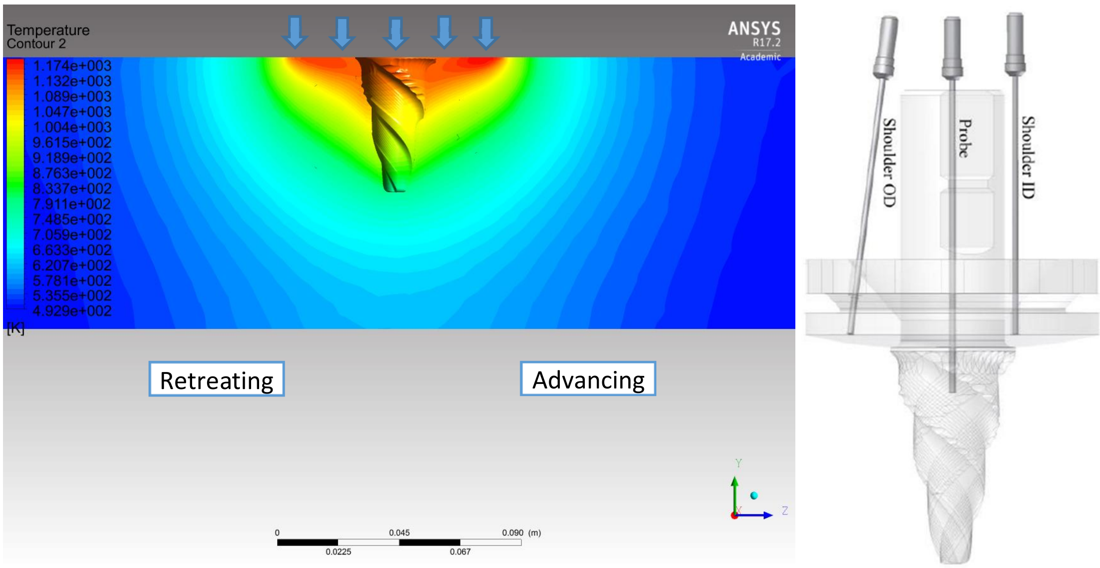
Temperature
Contour 2
1.174e+003
1.132e+003
1.089e+003
1.047e+003
1.004e+003
9.615e+002
9.189e+002
8.763e+002
8.337e+002
7.911e+002
7.485e+002
7.059e+002
6.633e+002
6.207e+002
5.781e+002
5.355e+002
4.929e+002
[K]
ANSYS
R17.2
Academic
Retreating
Advancing
Y
Z
0
0.045
0.090 (m)
0.0225
0.067
Shoulder OD
Probe
Shoulder ID

Figure 65: Simulated original probe temperature field viewed from the front, and sampling points (blue arrows) to compare to actual probe thermocouple placement [3].

Visually comparing temperature fields between probes is difficult because the fields look very similar and the changes in temperature are relatively small compared to the overall temperature. This causes the changes to become indiscernible on contour plots. A remedy for this problem was to plot the temperature along three lines running parallel to the probe angle (Figure 66). These lines sampled the far, mid, and near field advancing and retreating side temperatures of the probes from the shoulder to the tip.

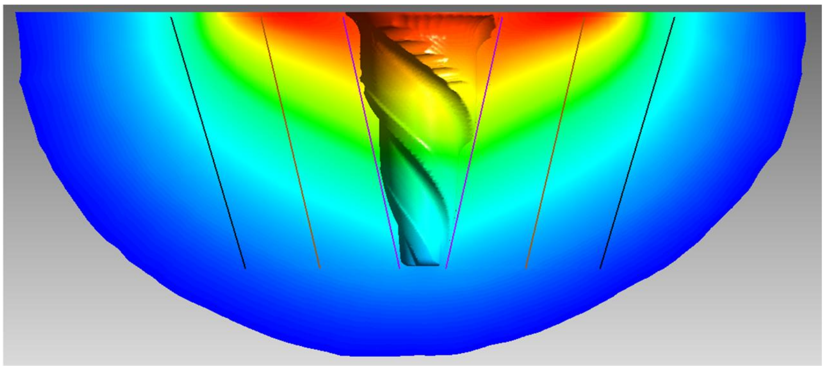

Figure 66: Diagram of temperature sample lines: near, mid, and far

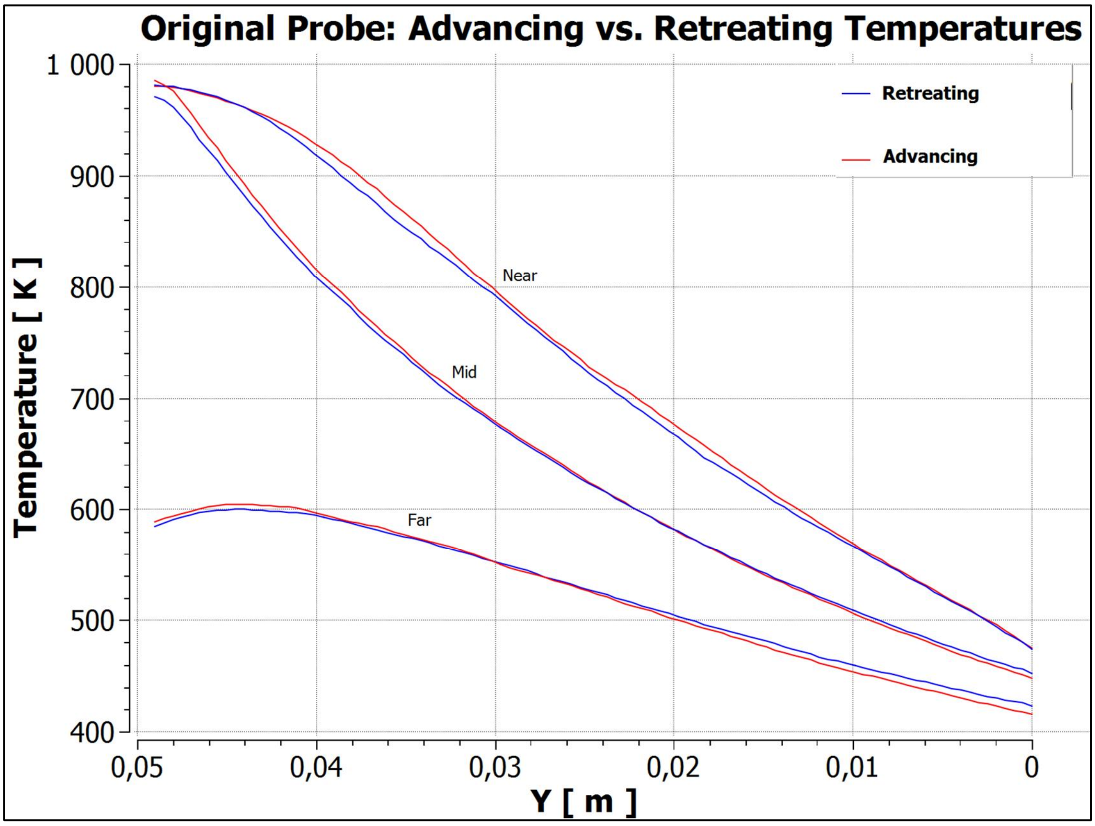

Figure 67: Advancing vs. retreating side temperatures of the original probe. Y height of 0.05 m corresponds to the shoulder and 0 m to the tip.

Plots of these lines showed the changes in heat generation patterns between the probes in Figure 68. These lines show that probe B has very similar temperatures near the shoulder for both the near and mid lines, but shows consistently higher temperature on the far line. As the shoulder and upper probe geometries between the models remained unchanged, this difference in far field temperature seems unreasonable, and the reason behind this variation is unknown (perhaps mesh interface issues at the shoulder boundary). On both the near and mid lines probe B generates more heat down the length of the probe, maximizing this effect near the tip. Probe B had between 15-20 °C higher temperatures over the original design, implying more effective stirring. This increase in temperature softens the material, which lowers the impact stresses imparted on the probe and could improve the material flow properties. However, higher temperatures also reduce the strength of the probe material, likely more than the softer copper will reduce the load. This could decrease the reliability of the probe.

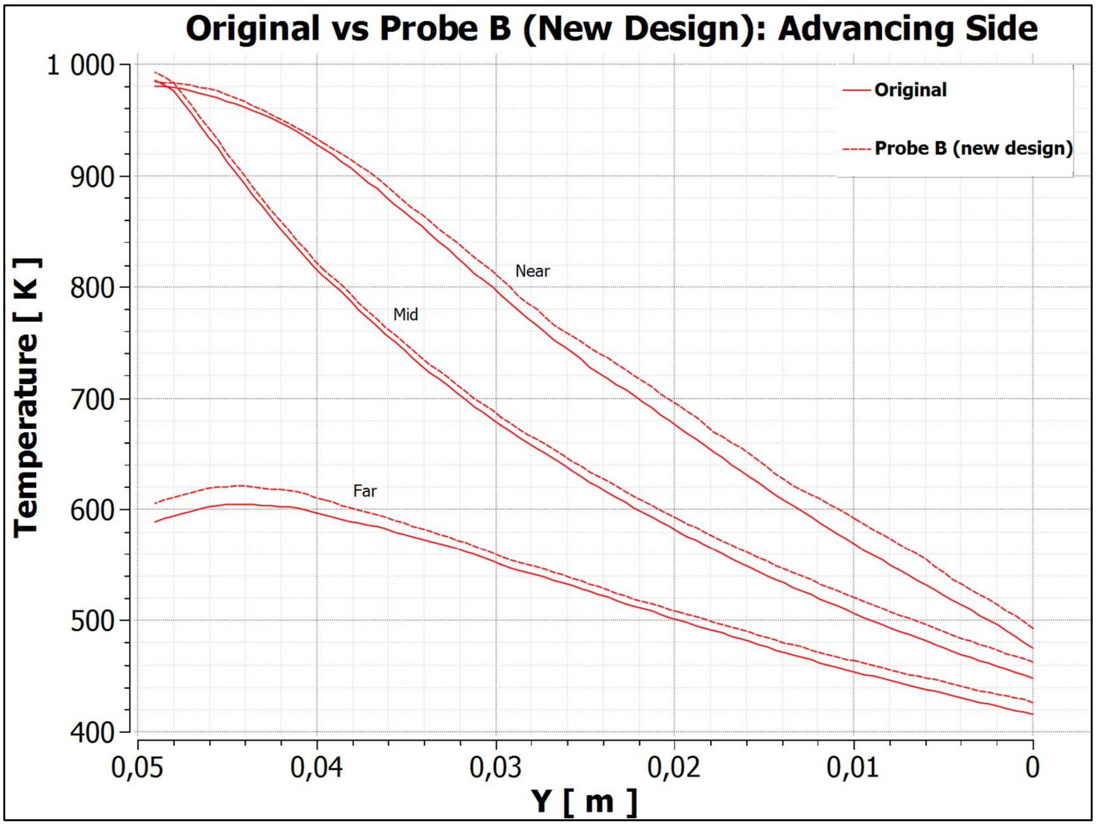

Figure 68: Original and probe B (new design) shoulder to tip advancing side temperature comparison. Y height of 0.05 m corresponds to the shoulder and 0 m to the tip.

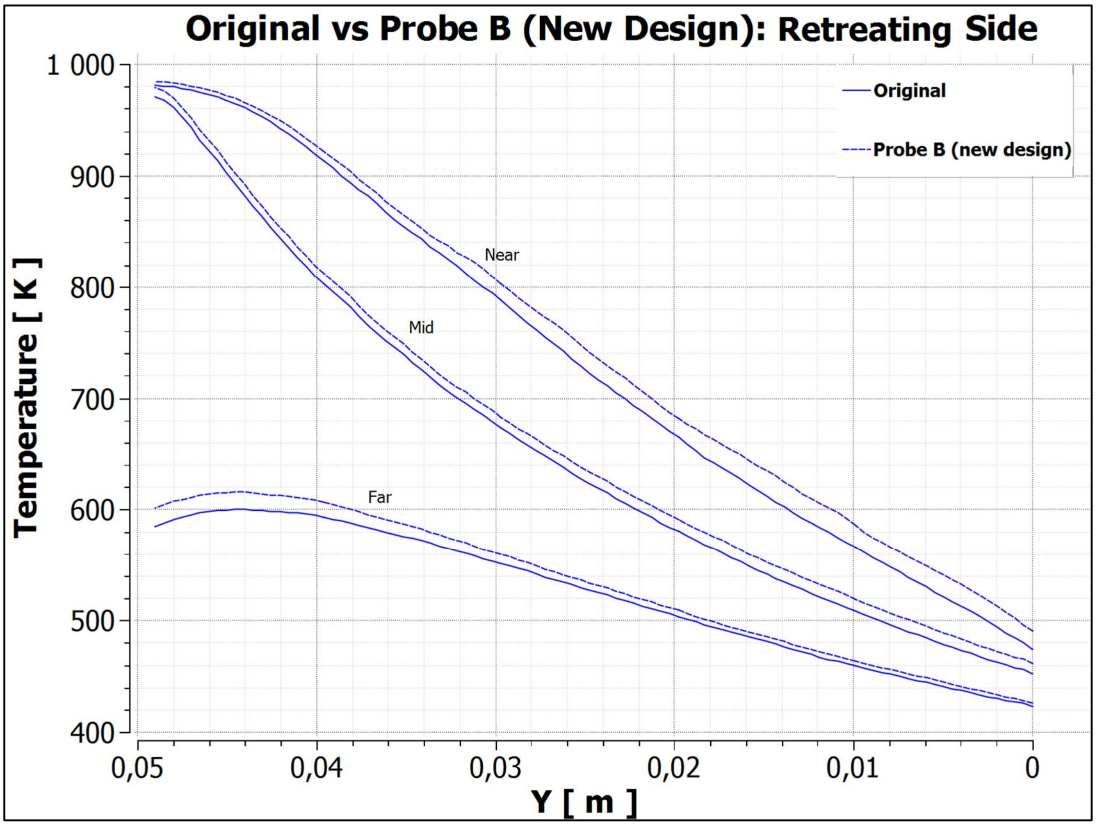

Figure 69: Original and probe B (new design) shoulder to tip retreating side temperature comparison. Y height of 0.05 m corresponds to the shoulder and 0 m to the tip.

# 7 Low Cycle Fatigue Material Testing

## 7.1 Introduction

Development of a LCF test that is based in a FSW environment will allow for the analysis and evaluation of how different material choices behave during FSW. Many material data sheets include important material properties, like tensile strength and toughness at different operating temperatures. However, these properties are measured in conditions quite different from the reality of FSW making them difficult to directly relate to the performance of the material as a FSW probe. The goal of this LCF test is: i) to have the combined effects of thermal stresses and all the loadings present in FSW (torsion, alternating bending, and axial compression, plus vibration and impact); and ii) assess the cumulative damage and influence of all the different stages during the FSW cycle, namely the plunging, dwell and travel periods. Standardized 10 mm long, and 8 mm diameter, conical test probes with a constant 12.5° cone angle serve as the test samples. A 2 mm wide circular notch cut into the top of the probe acts as a stress concentrator, creating a preferential fracture zone. Three 0.2 mm flats cut into the probe induce vibrational and impact stresses.

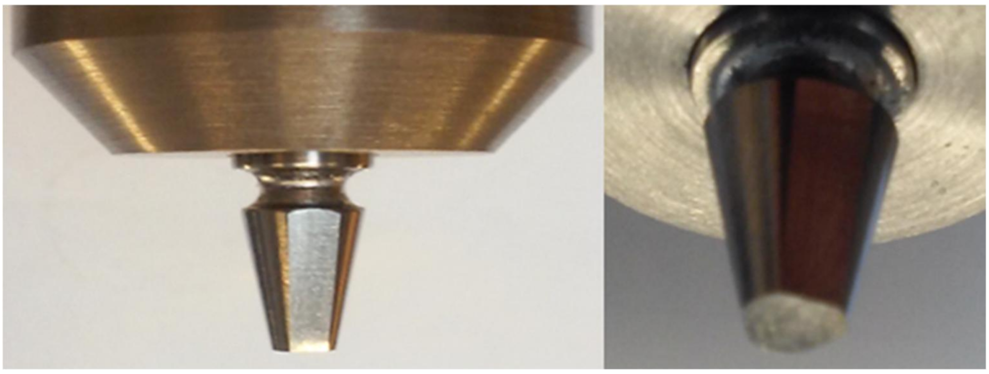

Figure 70: Representative LCF test sample. [6]

A custom shoulder and tool body were made specifically for use in the LCF. The tool body was made to fit the FSW machine present at Aalto University. The main FSW machine features are:

- ESAB LEGIO FSW 5UT (date of installation: 2014)
- Z-axis Control: Position, Speed, & Force
- Maximum Forces: Fzmax = 100kN (Fxmax = Fymax = 40kN)
- Maximum Welding Travel Speed: Vxmax = Vymax = 4m/min
- Maximum Spindle Power = 30kW; Maximum Spindle Speed = 3000rpm
- Work Envelope (XYZ) : 2000 mm x 400 mm x 300 mm
- Special focus on the application to: HSSteels, SSteels, Al, Cu and Ni based alloys
- Multipurpose clamping table (1000 mm x 600 mm) with cooled anvil + cooled clamps + Pre-heat induction capacities
- Shielding gas system for the tool (not used in this experimental implementation)

The tool body and shoulder that were designed and produced for the LCF test are presented in Figure 71.The body is made of H13 steel, and was designed to be compatible with the standard sized tool head on the FSW machine. The shoulder is made of Densimet D176, which is the same material as the existing shoulder of the actual weld tool. A solid plate of copper was added between the tool body and the shoulder to facilitate the rapid removal of the probe and shoulder without the need to drain the cooling fluid every time. Copper was chosen as the separation plate material to allow good heat conduction between the shoulder and cooling fluid now trapped inside the tool body. A centering pin was placed in the copper plate to guide the alignment of the probe and shoulder onto the tool body. A single setscrew holds the probe in the shoulder and a hole on the backside of the shoulder (the same hole used for the centering pin) allows for the rapid installation and removal of probes, even if they are broken.

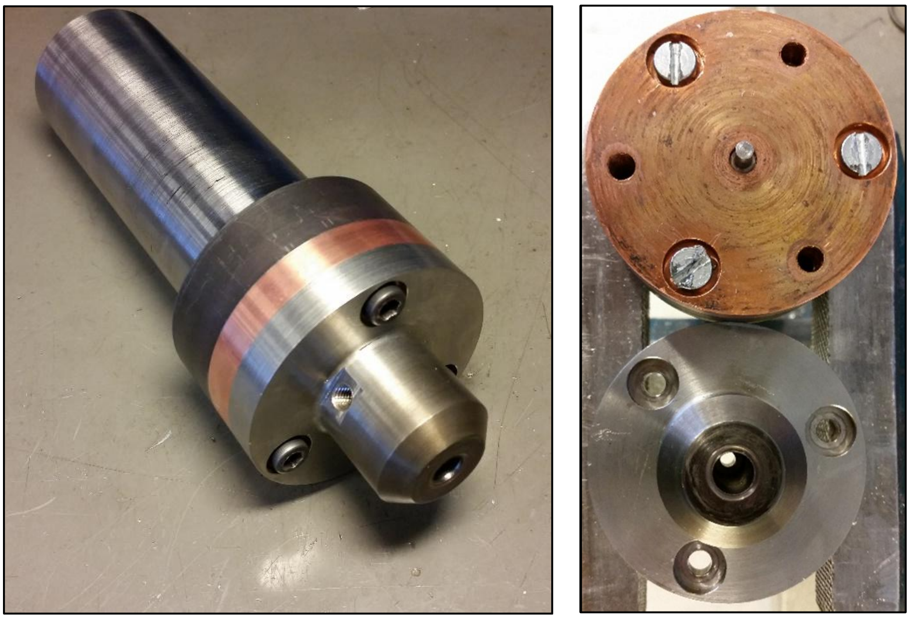

Figure 71: The tool for the experimental LCF test.

The initial probe samples are made from Nimonic 105 and will serve as the baseline for any alternative materials tested. The objective of the Nimonic baseline is to have the probes fracture, or at least show signs of fracture, within 1 meter of weld. The 1-meter weld is a tentative goal and it is acceptable to have the probes survive multiple meters of weld before fracture, assuming it is not prohibitively time consuming to test. Multiple notch depths will be tested to compare how Nimonic 105 performs under different stress levels. The main performance criteria are the ratio of weld length to probe fracture, or probe damage at 1 meter (tentative) if no fracture occurs. Alternative material candidates will be compared to the results obtained for Nimonic 105 to establish which candidates may be better material choices over Nimonic 105.

## 7.2 Experimental Theory & Protocol

The theory behind this LCF test is that the combined loading on the probe during FSW should be higher than the fatigue strength of Nimonic 105 but lower than its ultimate tensile strength. The plan is to have the stress levels increase, by increasing the notch depth, until a majority of probes fracture within 1 m but do not fracture on plunge. The initial weld parameters will be 80 $\frac{\text{mm}}{\text{min}}$ and 800 rpm (about 13 Hz), which equates to 10,000 revolutions per meter of weld. With the bending stress alternating once per revolution and the assumption that the three flats create consistent vibration, roughly 40,000 fatigue “cycles” occur per meter of weld. This is a simplification as the alternating bending and vibrational loading are likely of different magnitudes and not always in phase, but it gives an approximate target length to the LCF.

The theoretical stress in the probe is evaluated using Von Mises failure criteria for combined loading, Figure 72 is a diagram of the theoretical loading on the probe. In this theory, only the bending stress is assumed to alternate as the probe rotates (compressive to tensile loading) while the compressive and torsional stresses are static. These stresses are compared to the datasheet UTS and fatigue strength of Nimonic 105 at the weld temperature(s) [44] to confirm that the stresses are within the correct operating window to facilitate failure. As typical fatigue tests are low load and very high cycle (3x10$^7$ cycles in the datasheet), the stresses in this LCF should be above the fatigue strength but under the UTS. This stress window gives the optimal zone for low cycle fracture of the probes while minimizing the risk that they will immediately fracture during the plunge or start of the weld travel.

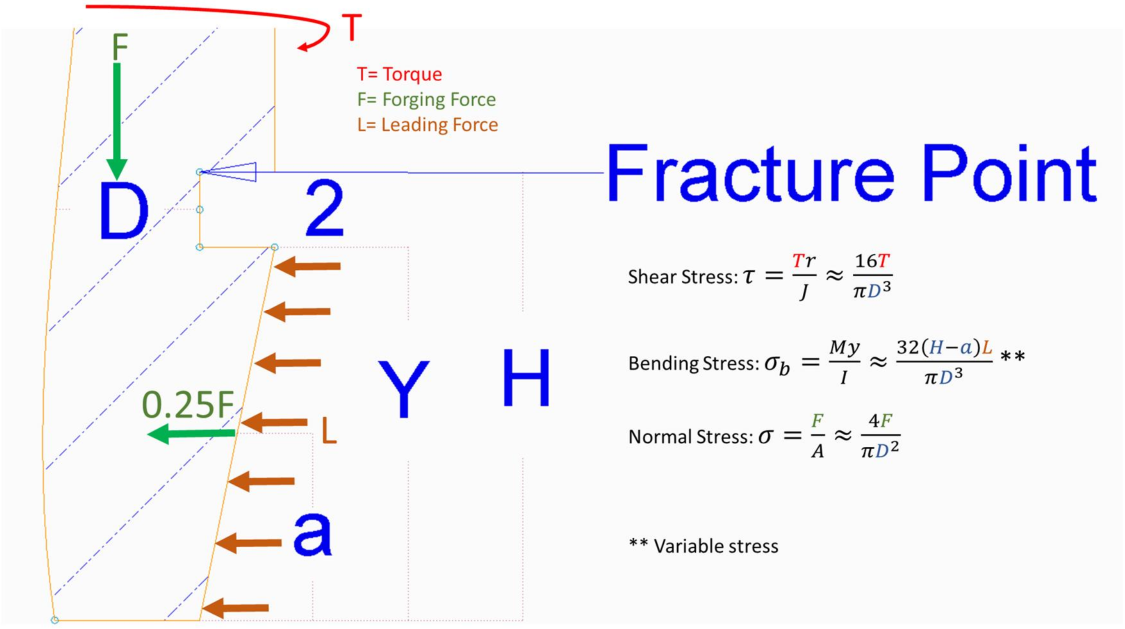
T
T= Torque
F= Forging Force
L= Leading Force
F
D
2
Fracture Point
Shear Stress: $\tau = \frac{Tr}{J} \approx \frac{16T}{\pi D^3}$
Y
H
Bending Stress: $\sigma_b = \frac{My}{I} \approx \frac{32(H-a)L}{\pi D^3}$ **
0.25F
L
Normal Stress: $\sigma = \frac{F}{A} \approx \frac{4F}{\pi D^2}$
a
** Variable stress

Figure 72: Theoretical loads and stresses within sample probes. This diagram assumes the distributed load leading force (L) is equivalent to 0.25 the forging force (F) acting halfway along the length of the probe (point a).

These theoretical loads can be used to predict the total probe stress through the formulation of the equivalent Von Mises stress. By assuming that the bending stress is the only alternating component of the principle stress and that the shear stress is purely caused by the torque, the resulting Von Mises equations become (the terms in these equations are the same used in Figure 72):

$$\sigma_{max} = \sqrt{(\sigma + \sigma_b)^2 + 3\tau^2} \tag{19}$$

$$\sigma_{min} = \sqrt{(\sigma - \sigma_b)^2 + 3\tau^2} \tag{20}$$

These equations can be converted into a more useful form of average and amplitude stress, given the specific loading scenario presented in Figure 72. Using those theoretical loads, the average and amplitude stress equations become:

$$\sigma_{amp} = \frac{\sqrt{(\frac{4F}{\pi D^2} + \frac{8(H-a)F}{\pi D^3})^2 + 3(\frac{16T}{\pi D^3})^2} - \sqrt{(\frac{4F}{\pi D^2} - \frac{8(H-a)F}{\pi D^3})^2 + 3(\frac{16T}{\pi D^3})^2}}{2} \tag{21}$$

$$\sigma_{avg} = \frac{\sqrt{(\frac{4F}{\pi D^2} + \frac{8(H-a)F}{\pi D^3})^2 + 3(\frac{16T}{\pi D^3})^2} + \sqrt{(\frac{4F}{\pi D^2} - \frac{8(H-a)F}{\pi D^3})^2 + 3(\frac{16T}{\pi D^3})^2}}{2} \tag{22}$$

These equations form the basis of the predicted probe stresses. An excel spreadsheet was made that uses the loads registered by the FSW machine and calculates the probe stress based on the probe dimensions and notch diameters. Some of the results from this spreadsheet are discussed later in this chapter.

A complete flowchart of the entire experimental protocol is in Figure 73. The test begins with a no notch specimen plunged and welded up to 1 m. If no fracture occurs, a new specimen with an increased notch increment of D (currently 0.125 mm depth, but this could change) is used, this process repeats until probe fracture occurs. Due to the conical geometry of the probe, the notch increment skips the first millimeter of the probe diameter and starts counting at a nominal notch diameter of 7 mm. Ideally, probe fracture will occur sometime during the length of the weld, if this is the case, then three more trials will be ran using different specimens with the same notch depth. If the result is repeated for all the trials of the same notch depth then a new notch depth increment (D) is added and everything repeats. This will continue until the notch diameter gets so small that the probes begin consistently fracturing during plunge. Enough successful trials should yield a ratio of notch depth, or probe stress, to weld distance for Nimonic 105, which will become the tests baseline.

Some contingency plans are also in place in the event of unexpected fractures occurring during plunge or weld travel start. Depending on which flags are active (which changes based on the current trial) different solutions can be implemented. If fracture occurs on plunge, the first solution is to drill a pilot hole to remove the stress associated with plunging. If fractures still occur then the weld parameters will be changed in an attempt to lower the probe stress. If fracture occurs at the start of travel, the first solution is to shorten the probe length in order to lower bending stress. Similar to plunge fractures, changing the weld parameters is the second solution. Figure 73 shows all the flags and counts for deciding which solution to use. Once a sound baseline has been established for Nimonic 105, the performance of other materials can be tested using this protocol and evaluated as possible material replacements.

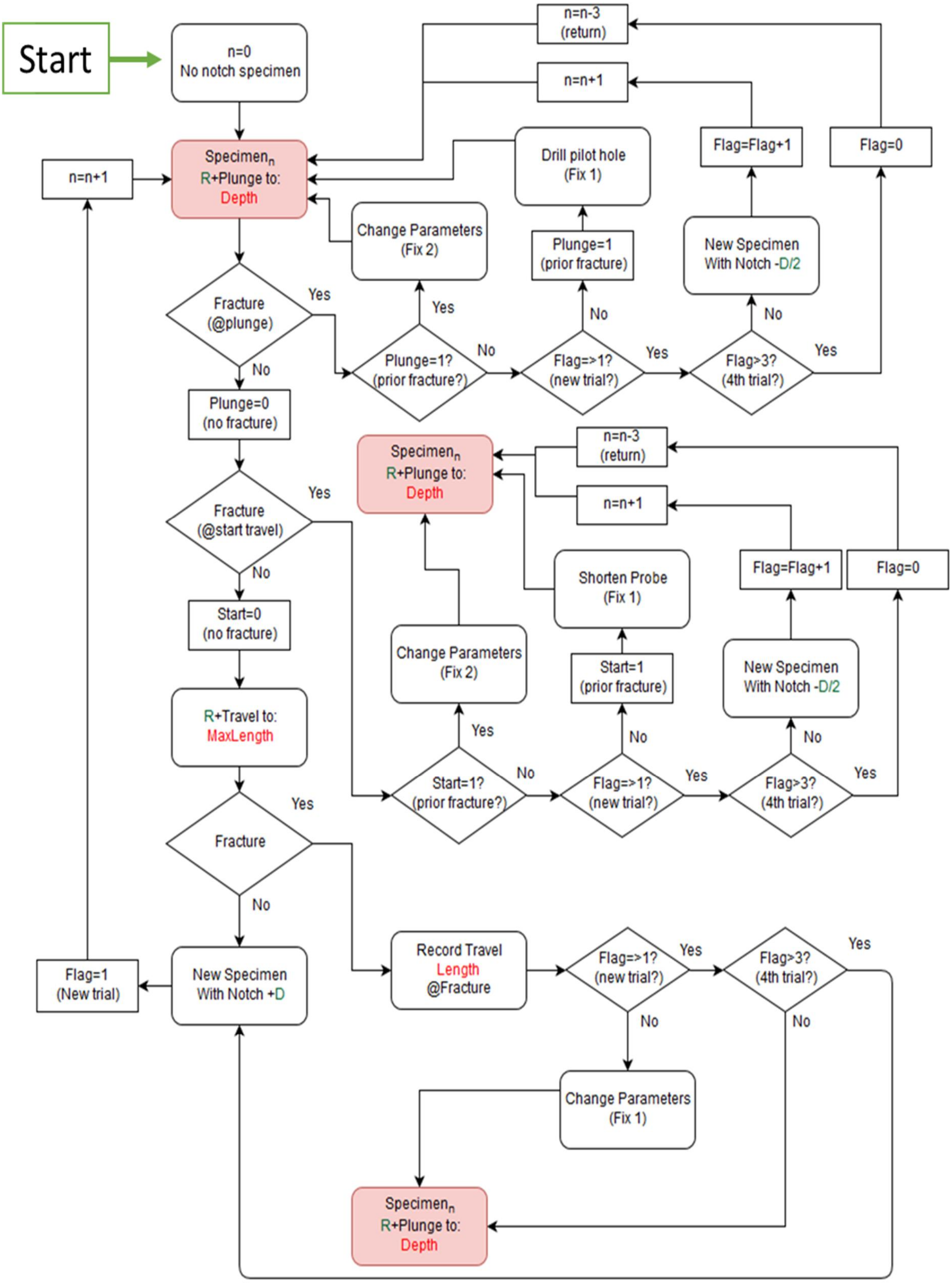
Start
n=0
No notch specimen
n=n-3
(return)
n=n+1
Specimen$_n$
R+Plunge to:
Depth
n=n+1
Drill pilot hole
(Fix 1)
Flag=Flag+1
Flag=0
Change Parameters
(Fix 2)
Plunge=1
(prior fracture)
New Specimen
With Notch -D/2
Fracture
(@plunge)
Yes
Yes
No
No
No
Yes
Yes
Plunge=1?
(prior fracture?)
Flag=>1?
(new trial?)
Flag>3?
(4th trial?)
No
Plunge=0
(no fracture)
Specimen$_n$
R+Plunge to:
Depth
n=n-3
(return)
n=n+1
Fracture
(@start travel)
Yes
No
Shorten Probe
(Fix 1)
Flag=Flag+1
Flag=0
Start=0
(no fracture)
Change Parameters
(Fix 2)
Start=1
(prior fracture)
New Specimen
With Notch -D/2
R+Travel to:
MaxLength
Yes
No
No
Yes
Yes
Start=1?
(prior fracture?)
Flag=>1?
(new trial?)
Flag>3?
(4th trial?)
Yes
Fracture
No
Record Travel
Length
@Fracture
Flag=>1?
(new trial?)
Yes
Flag>3?
(4th trial?)
Yes
No
No
Flag=1
(New trial)
New Specimen
With Notch +D
Change Parameters
(Fix 1)
Specimen$_n$
R+Plunge to:
Depth

Figure 73: Flowchart of the entire LCF test protocol.

### 7.2.1 Preliminary Results

Prior to the completion of the experimental protocol, a small batch of sample probes were tested by Nenonen to verify the test parameters and tools. This section is a brief analysis of those results.

A small batch of sample probes were made with varying notch depth increments (Figure 74), no non-notched specimens were made. These probes were designated A through G based on their notch depth, with A having a 1 mm (8 increments) deep notch and G having a 0.25 mm (2 increments) notch. A select number of these probes were used for welding runs on a copper test plate.

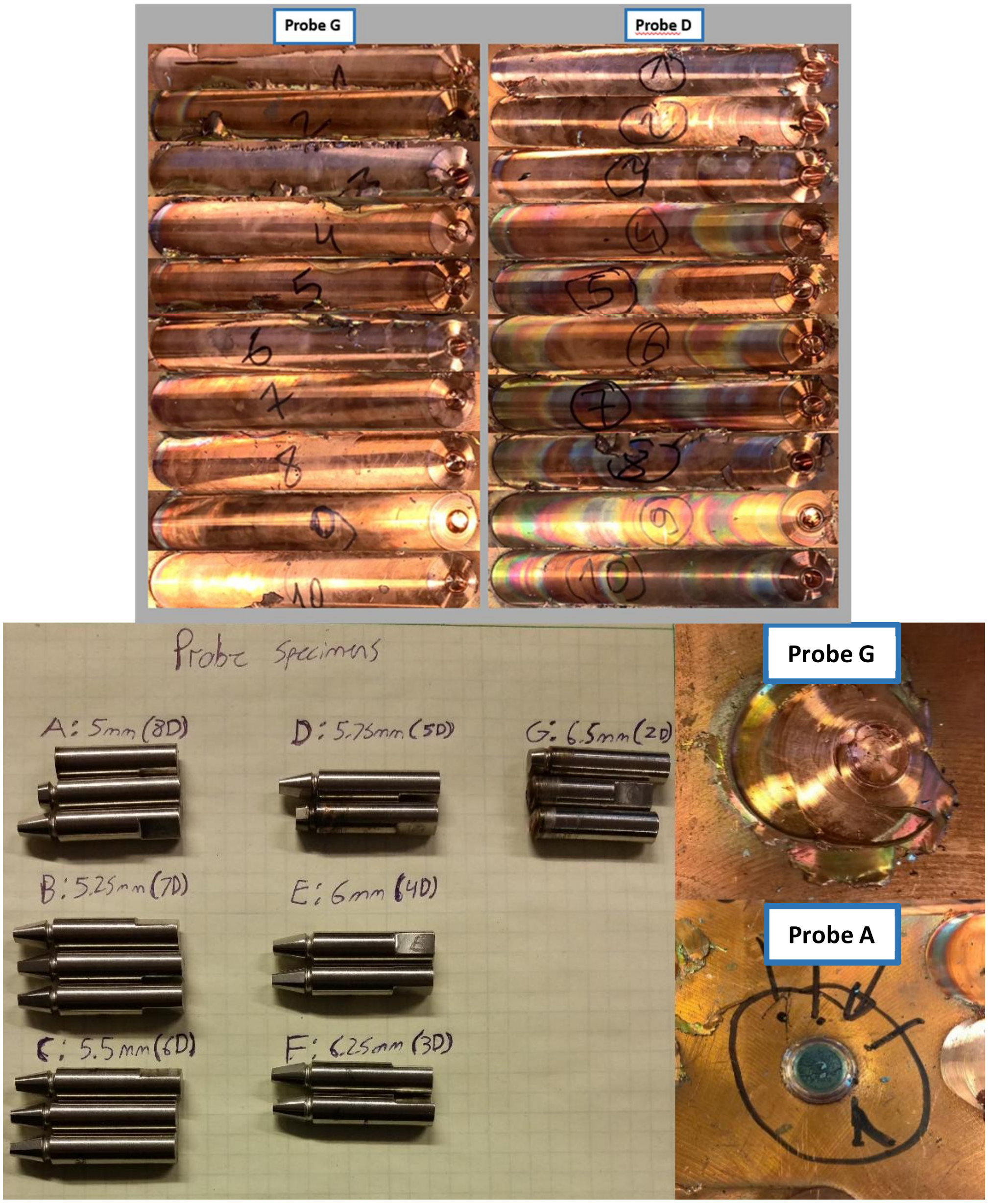

Figure 74: Overview of the preliminary weld results and first test probe samples.

Five probes were tested and two more were modified in preparation for testing. Three G probes, the ones with the smallest notch, were tested first. The first probe was plunged three times without traveling any distance to check that the probes would not immediately break in plunge. After confirmation of probe plunge strength, the probe travel began but it fractured very quickly at the start of the weld. The parameters for this weld were 200 $\frac{\mathrm{mm}}{\mathrm{min}}$ and 800 rpm; travel speed was lowered to 80 $\frac{\mathrm{mm}}{\mathrm{min}}$ for all remaining welds. The next probe G also fractured early in travel, near the start of the weld, poor clamping of the probe was thought to have created more vibration than expected. The last probe G was shortened from 10 mm to 5 mm and survived the entire 1 m of weld with no signs of damage. A probe D, which had a 0.625 mm deep notch (5 increments), was also cut to 5 mm and also survived 1 m of weld. Finally, a probe A, the deepest notch, was tested and it fractured during plunge. Table 9 summarizes these results.

Table 9: Preliminary LCF results summary.

| Probe | Fracture Point | Comments |
|---|---|---|
| G | Start of travel | 3X plunge with 200mm/s and 800 rpm parameters |
| G | Start of travel | Improper clamping suspected to cause early fracture |
| G | No Fracture | Cut to 5mm long, survived 1m of weld with no signs of damage |
| D | No Fracture | Cut to 5mm long survived 1m of weld |
| A | Plunge | Fractured from the top of the notch |

The preliminary tests suggest that the probe length causes a great deal of bending stress, which causes the probes to fracture prematurely. Halving the probe length greatly reduced this stress and allowed both G and D probes to survive the complete 1 m weld. An additional probe A was cut to 5 mm and testing was planned to see if it also survives plunge and welding because of this reduced stress. A second probe D, cut to 7 mm, was to be tested to see if this additional length causes fracture during weld. Once the proper parameters for a good internal probe stress are determined, the additional probes were to be ran according to the protocol.

## 7.3 Parameter Verification Results

After analyzing the preliminary results it was determined that a more precise operating window was required to achieve the proper probe stresses for fatigue fracture. It was found that a 10 mm long probe created too much bending stress during weld travel and caused even the largest notch diameter probes to fail very early on. However, shortening the probes to 5 mm appeared to reduce the bending stress too much, and allowed the probes to survive more weld length than desired. Based on the preliminary results it was assumed that the bending stress was the dominating load during weld travel. This load was greatly influenced by the probe length and the weld travel speed. Finding the correct probe length and weld travel speed to facilitate probe fatigue failures is critical to the application of the LCF test. While the initial travel speed was 80 $\frac{\mathrm{mm}}{\mathrm{min}}$, the ideal nominal travel speed is 160 $\frac{\mathrm{mm}}{\mathrm{min}}$ (when combined with 800 rpm this is double the full-scale weld parameters of 400 rpm and 80 $\frac{\mathrm{mm}}{\mathrm{min}}$). This meant the goal was to find a probe length that resulted in fatigue failures with travel speeds within 160 ± 40 $\frac{\mathrm{mm}}{\mathrm{min}}$.

While optimizing the bending stress was critical, finding the point when the notch diameter was so small that the probes were too weak to function was also important. With no-notched specimens acting as the strongest probes, finding the weakest probes determined when it was no longer useful to test (or manufacture) probes with larger notch depths. Finding this weak point also set the curve for when different notch depths are expected to fail, allowing for the weld parameters to be adjusted so that probes with notch diameters near the weakest probe fail early on, while probes with small notch depths take almost as long as no-notch specimens to fail. The point at which this occurred was assumed to be when the static loading of compression and torsion (forging force and machine torque) caused probe fracture in plunge, before bending stress was introduced. The remaining A-G probe specimens, made by Nenonen, were modified and tested to further characterize the LCF operating window and to give information that influenced the next revision of the test probe samples.

To confirm that 10 mm probes were too long, two of the next strongest probes (as there were no more 10 mm G probes left) probe F were tested. As expected, both of these probes successfully completed plunges, but failed almost immediately at the start of travel. Next, the two surviving G and D probes (from the preliminary testing) were tested with increasing travel speeds to gauge how much stress it would take to cause shortened 5mm probes to fail. The probe D failed at 400 $\frac{\mathrm{mm}}{\mathrm{min}}$ while the probe G lasted until 1,000 $\frac{\mathrm{mm}}{\mathrm{min}}$. This showed that bending stress was greatly reduced in 5 mm long probes. However, these results are abnormally high when compared to the failure points of the rest of the probes. Perhaps a strain hardening or a heat treating effect occurred by welding 1 meter with the probes at a lower stress level of 80 $\frac{\mathrm{mm}}{\mathrm{min}}$ that improved the fracture strength of the probes.

After the 5 mm probes D and G had failed, the 5 mm probe A and 7 mm probe D, which were created during the preliminary results trials but never used, were tested. Both probes fractured in plunge. This showed that the large notch of probe A created much too weak of a probe, even with reduced length, while the notch depth of probe D was on the border of being too weak. Next, a 5 mm long probe C was tested, and as expected, fractured during plunge. This confirmed that a probe D notch diameter of 5.75 mm was the smallest diameter probe that could survive plunge. Anything smaller than a probe D, and even some longer probe D's (5 mm survived 7 mm did not), would likely fail in plunge due to the combined static torsional and compressive loading alone.

The fractures due to static loading fit well with the data predicted from the static loading portion of the test theory. Table 10 shows the predicted value of probe stress in the notch compared to the best-case UTS for Nimonic 105. These predictions were calculated assuming the bending stress was zero during plunge, leaving only the compressive and shear stresses in the Von Mises equations. The loads used in the calculations were the average torque and compressive force registered by the FSW machine during plunge, which was 22-25 N*m and 10-12 kN. From the table it is easy to see how the stress in probe D is nearly over the UTS of the Nimonic 105. Anything weaker will fracture due to overload during plunge; this prediction is consistent with the test results.

Table 10: Predicted static probe stress for all notch depths. 23.5 N*m and 11 kN loads were used, which were the average during plunge. These stresses assume the alternating bending stress is zero during the plunge, leaving only static compression and torsion.

| Nimonic UTS | Probe A | Probe B | Probe C | Probe D | Probe E | Probe F | Probe G |
|---|---|---|---|---|---|---|---|
| 1200 MPa | 1750 | 1520 | 1329 | 1170 | 1036 | 922 | 824 |

These results essentially shifted the curve for when failures were expected with different notch depths. Originally, the 5 mm notch diameters of probe A (1 mm notch depth) were expected to fail early in travel, with the 5.75 mm probe D (0.625 mm notch depth) failing somewhere in the middle of the sample pool. However, after finding that every probe with a notch diameter smaller than 5.75 mm failed in plunge, probe D became the new "weakest" probe. This meant that there were seven progressively smaller notch diameters between a no-notched probe and a 5.75 mm (probe D) notch diameter available for testing, given a notch increment of 0.125 mm. As previously mentioned, the notch diameters begin counting at 7 mm, while the no-notched specimens have a nominal diameter of 8 mm.

Once alternating bending stress is introduced, accurate predictions from the test theory become increasingly difficult to achieve. The issue arises in determining how much of the loads registered by the FSW machine are on the probe alone. The test theory predicts probe stresses based on probe loads, but the loads the FSW machine measures are a combination of probe, shoulder, and dry run (the energy required to solely move the machine) loads. Factoring out the dry run loads is easy, the machine can simply be run without actually welding anything, but finding the ratio of loads shared between the probe and shoulder is difficult. For the initial predictions, the stress state was based purely on the ratio of area between the probe and shoulder. This is a very rudimentary method of approximating the load sharing and is likely not accurate, but it gives some basic insights into what is occurring inside the probe. Figure 75 is a graph of this basic predicted stress state for a probe G.

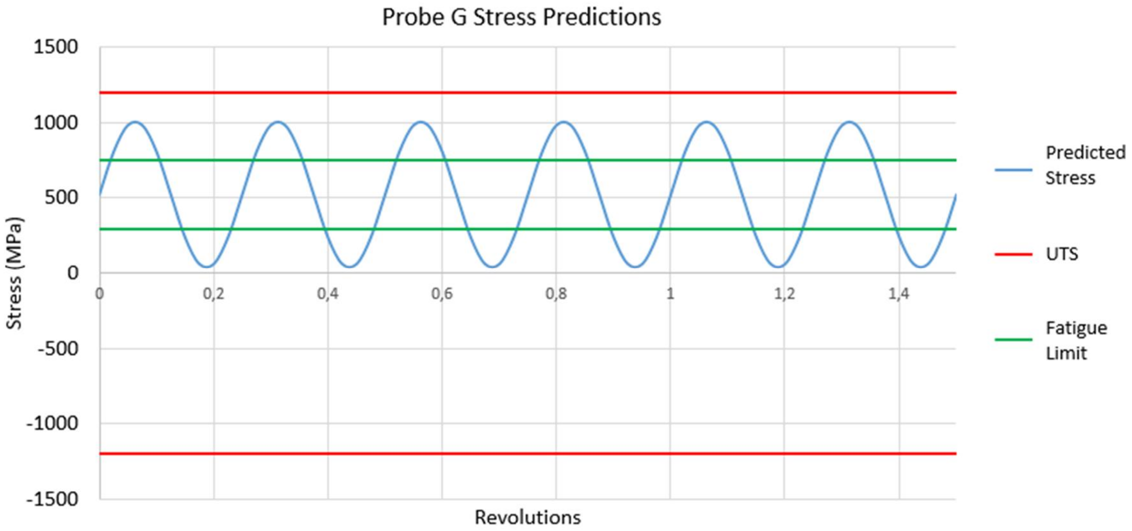

Figure 75: Probe G stress predictions based on the test theory with load sharing based on area.

This graph shows that the predicted stress for a probe G is above the fatigue limit but under the UTS, which is desired. For this probe G, the predicted Von Mises stress is 521.2 ± 480.7 MPa, which is 521 MPa of static stress and 481 MPa of alternating stress. There are many assumptions in this prediction, one of the largest is the graph assumes that there are four equal cycles in stress per revolution (1 from bending and 3 from impact), which is likely not true. Overall, the usefulness of these predictions is questionable, due to their poor accuracy. However, they serve as the starting point for the logic behind the testing.

With this information, the remaining D, E, and F probes were tested in an attempt to identify the correct probe length for achieving the optimal failure window given the operating conditions of 800 rpm and 160 $\frac{\mathrm{mm}}{\mathrm{min}}$. The goal was to have probe D, the new weakest probe, fail early in travel but not fail instantly at the start of travel. The rest of the probes (E and F) should have progressively more weld length for fracture, but ideally would not take multiple meters of weld to fail. A probe E (6 mm notch diameter) was cut to 7 mm long and fractured very near the start of travel, at only 17 mm of weld. It is likely this probe failed during the start of travel and the machine continued welding for a short time with a broken probe. Another probe E was cut to 6 mm long and was started at a reduced speed of 80 $\frac{\mathrm{mm}}{\mathrm{min}}$. After 200 mm of weld at 80 $\frac{\mathrm{mm}}{\mathrm{min}}$ the weld speed was increased to 160 $\frac{\mathrm{mm}}{\mathrm{min}}$ and the probe fractured after 25 mm. This probe E survived 225 mm in total before fracture, but only 25 mm at the desired weld speed. The final probe D was cut to 5 mm long and fractured after 23 mm of travel (at 160 $\frac{\mathrm{mm}}{\mathrm{min}}$). This was the desired outcome for the probe D, as the probe clearly survived travel-start but fractured very early into travel. Figure 76 shows how the 5 mm probe D clearly fractured during travel; the bright blue spot in the weld path is the probe fracture point.

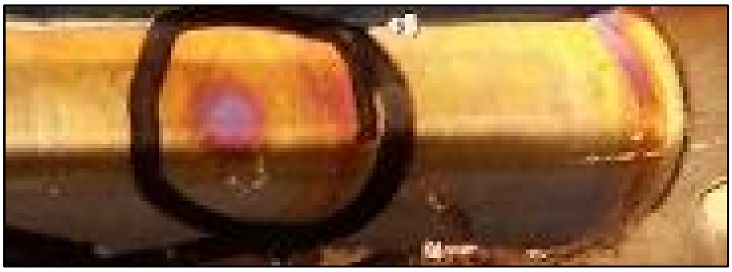

Figure 76: 5 mm probe D fracture after 23 mm of weld; the blue spot is the probe fracture point.

Once the 5 mm probe D had failed, the last probe E was cut to 5 mm long and was tested. The test began at a 120 $\frac{\mathrm{mm}}{\mathrm{min}}$ travel speed as the 6 mm long probe E (from earlier testing) failed too quickly at a travel speed of 160 $\frac{\mathrm{mm}}{\mathrm{min}}$. This probe was ran for 1,190 mm without failure and no visible signs of damage. After this first meter of weld, the weld travel speed was increased by 20 $\frac{\mathrm{mm}}{\mathrm{min}}$ every 500-600 mm of additional weld; 575 mm at 140 $\frac{\mathrm{mm}}{\mathrm{min}}$, 600 mm at 160 $\frac{\mathrm{mm}}{\mathrm{min}}$, and 500 mm at 180 $\frac{\mathrm{mm}}{\mathrm{min}}$. The probe failed after 70 mm at a weld speed of 200 $\frac{\mathrm{mm}}{\mathrm{min}}$, and a total weld length of 2,935 mm. This result showed that the ideal length for the test probes was between 5-6 mm.

The final probe tested of this sample batch was the last probe F. This probe was cut to 5.5 mm long, in the middle of the ideal 5-6 mm length. This probe was ran for 1,275 mm at 160 $\frac{\mathrm{mm}}{\mathrm{min}}$ (the desired travel speed) without fracture or signs of damage. After this first meter (a little over a meter) of weld the probe was ran for two 350 mm welds (700 mm total) at 180 $\frac{\mathrm{mm}}{\mathrm{min}}$ and 200 $\frac{\mathrm{mm}}{\mathrm{min}}$ each, 1,400 mm total (Figure 77). This probe began to fail at the very end of the last weld at 200 $\frac{\mathrm{mm}}{\mathrm{min}}$ and fractured completely during the probe withdrawal from the copper. It is believed that the loading change at the end of the weld, from compressive to tensile, caused the already fatigue damaged probe to fail. In total, this probe survived 2,675 mm of weld before fracture.

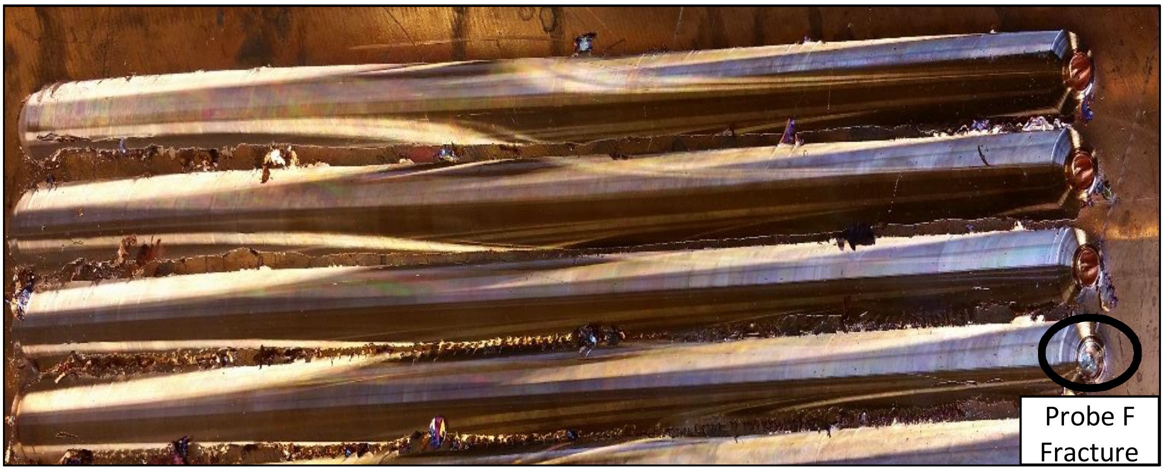

Figure 77: The last 1,400 mm (4 X 350 mm) weld of the 5.5 mm long probe F that survived 2,675 mm of weld, the bottom right shows where the probe fractured.

These results show that the ideal length of probes for LCF fracture with weld parameters of 800 rpm and 160 $\frac{\mathrm{mm}}{\mathrm{min}}$ is between 5-6 mm. It also showed that the smallest notch diameter (weakest probe) the did not cause immediate fracture was 5.75 mm (probe D). The results of all the probes tested are summarized in Table 11 (including the 5 from the preliminary results). They show that LCF failure can be expected in roughly 3 meters of weld, which is approximately 60,000 fatigue "cycles" at the desired weld parameters. However, further testing is needed to establish a more statistically sound baseline for alternative material comparison.

Table 11: Summary of the LCF probe test results.

| Probe | Length (mm) | Notch Ø (mm) | Fracture Point | Weld Length (mm) |
|---|---|---|---|---|
| A | 5 | 5.00 | Plunge | 0,00 |
| A | 10 | 5.00 | Plunge | 0,00 |
| C | 5 | 5.5 | Plunge | 0,00 |
| D | 7 | 5.75 | Plunge | 0,00 |
| F | 10 | 6.25 | Travel Start | 0,00 |
| F | 10 | 6.25 | Travel Start | 0,00 |
| G | 10 | 6.50 | Travel Start | 0,00 |
| G | 10 | 6.50 | Travel Start | 0,00 |
| E | 7 | 6.00 | Weld/T.S. | 17 |
| D | 5 | 5.75 | Weld | 23 |
| E | 6 | 6.00 | Weld | 225 |
| G | 5 | 6.50 | Weld | 1168,00 |
| D | 5 | 5.75 | Weld | 1234,00 |
| F | 5.5 | 6.25 | Weld | 2675,00 |
| E | 5 | 6.00 | Weld | 2935,00 |

### 7.3.1 Revision 2 Probes

In total, 15 probes from the A-G sample pool were tested (including the 5 tested in the preliminary results) and analyzed. Based on the results from those probes a second revision of 21 new probes were manufactured for further testing, seven batches of three identical probes each. Based on the previous results, the smallest notch diameter made in this revision was 5.75 mm (probe D). This was expected to be the new "weakest" probe that should fail early during weld. From there, the notch diameter was increased by 0.25 mm (one 0.125 mm increment) for every new batch of three. In all, three probes of notch diameters 5.75, 6.00, 6.25, 6.50, 6.75, and 7.00 mm (18 probes total) were made. Three unnotched probes were also made for establishing a strongest probe reference.

The length of all revision 2 probes was 6 mm, which was the upper end of the ideal probe length found in the results. They were manufactured at the upper end of the ideal range because 3 meters of weld before failure, as was found with 5 mm and 5.5 mm long probes, is acceptable but time consuming. A slightly longer probe was expected to reduce the weld length and time needed to achieve fracture. Additionally, the probes could always be shortened later if it was determined that the probes were too long.

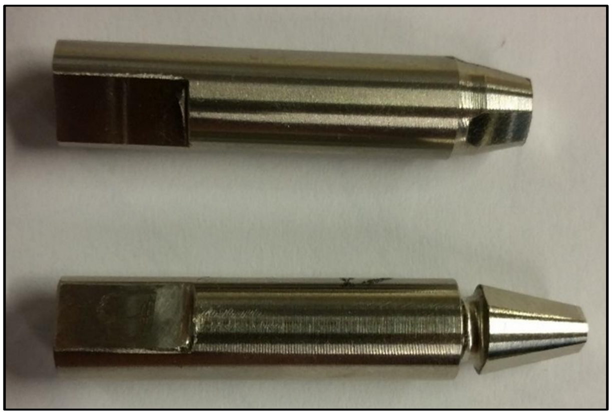

Figure 78: Revision 2 probe (top) compared to a 10 mm long original LCF test probe (bottom).

The manufacturing and testing of these probes is ongoing and will not be included in this thesis. The intended use for these probes will be as the first wave of Nimonic 105 probes solely designed for establishing a weld length (fatigue cycles) to notch diameter (probe stress) baseline.

### 7.3.2 Probe Twisting

During the testing, it was noticed that the probes have a tendency to twist during welding. A majority of the twisting occurred in the probe tip, after the notch, but there was also a small amount of twisting in the probe body. The twisting in the probe tip was the most critical, and of much greater magnitude compared to the twisting of the probe body, so it was the primary focus of investigation. The way probe twisting was measured was based off the relative location of the flats cut into the probe tips. A reference line was kept constant with respect to each probe and the angle each flat made with that reference line was measured. All three flats were measured as a redundancy to eliminate errors. Figure 79 is a representative image of how the probe torsion measurements were done.

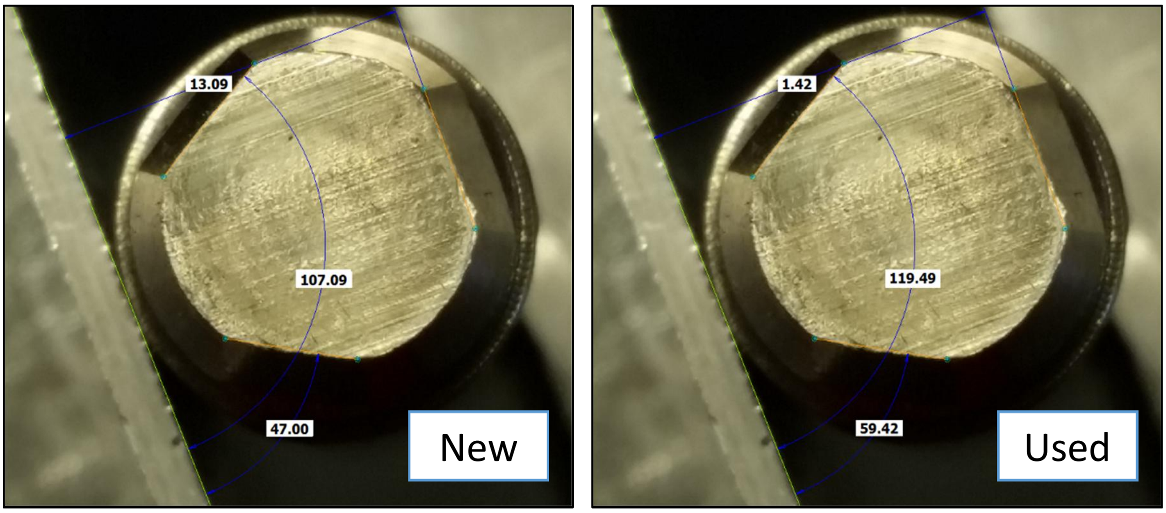

Figure 79: Representative probe torsion measurements based off the relative probe flat locations. This image is not an actual measurement but is intended to show how the change in relative flat angle was measured.

The purpose of these measurements is to compare the relative positons of the flats pre-weld to their positons after increasing weld distances. Three images of the probe, from different orientations, gives an average value for each flat angle, further reducing error. Prior to welding the position of each flat is measured on the unused probe; as the global flat position is arbitrary between probes this sets the zero for that specific probe. This zero is subtracted from the flat positions after welding; giving a relative change in flat angle that is consistent for all three flats. These three relative angle measurements are further averaged to give one approximate change in angle, which is the final probe twist. This means that nine measurements are taken (three images, with three flats each) to get one average probe twist measurement, allowing for a relative accuracy of ±2° of error.

Analysis showed that the probes exhibit a majority of twist very early during weld, but not during plunge. All probes measured only showed between 0-2° of twist during plunge (as signified by a vertical jump along the Y-axis in Figure 80), which is within the error margin. Once the probes reached a certain amount of twist, which appeared to depend on the notch diameter, they did not twist any further unless the stress level was increased. Figure 80 graphs the measured average probe twist versus the weld length. The dots are points where the twist was measured and the color of the dashed lines indicate the weld travel speed between sample points. As seen from the graph, almost all twisting occurs before 250 mm of weld and then stabilizes unless the weld travel speed is increased (more bending stress). Both probes E and F show a jump in the probe twist when the travel speed is increased. This stabilizing of the probe twist could be a strain hardening effect that improves the fracture resistance of the probes until the stress level increases. Of the probes measured, they all fracture once 12-14° degrees of twist have been reached. With such a small sample size, this could simply be a coincidence, but it warrants further investigation as it could be used as a warning sign of eminent fracture.

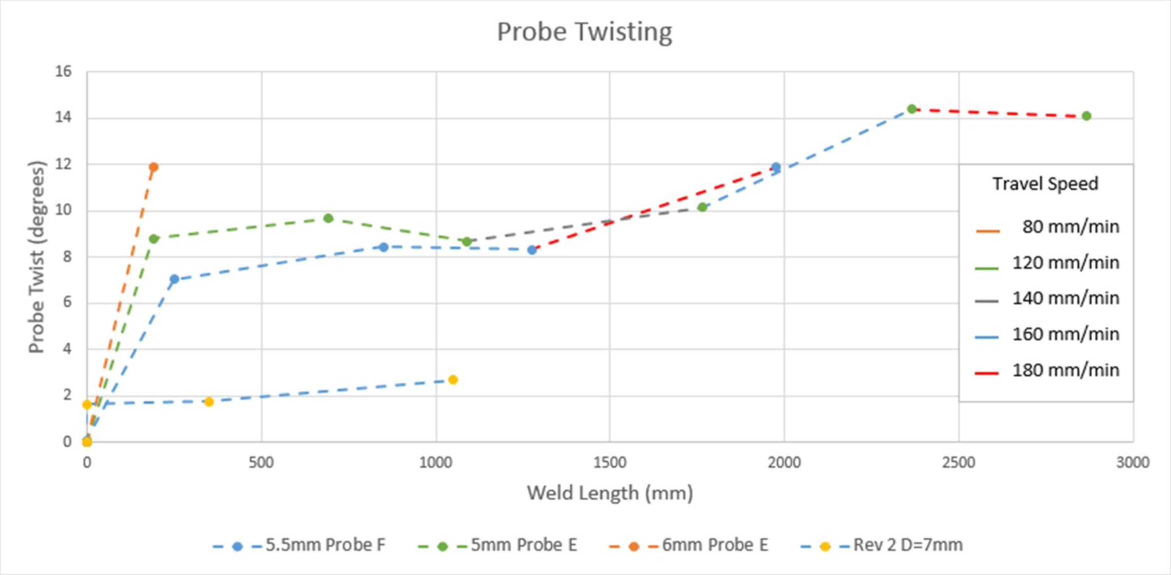

Figure 80: Plot of probe twisting; different colored lines indicate changes in weld travel speeds, dots are sample points of different probes.

With a relatively small sample size, more investigation into the probe twisting in needed. The revision 2 probes will all be measured for twist during their use to compare how the notch depth effects the torsion magnitude. Additionally, the amount of twisting occurring in the probe body compared to the probe tip needs to be quantified.

## 7.4 Microscopic Analysis

Apart from measuring the weld length until failure of the probes, some microscopic analysis of different probe samples was done. Both optical microscope (OM) and scanning electron microscope (SEM) analysis was done. Multiple samples of different probe failure mechanisms were created for examination; Figure 81 shows some of the samples. The goal of this analysis was to investigate if there was any difference in the probe material based on the failure mode. Probes that failed in plunge, travel start, and after long welds (fatigue loading) were all compared to each other and to an unused reference material. This analysis focused on any microstructural changes of the probe material and also on the probe fracture surfaces themselves. However, it was suspected that the fracture surfaces of the probes would be too damaged by the post fracture grinding of the two probe halves. Additionally, only the fracture surfaces of probes that failed in plunge could be analyzed, as the all the other probes were covered in copper post fracture.

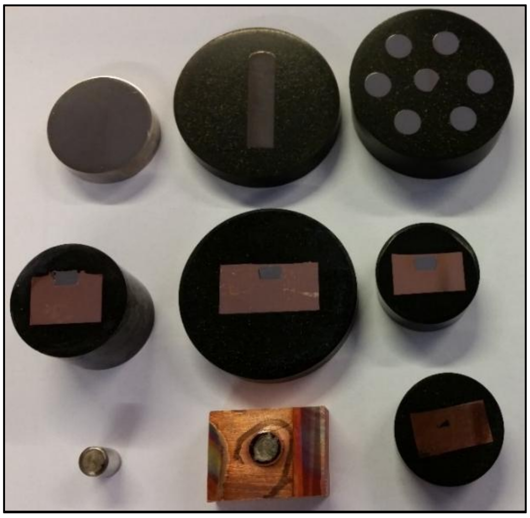

Figure 81: Representative SEM and OM specimens of fractured probes and of reference material.

Figure 82 is a cross-sectional SEM image of a fractured probe E, which fractured after 2,935 mm of weld (middle row, rightmost sample in Figure 81). This was the most heavily fatigued probe analyzed and, as expected, fractured across the minimum notch diameter. The purpose of the sample was to investigate what kind of damage was present, and if there were any differences in the microstructural damage between this probe and a probe that failed in plunge (Figure 83). As seen from Figure 82, there is 300-500 µm deformation zone radiating down from the fracture surface. In this region, the grain structure of the probe material is heavily distorted; the distorted zone is larger near the probe edges, and is minimal near the central axis. This is expected as the peak stress regions are along the outer probe edges while the bending stress should theoretically be zero along the central axis.

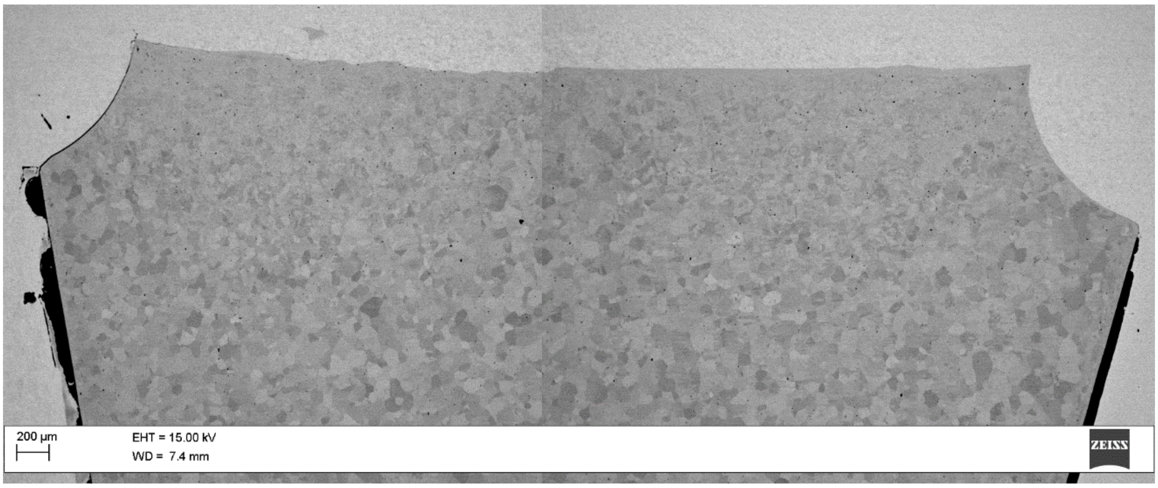

Figure 82: Cross-sectional SEM image of probe E that fractured after 2,935 mm of weld.

By analyzing a probe A that failed in plunge (Figure 83) it can be seen that this probe also has a 300-500 µm deformation zone under the fracture surface. Similar to probe E, it is maximum near the probe edges and minimal along the central axis. This probe also shows a very heavily recrystallized zone at the probe fracture surface. This is post fracture damage caused by the two halves of the probe pushing and grinding together as the FSW machine slows down. Upon fracture the FSW machine does not stop instantly, this residual motion has enough friction and pressure to deform and completely recrystallize the fracture surface (this is the damage mentioned earlier that destroys the fracture surface).

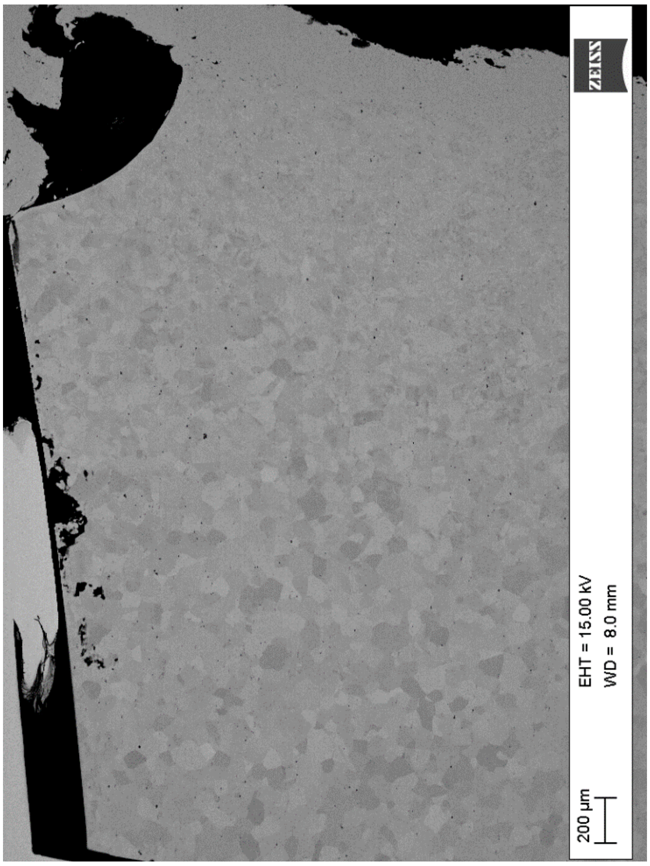

Figure 83: Cross-sectional SEM image of probe A that fractured during plunge. The black marks along the probe edge are residual sample resin, not probe damage.

Figure 84 compares the non-distorted grain structure of probe E to an OM image of an unused reference sample of Nimonic 105. The image for probe E was taken in the center of the probe, where there was no visible deformation. Visually, there is no difference in the grain structure between probe E and the reference material (probe A was also compared and showed similar results). The grain structure was the same between both samples in terms of size and shape with grain sizes of roughly 80 µm. This was consistent with Westman's findings of 50-150 µm [15] and Nenonen's observations of 67-90 µm [6]. There are precipitates present in both samples, as expected, but analysis was not done to confirm their chemical composition. There was no obvious difference in the precipitates between samples, but further analysis could be done to quantify the actual precipitate density and to investigate if there is any particle migration.

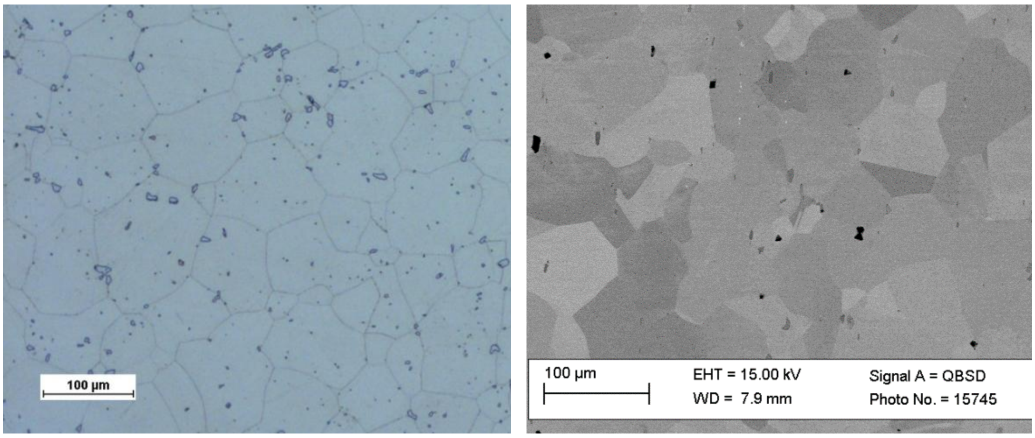

Figure 84: OM image of reference Nimonic 105 grain structure compared so SEM image of probe E (2,935 mm of weld).

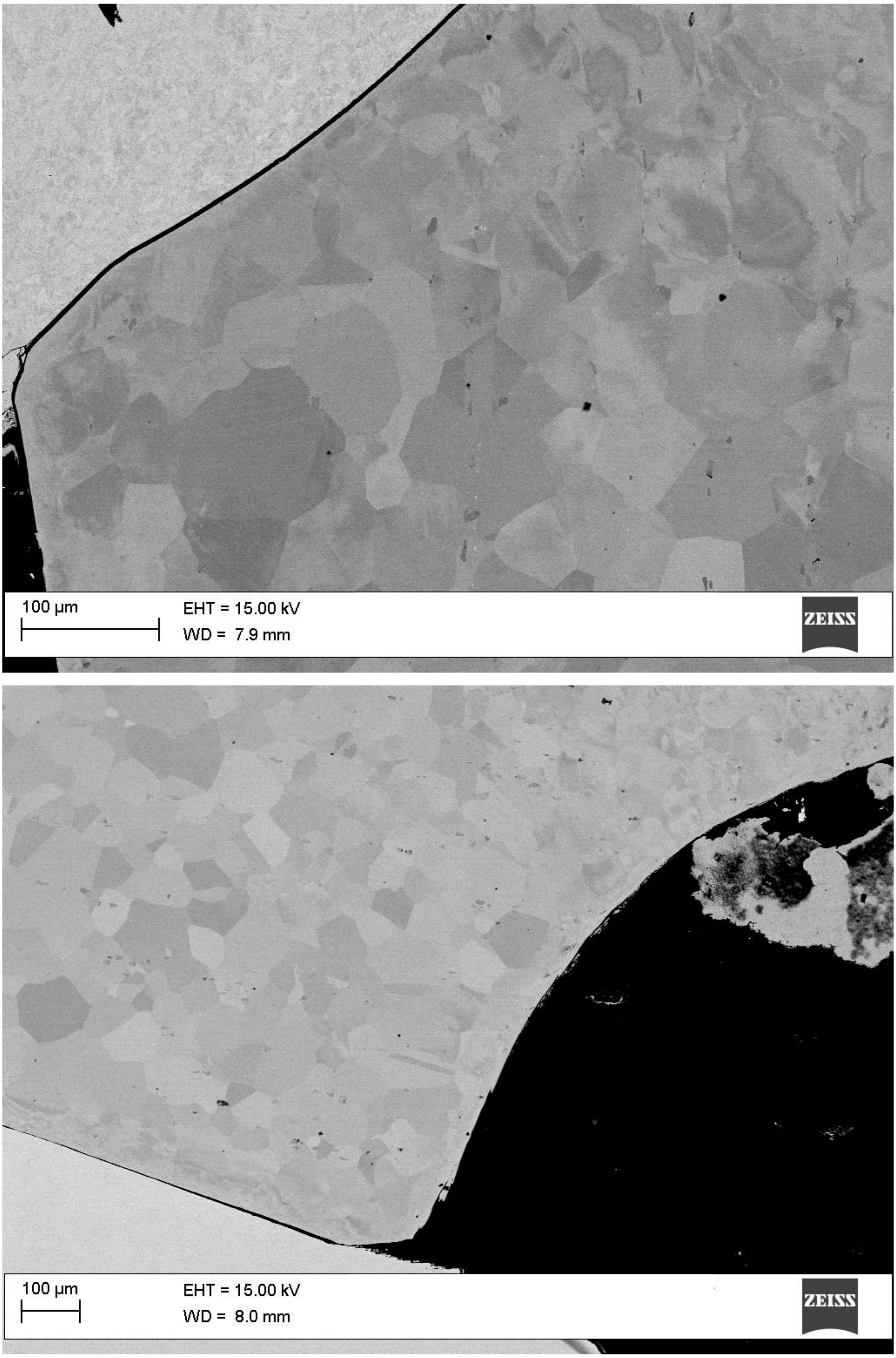
100 µm
EHT = 15.00 kV
WD = 7.9 mm
ZEISS
100 µm
EHT = 15.00 kV
WD = 8.0 mm
ZEISS

Figure 85: Close up of the deformation zones along the fracture surfaces and probe edge compared to undistorted grain structure. Probe E (2,935 mm of weld) on top and probe A (plunge) on bottom.

Figure 85 shows close up images of the transition between the distorted grains of the fracture zone and probe edge to an undamaged grain structure. Interestingly, there was not a noticeable deformation zone along the bottom surface of the probes, even though this region was expected to undergo very high stress during plunge. The deformation zone along the probe edges is consistent between probes and is approximately 30 µm wide. A deformation zone was also found on full-scale probes by Westman [15] and Nenonen [6], but they only observed a zone of 10 µm wide. The increased size of this deformation zone is likely because the full-scale probes are hardened before use while the test probes are not.

Overall, no major differences were found when comparing the fractured sample of a heavily fatigued probe E and a plunge-fractured probe A. The deformation zone around the fracture zone was of similar size in both probes, meaning it was likely caused by the final overload fracture and not fatigue damage. The small deformation zone on the outer edges of the probe was also present in both samples, meaning this was also formed very early on and is not fatigue damage. The grain structure of the fatigued probe also matches very well to the structure of the reference Nimonic. The results show that deformation is clearly present in the probes, but it is difficult to say if there is any fatigue damage. Just because no signs of fatigue were found on these samples does not mean it can be ruled out. Many of the surfaces likely to show fatigue damage are covered by copper, or are damaged post fracture. Further analysis is needed, perhaps with new approaches on removing the copper covering the fracture surfaces of the probes, or by specifically creating samples looking for crack growth in fatigued probes prior to probe fracture.

Analysis using an OM of the remaining section of a fractured probe (the part left in the tool) showed a similar deformation zone to the SEM images. However, this deformation zone is much more heavily damaged than the probe buried in the copper as this part continued to spin after fracture. Figure 86 shows the full cross-section fracture profile of a probe G that welded 1,168 mm before fracture. The shape of the fracture suggests the material fails with ductile torsion, twisting in the plane of maximum shear loading. The domed structure of the fracture could hint at some brittle tendencies, but it is more likely that this shape was formed from the post fracture grinding. It was noticed that the Nimonic seems to “peel” away in layers during fracture. On the right edge of the image, there is a large tear of Nimonic that was in the process of peeling away when the weld was stopped.

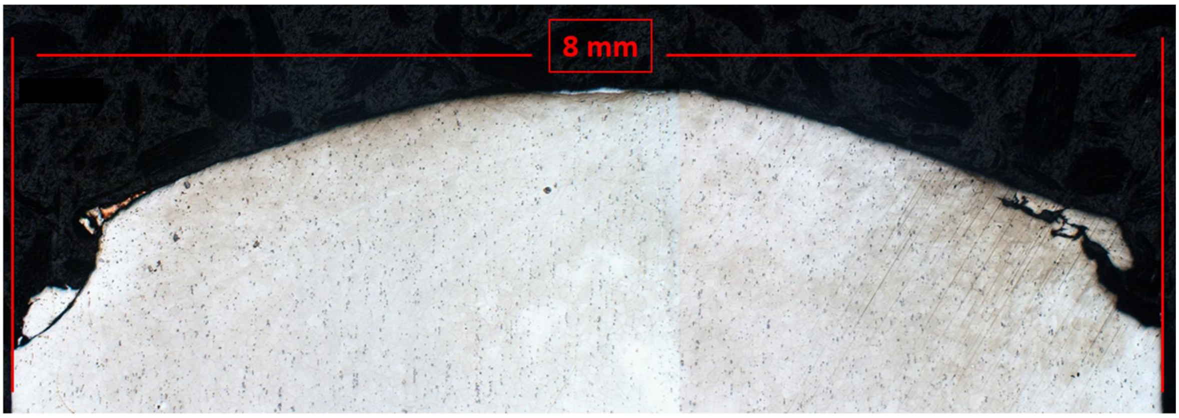

Figure 86: Cross-sectional OM image of fractured probe G (1,168 mm of weld).

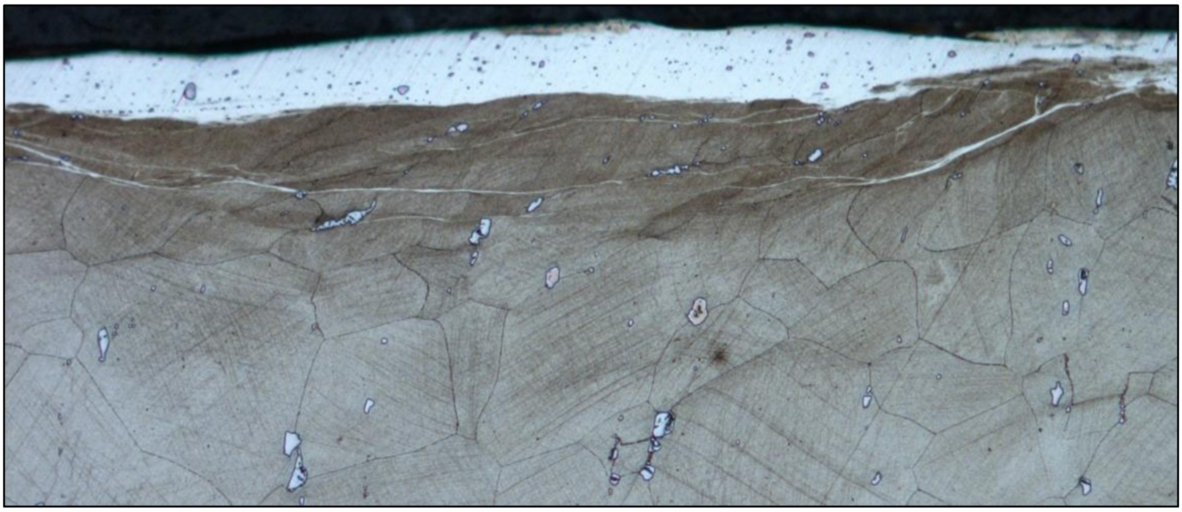

Figure 87: OM image of probe G Nimonic-copper interface, with copper filling the cracks/folds in the fractured Nimonic 105. Estimated size of the damaged region is 100 µm.

Figure 87 is a magnified image of the Nimonic-copper interface, in this image the highly deformed zone can be seen. While interesting, a majority of this damage was likely post fracture, as evidenced by the uniform grain twisting. This evidence is indicative of ductile hot shear failure, which is the expected failure mode. In this region, copper fills the cracks and folds left behind by the tearing Nimonic. As the probe slows its rotation post fracture, the copper becomes trapped in the gaps and seams between the Nimonic.

SEM analysis of the probe fracture surfaces confirmed that a large amount of post fracture grinding removed/destroyed a majority of the original fracture surface. Figure 88 shows the least damaged fracture surface of the tested probes, a probe C that failed in plunge. The figure also shows what a typical fracture surface looks like after failure (top left) and demonstrates why analysis of the fracture surface is so challenging.

As seen in the figure, even the least damaged probes have most of their fracture surface destroyed post fracture. The tears and folds of the Nimonic are easy to see, and if this probe had completed plunge would likely have trapped copper (as in Figure 87). The magnified image of the fracture surface shows clear ductile shear in a radial pattern. This surface gets very hot after fracture, so hot that the Nimonic will glow for a short time, and this causes very ductile shear. This high temperature also contributes to the grain recrystallization seen back in Figure 83. Precipitates on the fracture surface are dislodged and form radial grooves in the surface. These precipitates, combined with the materials ductile tearing form a sweeping circular pattern that indicates hot shear failure but obscures evidence of other possibly contributing failure modes.

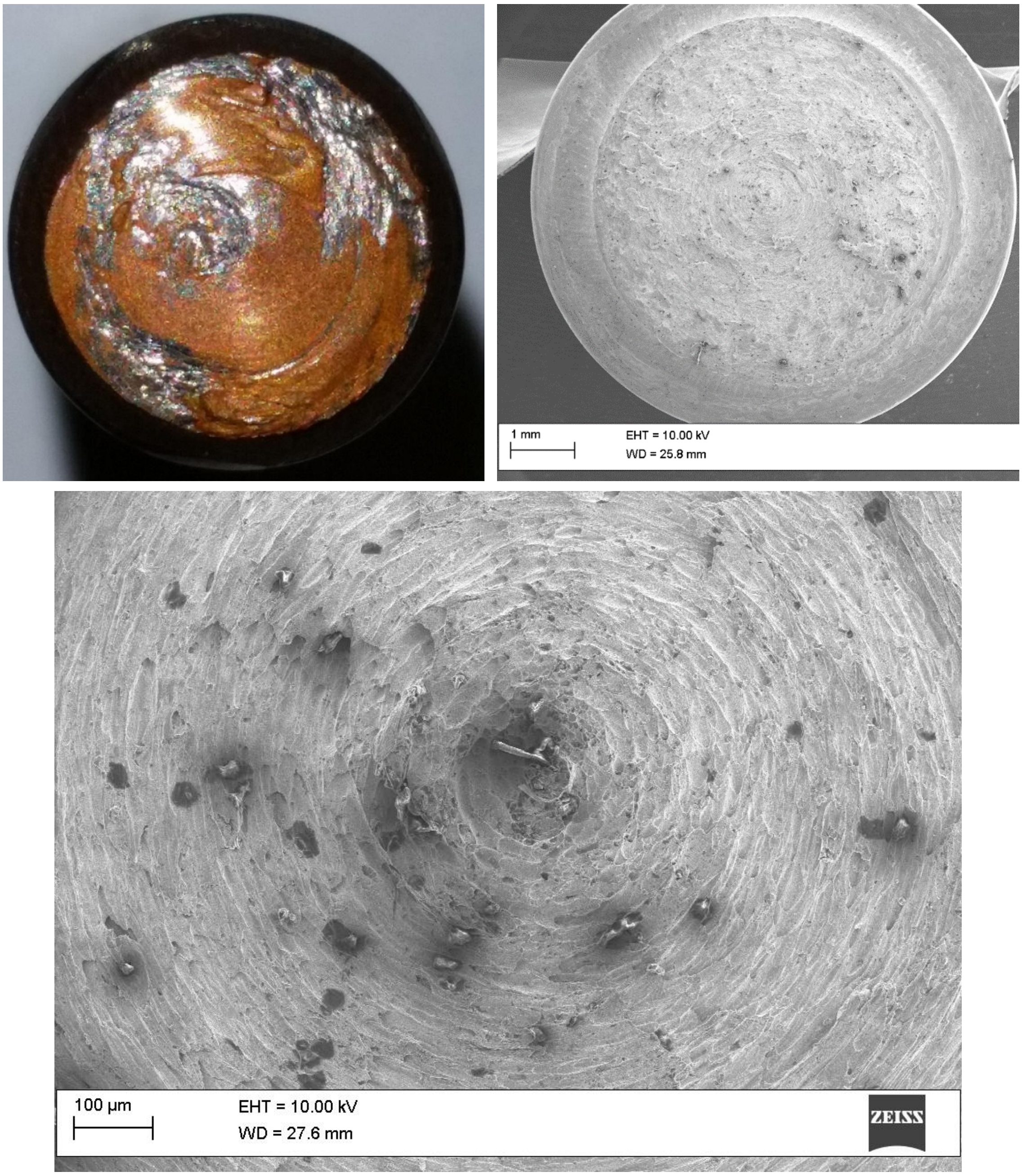

Figure 88: Probe fracture surfaces. Top left is of a heavily damaged, copper covered surface, top right is of probe C that fractured in plunge, bottom is a more magnified image of probe C.

While interesting to look at, the post fracture damage to the probes is a major obstacle in accurate microscopic analysis. More work is needed on developing methods for preserving the fracture surface and for removing the residual copper. The results in this thesis should not but treated as complete conclusions, but as preliminary finding for determining what can be expected during further LCF testing. These initial results from the LCF testing show promise, but more data is needed for a completely thorough analysis.

# 8 Summary

## 8.1 General Comments

Friction Stir Welding (FSW) of thick copper, specifically for the sealing of nuclear waste canisters, is a challenging and complex task. Many hours of work and years of development have gone into creating a stable weld process. However, there are areas of possible improvement in both the probe geometry and material, which could lead to an even higher level of reliability and weld quality. Originally, many of these improvements would require a large amount of experimental validation. With probes as large and complex as the ones used in this work experimentation is a costly and time-consuming process, which is why the original development was discontinued.

The numerical model created in this work was designed specifically to reduce the need for full-scale experimentation of every probe design revision. The model allows the performance of different probe designs to be simulated and compared to each other. This reduces costs and speeds up the development cycle as only the final, and most optimized, designs need to be physically built and tested. A highly refined mesh around the probe region maintains high accuracy of material flow characteristics. Post-processing of the results makes it easy to visualize changes caused by different probe geometries. Creation of an OFP-copper material model allows for reasonably accurate model validation based on evidence seen during the actual FSW process.

FSW tool material performance can be evaluated using the test protocol and parameters developed in the LCF test specifically created for a real FSW environment. This test can evaluate a materials performance as a FSW tool, without needing information often not available in a manufacturer's datasheet, such as high temperature fracture toughness. Small-scale test probes, with a known notch diameter acting as the preferential fracture zone, create a consistent test scenario for all materials. The current material, Nimonic 105, can be used to establish a baseline for comparing alternative material candidates. A ratio of weld length traveled before fracture to notch diameter is a fast and simple way to evaluate material performance. Microscopic and metallurgical analysis can also be used to more closely analyze material property changes during welding.

## 8.2 Conclusions

Earlier development projects and analytical design of a new probe:

- Selection of Nimonic 105 was well justified within the studied materials available at the time. It was one of the most reliable materials tested in terms of fracture resistance and creep rupture strength. Additionally, it maintained good ductility at high temperatures and showed no signs of hot shear deformation above 1000 °C and 20 m of weld.
- The canister weld process is temperature controlled to 845 ± 10 °C; temperature stability plays a large role in probe life as well as weld quality and stability.
- The current probe design emphasized reducing stress concentration points and improving probe strength. While the current probe does make acceptable welds, it was suggested that not all possibilities were explored and that optimal solutions for the tool were not found.
- The main target in a new design is to improve the material flow and forging effect at the tip of the probe. The new design aims to maintain all positive features of the existing probe design that are present near the shoulder.
- Analytical design performance parameters were developed to evaluate new probe design concepts. These parameters are: 1. Static volume; 2. Dynamic to static volume ratio; 3. Contact surface area. The best design, probe B, presents a 1.2% increase of static volume, a 3.3% increase of dynamic to static volume ratio, and a 1.2 % increase of contact surface area.

Numerical model developed to validate analytical designs:

- The purpose of the numerical model was to simulate FSW of copper using the original probe design and new probe design concepts.
- An Eulerian model, with a sliding mesh technique, allows full 3D simulation of material flow properties. The model is specifically designed to comparatively analyze different probe geometries strengths and weaknesses.
- High accuracy mesh allows for modeling of complex probe geometries, which is very uncommon in most other simulations.
- Sheppard-Wright flow stress based material model was developed for OFP copper that utilizes the Zener-Hollomon parameter to create a strain rate and temperature dependent viscosity.

Model validated with evidence seen in the actual FSW process:

- The simulations can be validated by comparing how the different viscosity and pressure zones compare to the actual process. The negative pressure zones are indicative of a stick-sliding flow transition and correlate well to the actual process.
- Pressure integration can be used to show forces and bending moments acting on the probe. Negative pressures cause errors in this calculation by artificially creating negative forces that are not physically possible.
- The leading X-force is still a useful tool for validation as it is more of a pressure gradient and is less prone to the errors from negative pressures. This force is also the most harmful to probe life as it creates the most bending stress in the probe. The model results overlap the actual machine measurements, but the model under predicts on average.
- Probe B shows a slight decrease in the leading force, and more axial force, compared to the original probe design, which reduces bending stress and gives more forging force instead. Probe B also shows a slightly shorter bending axis and more probe torque, implying greater material stirring and less material “pushing”.
- Constant viscosity and strain curves visually predict the boundary between different material flow zones well, but further validation is needed (perhaps microstructural analysis).
- The model shows dynamic loading effects through time as the probe completes one full rotation.

Numerical model shows proof of concept for new probe design capabilities:

- Comparative analysis methods include; velocity magnitude and direction, viscosity patterns of the material, and heat generation around the probe. In total, nine different probe design variations were simulated and analyzed.
- Probe B simulations show improved material flow and axial velocity near the tip of the probe, implying more forging ability and better mixing near the tip over the current design. Near the shoulder, the velocities are essentially the same, which is expected.
- Probe B also shows lower viscosities near the probe tip, which is caused by both increased strain rate and higher heat generation. This improves material mixing but the increased strain rate could also increase impact loading, reducing probe life.
- The new probe design (probe B) is not a result from an optimized design procedure. Namely, it still shows flaws with upward velocity shedding off the flute tips and stress concentrations near the probe tip. However, this probe is likely better than the current design and should be improved further through an optimization procedure, including experimental test implementation.

Theory and protocol developed for FSW LCF test for material testing:

- For many materials, there is data on tensile strengths available, typically for a relevant range of temperatures. However, many other material properties, that are critical for the material's performance in FSW, are often unavailable from the manufacturer.
- The LCF FSW test uses small diameter probes (8 mm). The test probe has a conical profile with three flats and a semi-circular notch at the top to act as preferential fracture zone. The loading conditions will be a combined effect of torsion, alternative bending and axial compression with a thermal field similar to the one seen in the actual application. The three flats will induce vibration and impact loading.
- A complete test theory and protocol has been established, with details on the assumed probe stresses and material fatigue limits based on the equivalent Von Mises stresses due to the forging force, torque, and bending loads. Action plans are considered to recover from any unexpected probe fractures.
- Preliminary results show high bending stresses in probes that are very dependent on probe length and weld travel speed. Results also confirm that test parameters are within the failure window of Nimonic 105.
- Test probes have a tendency to twist during the first 250 mm of welding, but not during plunge. After the initial twisting, the probes do not deform further unless the probe stress increases; this could be a strain hardening effect.
- SEM analysis shows large deformation zones near the fracture area on both fatigued and plunged samples. This deformation is likely due to the final overload fracture and not fatigue loading. Post fracture damage, due to the probe pieces grinding together, destroys the facture surface and makes finding signs of fatigue difficult.

## 8.3 Future Work

The next steps in the probe development can be divided into three main sections and are as follows:

Probe geometry design improvements:

- Further improve the geometry of the new probe concepts by reducing flute overlap and minimizing stress concentration zones around the MX features and probe tip.
- Manufacture full-scale test probes, once a design is finalized, and determine how well they work in the actual canister welding process.
- Optimize weld parameters once a final probe geometry and material have been selected.

Numerical model accuracy and efficiency improvements:

- Create a fully optimized, continuous, material model using only OFP-copper experimental data; this will eliminate the jumps in strain rate zones and improve flow stress accuracy.
- Introduce a proper tool/material slip condition and a fully modeled shoulder to improve the heat generation and shear stress calculations within the simulation.
- Include a particle tracking ability to further understand material flow properties.
- Create a sister FEM model to simulate the internal probe stresses and temperatures based on the CFD model surface loading predictions.
- Fully optimize mesh to determine when simulation solutions are no longer mesh dependent.
- Develop a structured mesh to possibly improve simulation run-time.

New probe material analysis and LCF FSW testing:

- Fully test Nimonic 105 using the LCF test protocol to establish a strong baseline for comparison of other material candidates and investigate hardening/twisting effects further.
- Perform CFD numerical modeling of the test probes. This can be used to further validate the numerical model and to give a clearer view of the test probe loading scenario.
- Acquire new material and test the promising new material candidates, such as Ni-Ir alloys [55] or Astroloy, using the established LCF test protocol.
- Compare the best candidates from the LCF test using metallurgical analysis methods to determine the best and most reliable probe material currently available.
- Develop an analysis method/approach to view the fracture surfaces of the fatigued probes by somehow removing the residual copper without completely destroying the fracture surfaces.

In all, the work done in this thesis helps progress the predictability, stability, and efficiency of FSW copper (or more specifically, thick OFP-copper). However, there is still a great deal more to do, much more than could fit in a single thesis. The work done here should not be considered a stopping point, but as a stepping-stone for future endeavors.

# 9 References

[1] The Welding Institute (TWI), "Friction stir welding patents - a stirring story, Case Study," 2007. [Online]. Available: http://www.twi-global.com/news-events/case-studies/friction-stir-welding-patents-a-stirring-story-002/. [Accessed October 2016].

[2] W. M. Thomas, E. D. Nicholas, J. C. Needham, M. G. Murch, P. Temple-Smith and C. J. Dawes, "Friction welding". USA Patent US5460317 A, 24 October 1995.

[3] L. Cederqvist, *Friction Stir Welding of Copper Canisters Using Power and Temperature Control,* Doctoral Thesis, Lund Univerisy, 2011.

[4] R. S. Mishra and M. W. Mahoney, Friction Stir Welding and Processing, ASM International , 2007, ISBN: 978-0-87170-840-3.

[5] P. Vilaca and W. Thomas, "State-of-the-Art in FSW Technology, Chapter 4," in *Structural Connections for Lightweight Metallic Structures*, Springer, 2012, pp. 85-124.

[6] J. Nenonen, "Development of friction stir welding tool for sealing copper canisters," Master's Thesis, Aalto University School of Engineering, 2016.

[7] H. Raiko, B. Pastina, T. Jalonen, L. Nolvi, J. Pitkänen and T. Salonen, "Canister Production Line 2012: Design, Production and Initial State of the Canister," Posiva Oy, 2012, ISBN 978-951-652-197-1.

[8] *Pocket Guide to Final Disposal,* Eurajoki: Posiva Oy, 2014.

[9] T. Purhonen, "State of the Art of the Welding Method for Sealing Spent Nuclear Fuel Canister Made of Copper, Part 1-FSW," Posiva Oy, Eurajoki, 2014.

[10] R. S. Mishra and Z. Y. Ma, "Friction stir welding and processing," *Materials Science and Engineering: R: Reports,* vol. 50, no. 1-2, pp. 1-78, 2005.

[11] Y. N. Zhang, X. Cao, S. Larose and P. Wanjara, "Review of tools for friction stir welding and processing," *Canadian Metallurgical Quarterly,* vol. 51, no. 3, pp. 250-261, 2012.

[12] D. Rowe and W. Thomas, "Advances in Tooling Materials For Friction Stir Welding," TWI and Cedar Metal Ltd, Cambridge, UK, 2005.

[13] SFS-EN 1976:2012, *Copper and Copper Alloys. Cast Unwrought Copper Products,* Suomen Standardisoimislitto (SFS), 2012.

[14] R. E. Andrews, "Friction stir welding - an alternative for sealing nuclear waste storage canisters," TWI Ltd & Swedish Nuclear Fuel and Waste Management Co (SKB), Cambridge, UK, 2004.

[15] C. E. Andersson and C. Westman, "High temperature materials for FSW tool applications," Swedish Institute for Metals Research, Stockholm, 2002.

[16] K. Savolainen, "Friction Stir Welding of Copper and Microstructure and Properties of the Welds," Aalto University School of Engineering, Doctoral Thesis, 2012, ISBN: 978-952-60-4500-9.

[17] K. Savolainen, J. Mononen, T. Saukkonen, H. Hänninen and J. Koivula, "Friction Stir Weldability of Copper Alloys," in *5th International Friction Stir Welding Conference*, Metz, France, September 14-16, 2004.

[18] R. Agrawal, R. Uddanwadiker and P. Padole, "Low Cycle Fatigue Life Prediction," *International Journal of Emerging Engineering Research and Technology,* vol. 2, no. 4, pp. 5-15, 2014.

[19] C. G. Andersson, "Development of fabrication technology for copper canisters with cast inserts," Swedish Nuclear Fuel and Waste Management Co, Stockholm, 2002.

[20] SKB, C. E. Andersson and R. E. Andrews, "Verktyg för friktionsomrörningssvetsning". Sweden Patent 0101663-3, 2004.

[21] L. Cederqvist, C. D. Sorensen, A. P. Reynolds and T. Öberg, "Improved process stability during friction stir welding of 5 cm thick copper canisters through shoulder geometry and parameter studies.," *Science and Technology of Welding and Joining,* vol. 14, no. 2, pp. 178-184, 2009.

[22] D. M. Neto and P. Neto, "Numerical modeling of the friction stir welding process: a literature review," *The International Journal of Advanced Manufacturing Technology,* vol. 65, no. 1, pp. 115-126, 2013.

[23] X. He, F. Gu and A. Ball, "A review of numerical analysis of friction stir welding," *Progress in Materials Science,* vol. 65, pp. 1-66, 2014.

[24] A. Kumar and L. Raju, "Influence of Tool Pin Profiles on Friction Stir Welding of Copper," *Materials and Manufacturing Processes,* vol. 27, no. 12, pp. 1414-1418, 2012.

[25] S. Cartigueyen and K. Mahadevan, "Study of friction stir processed zone under different tool pin profiles in pure copper," *IOSR Journal of Mechanical and Civil Engineering,* vol. 11, no. 2, pp. 6-12, 2014.

[26] H. N. B. Schmidt, T. L. Dickerson and J. H. Hattel, "Material flow in butt friction stir welds in AA2024-T3," *Acta Materialia,* vol. 54, no. 4, pp. 1199-1209, 2006.

[27] T. Källgren, "Investigation and modelling of friction stir welded copper canisters," Doctoral Thesis, Royal Insitute of Technology (KTH), Stockholm, 2010.

[28] P. Colegrove and H. Shercliff, "3-Dimensional CFD modelling of flow round a threaded friction stir welding tool profile," *Materials Processing Technology,* vol. 169, no. 2, pp. 320-327, 2005.

[29] T. Sheppard and D. S. Wright, "Determination of flow stress: Part 1 constitutive equation for aluminium alloys at elevated temperatures," *Metals Technology,* vol. 6, no. 1, pp. 215-223, 1979.

[30] R. Nandan, G. G. Roy and T. Debroy, "Numerical simulation of three-dimensional heat transfer and plastic flow during friction stir welding," *Metallurgical and Materials Transactions A,* vol. 37, no. 4, pp. 1247-1259, 2006.

[31] R. Nandan, G. G. Roy, T. J. Lienert and T. Debroy, "Three-dimensional heat and material flow during friction stir welding of mild steel," *Acta Materialia,* vol. 55, pp. 883-895, 2007.

[32] H. Schmidt, J. Hattel and J. Wert, "An analytical model for the heat generation in friction stir welding," *Modelling Simul. Mater. Sci. Eng,* vol. 12, pp. 143-157, 2004.

[33] R. Nandan, A. D. B. Prabu and T. Debroy, "Improving Reliability of Heat Transfer and Materials Flow Calculations during Friction Stir Welding of Dissimilar Aluminum Alloys," *Welding Journal,* vol. 86, pp. 313-322, 2007.

[34] S. D. Ji, Q. Y. Shi, L. G. Zhang, A. L. Zou, S. S. Gao and L. V. Zan, "Numerical simulation of material flow behavior of friction stir welding influenced by rotational tool geometry," *Computational Materials Science,* vol. 63, pp. 218-226, 2012.

[35] G. Q. Chen, Q. Y. Shi, Y. Fujiya and T. Horie, "Simulation of Metal Flow During Friction Stir Welding Based on the Model of Interactive Force Between Tool and Material," *Materials Engineering and Performance,* vol. 23, no. 4, pp. 1321-1328, 2014.

[36] H. Su, C. S. Wu, M. Bachmann and M. Rethmeier, "Numerical modeling for the effect of pin profiles on thermal and material flow characteristics in friction stir welding," *Materials and Design,* vol. 77, pp. 114-125, 2015.

[37] T. Källgren, L. Z. Jin and R. Sandström, "Finite Element Modeling of Temperature Distribution in Friction Stir Welding Process and Its Influence on Distortion of Copper Canisters," in *MRS Spring Meeting, Scientific Basis for Nuclear Waste Management XXVIII*, San Francisco, 2004.

[38] H. Pashazadeh, J. Teimournezhad and A. Masoumi, "Numerical investigation on the mechanical, thermal, metallurgical and material flow characteristics in friction stir welding of copper sheets with experimental verification," *Materials & Design,* vol. 55, pp. 619-632, 2014.

[39] B. Hadi, M. A. Shahbazi and M. E. Aalami-Aleagha, "3-dimensional numerical analysis of friction stir welding of copper and aluminum," *Journal of Mechanical Science and Technology ,* vol. 30, no. 8, pp. 3767-3776, 2016.

[40] J. F. Wendt and J. D. Anderson, "Governing Equations of Fluid Dynamics," in *Computational Fluid Dynamics an Introduction; Third Edition*, Springer Publishing, 2009, pp. 15-51, ISBN-13: 978-3540850557.

[41] ANSYS Inc, ANSYS 16 Fluent User's Guide, 2015.

[42] N. Davis, "Computational Fluid Dynamics, Finite Volume Method," 2015. [Online]. Available: https://uiuc-cse.github.io/me498cm-fa15/lessons/fluent/fvm.html. [Accessed March 2017].

[43] K. Budinski and M. Budinski, "Copper and Its Alloys," in *Engineering Materials Properties and Selection, 7th Edition*, Columbus, Ohio, Prentice Hall, 2002, pp. 603-628 & 792, ISBN: 0-13-030533-2.

[44] Special Metals, *Nimonic alloy 105,* Special Metals Corporation, 2007.

[45] Plansee, *Densimet and Inermet Tungsten heavy alloys,* URL: https://www.plansee.com/en/materials/tungsten-heavy-metal.html.

[46] T. Sheppard and A. Jackson, "Constitutive equations for use in predictions of flow stress during extrusion of aluminium alloys," *Materials Science and Technology,* vol. 13, no. 3, pp. 203-209, 1997, ISSN: 0267-0836.

[47] K. E. Tello, A. P. Gerlich and P. F. Mendez, "Constants for hot deformation constitutive models for recent experimental data," *Science and Technology of Welding and Joining,* vol. 15, no. 3, pp. 260-266, 2010.

[48] R. Sandström and J. Hallgren, "Stress strain flow curves for Cu-OFP," Materials Science and Engineering Royal Insitute of Technology (KTH), 2009, ISSN 1402-3091.

[49] L. Z. Jin and R. Sandström, "Steady non-Newtonian flows in copper and iron aluminide at elevated temperatures," *Materials Processing Technology,* vol. 189, pp. 428-434, 2007.

[50] A. Rusinek, J. A. Rodriguez-Martinez and A. Arias, "A thermo-viscoplastic constitutive model for FCC metals with application to OFHC copper," *International Journal of Mechanical Sciences,* vol. 52, no. 2, pp. 120-135, 2010.

[51] G. Fernandez, "Chapter 5: Modeling the Hot Flow Curve of Commercial Purity Coppers with Different Oxygen Levels," in *Constitutive relations to model the hot flow of commercial purity copper*, Barcelona, Doctoral Thesis,Universitat Politècnica de Catalunya, 2004, pp. 105-125.

[52] B. Barkely, "Analysis of Hot Isothermal Copper Extrusion for Multi-Channel Profiles," Master's Thesis, the Russ College of Engineering and Technology of Ohio University, pp. 34-36, 2013.

[53] Y. V. R. K. Prasad and K. P. Rao, "Processing maps and rate controlling mechanisms of hot deformation of electrolytic tough pitch copper in the temperature range 300–950 C," *Materials Science and Engineering A,* vol. 391, no. 1-2, pp. 141-150, 2005.

[54] Y. V. R. K. Prasad and K. P. Rao, "Influence of oxygen on rate-controlling mechanisms in hot deformation of polycrystalline copper: oxygen-free versus electrolytic grades," *Materials Letters,* vol. 58, no. 14, pp. 2061-2066, 2004.

[55] T. Nakazawa, K. Tanaka, K. Sakairi, Y. S. Sato, H. Kokawa, T. Omori, K. Ishida and S. Hirano, "Performance of iridium containing nickel base superalloy for friction stir welding of Ti-6Al-4V alloy," p. 6, 2016.

# 10 Appendices

Appendix 1: Additional Simulation Results Images. 2 pages

Appendix 2: Additional LCF Test Images. 4 pages

# Appendix 1: Additional Simulation Results Images

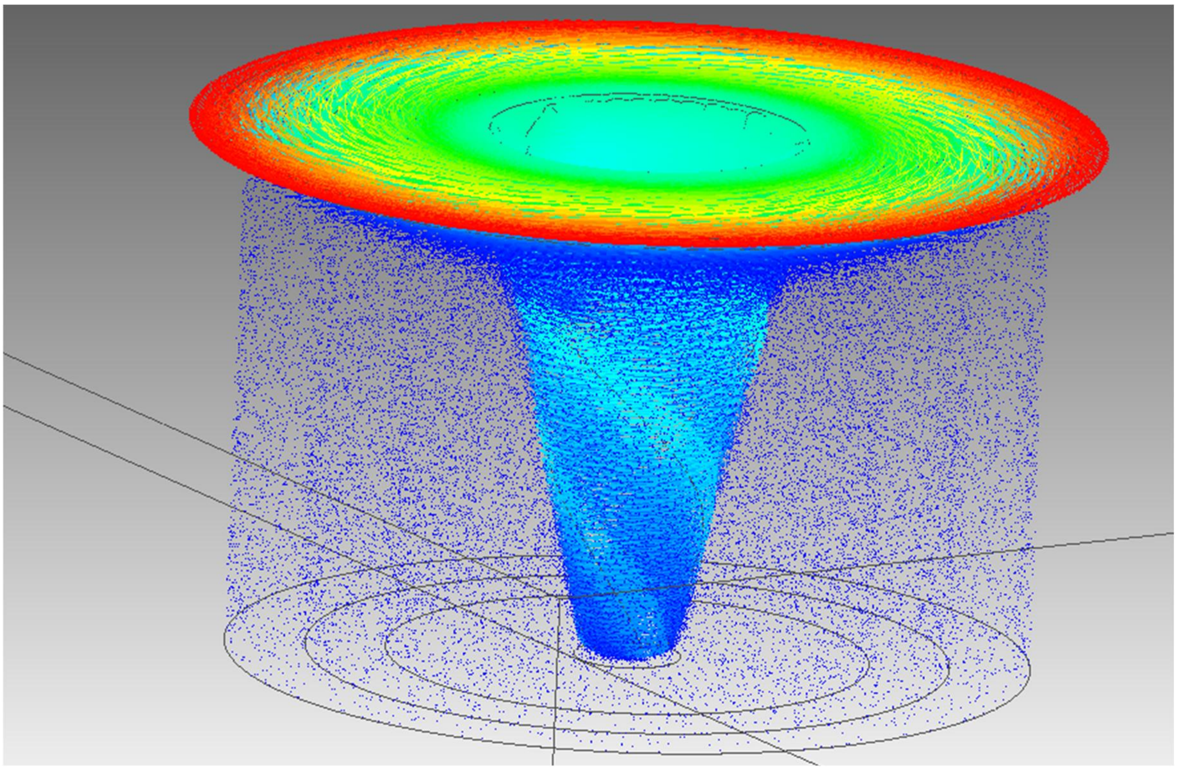

Original probe global velocity vectors.

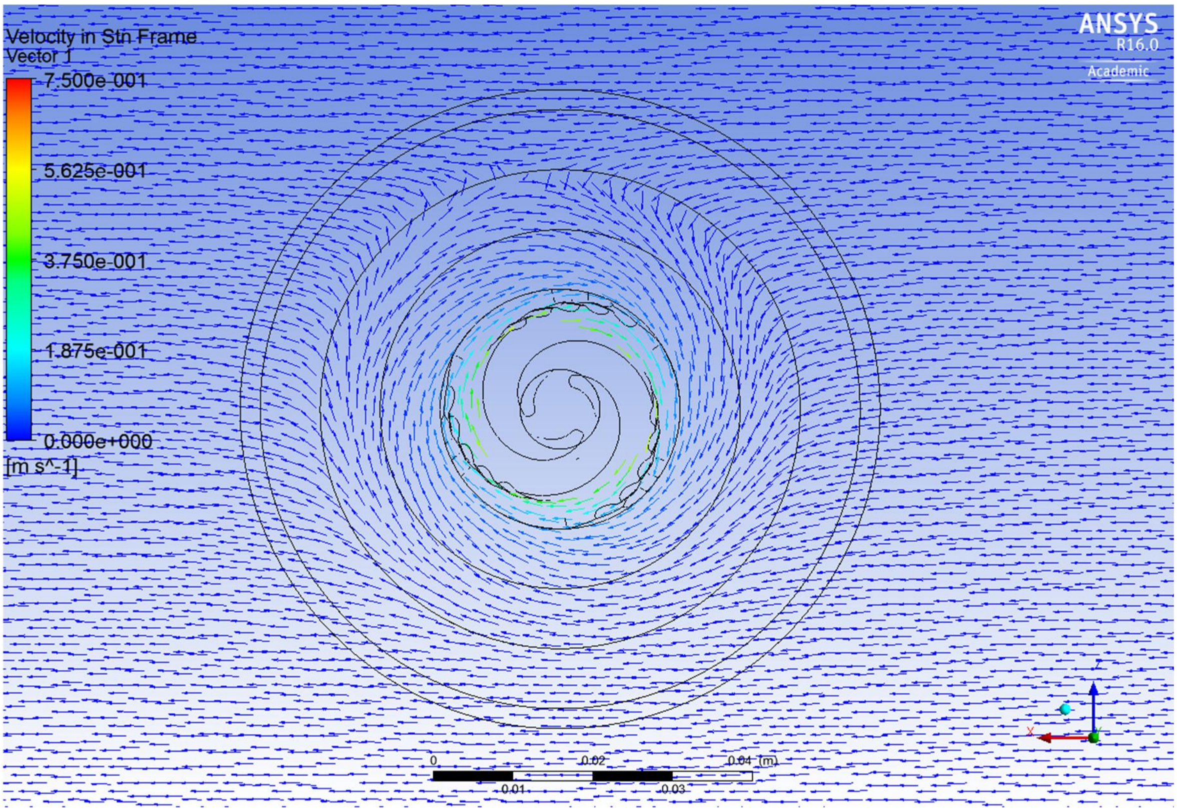

Original probe plane velocity profile at 0.35 mm above the tip.

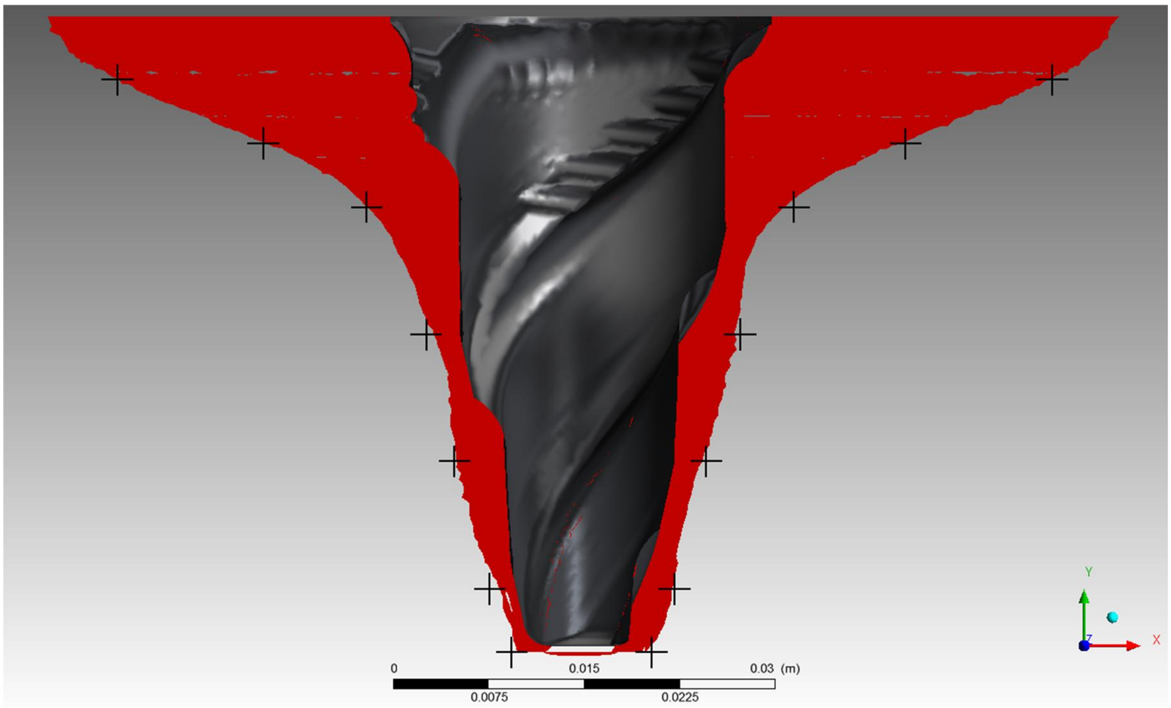
0
0.015
0.03 (m)
0.0075
0.0225
Y
X

Original probe strain rate isosurfaces.

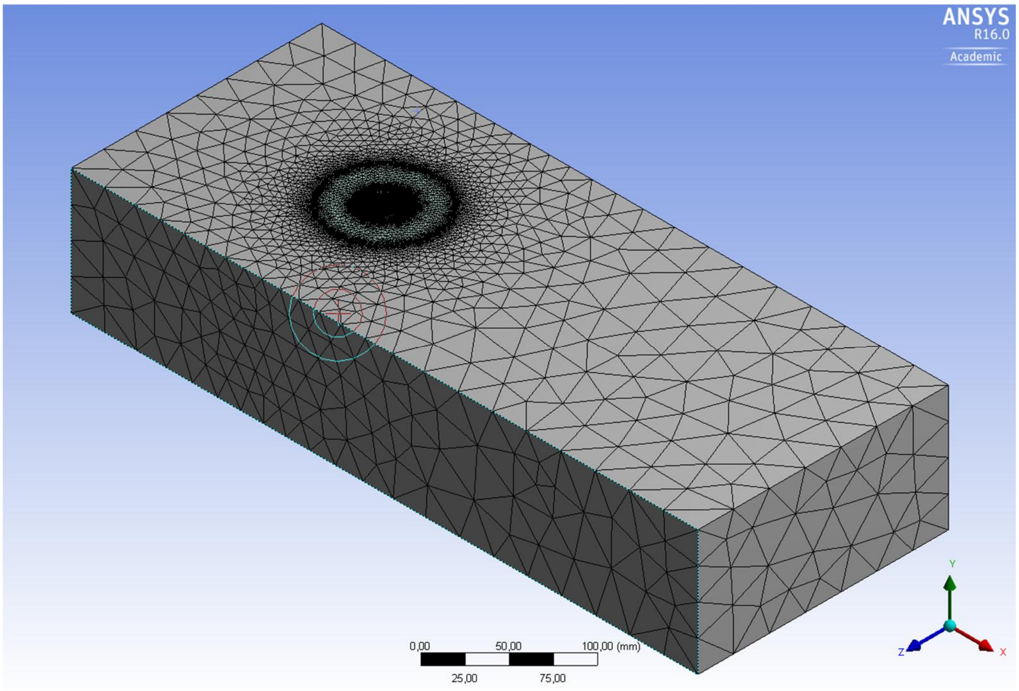
ANSYS
R16.0
Academic
0,00
50,00
100,00 (mm)
25,00
75,00
Y
Z
X

Early model mesh and simulated region.

# Appendix 2: Additional LCF Test Images

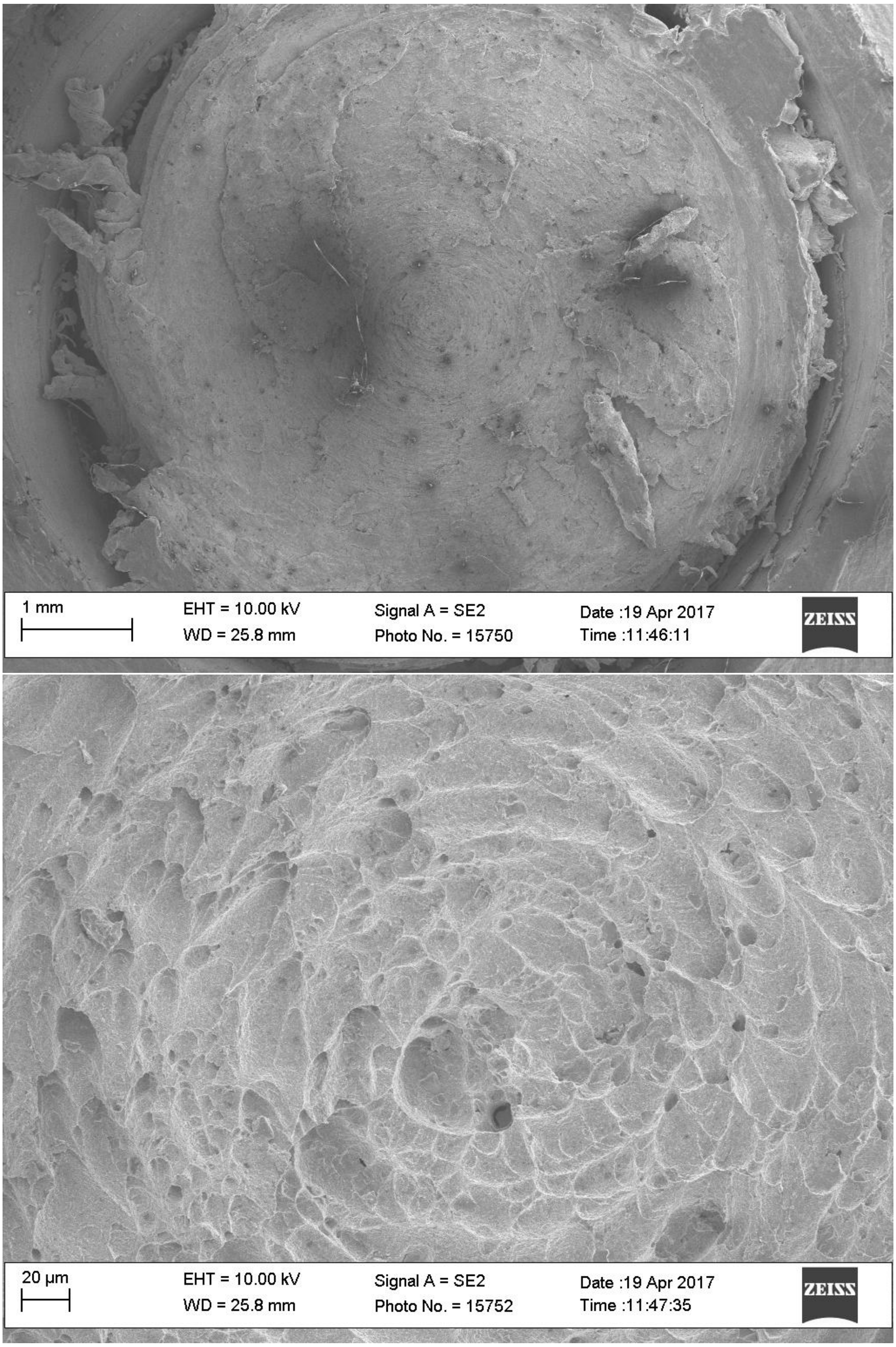
1 mm
EHT = 10.00 kV
WD = 25.8 mm
Signal A = SE2
Photo No. = 15750
Date :19 Apr 2017
Time :11:46:11
ZEISS
20 µm
EHT = 10.00 kV
WD = 25.8 mm
Signal A = SE2
Photo No. = 15752
Date :19 Apr 2017
Time :11:47:35
ZEISS

Fracture surface images of the probe half that remained in the copper.

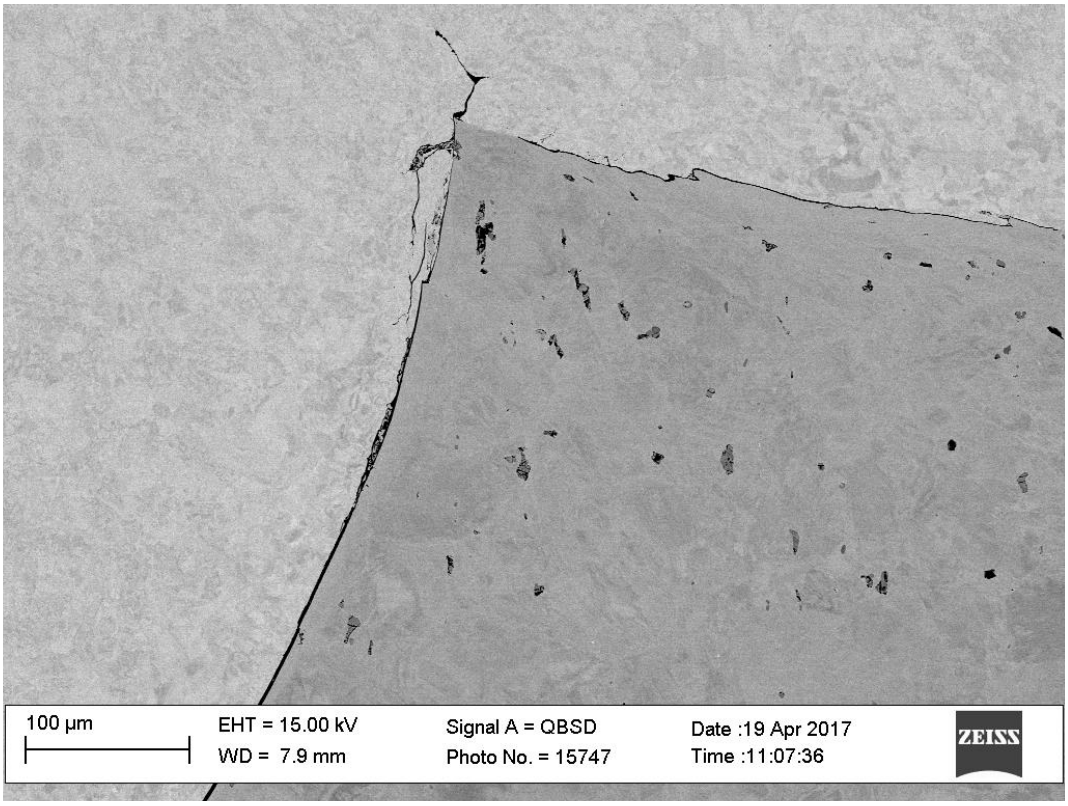
100 µm
EHT = 15.00 kV
WD = 7.9 mm
Signal A = QBSD
Photo No. = 15747
Date :19 Apr 2017
Time :11:07:36
ZEISS

Copper-Nimonic interface of the corner of fractured probe E (2,935 mm of weld).

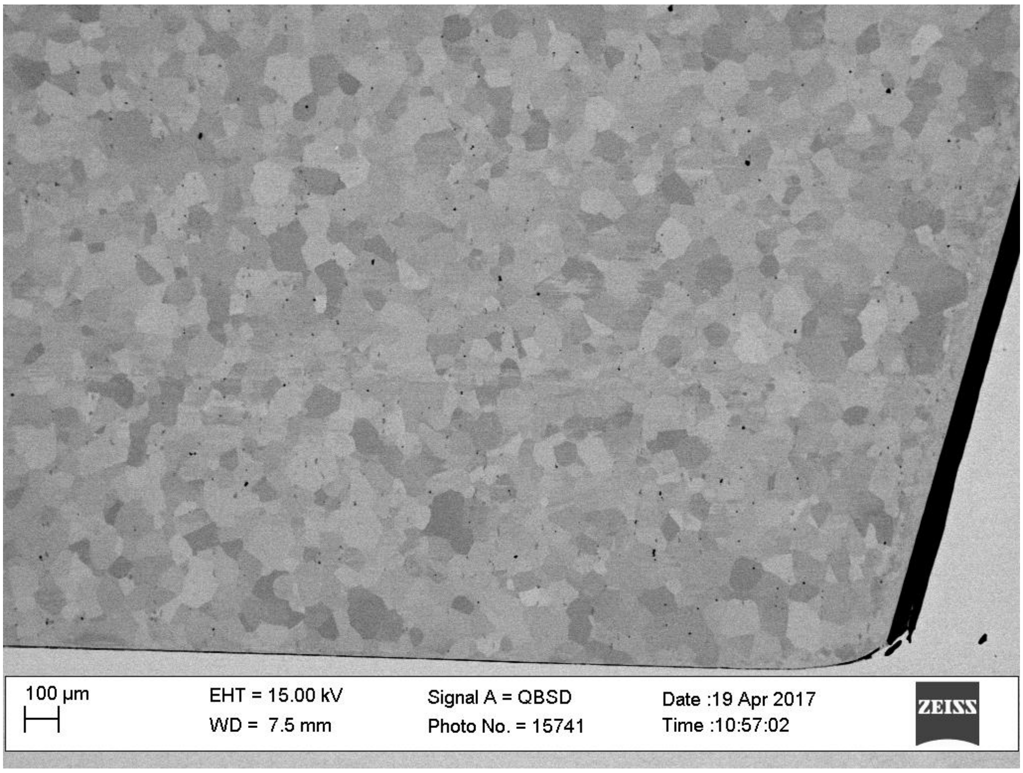
100 µm
EHT = 15.00 kV
WD = 7.5 mm
Signal A = QBSD
Photo No. = 15741
Date :19 Apr 2017
Time :10:57:02
ZEISS

Side and bottom edge of probe E (2,935 mm of weld), notice the deformation zone along the side but not along the bottom.

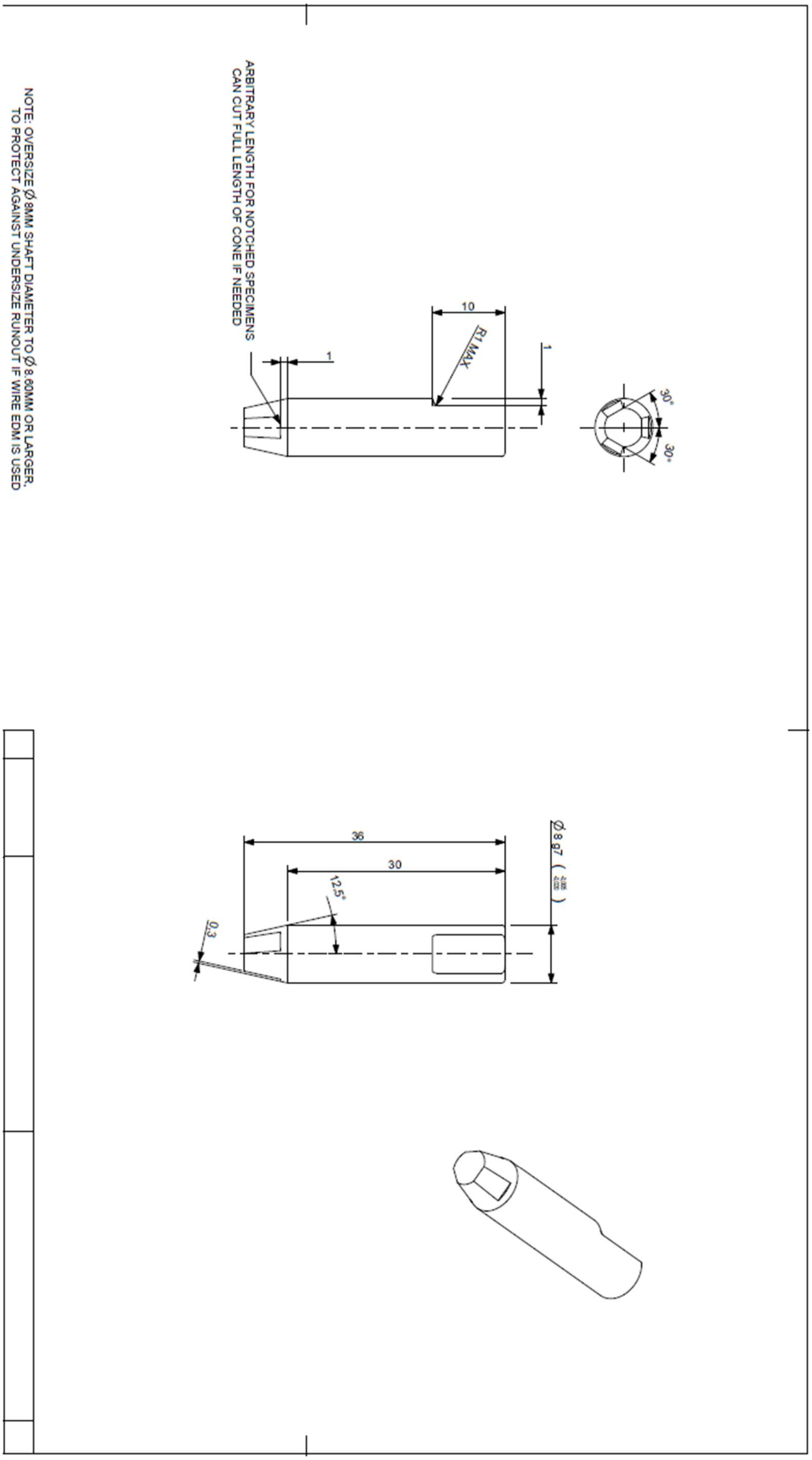
NOTE: OVERSIZE Ø 8MM SHAFT DIAMETER TO Ø 8.60MM OR LARGER,
TO PROTECT AGAINST UNDERSIZE RUNOUT IF WIRE EDM IS USED
ARBITRARY LENGTH FOR NOTCHED SPECIMENS
CAN CUT FULL LENGTH OF CONE IF NEEDED
1
10
R1 MAX
1
30°
30°
36
30
12.5°
0.3
Ø 8 g7

Revision 2 probe manufacturing drawing.

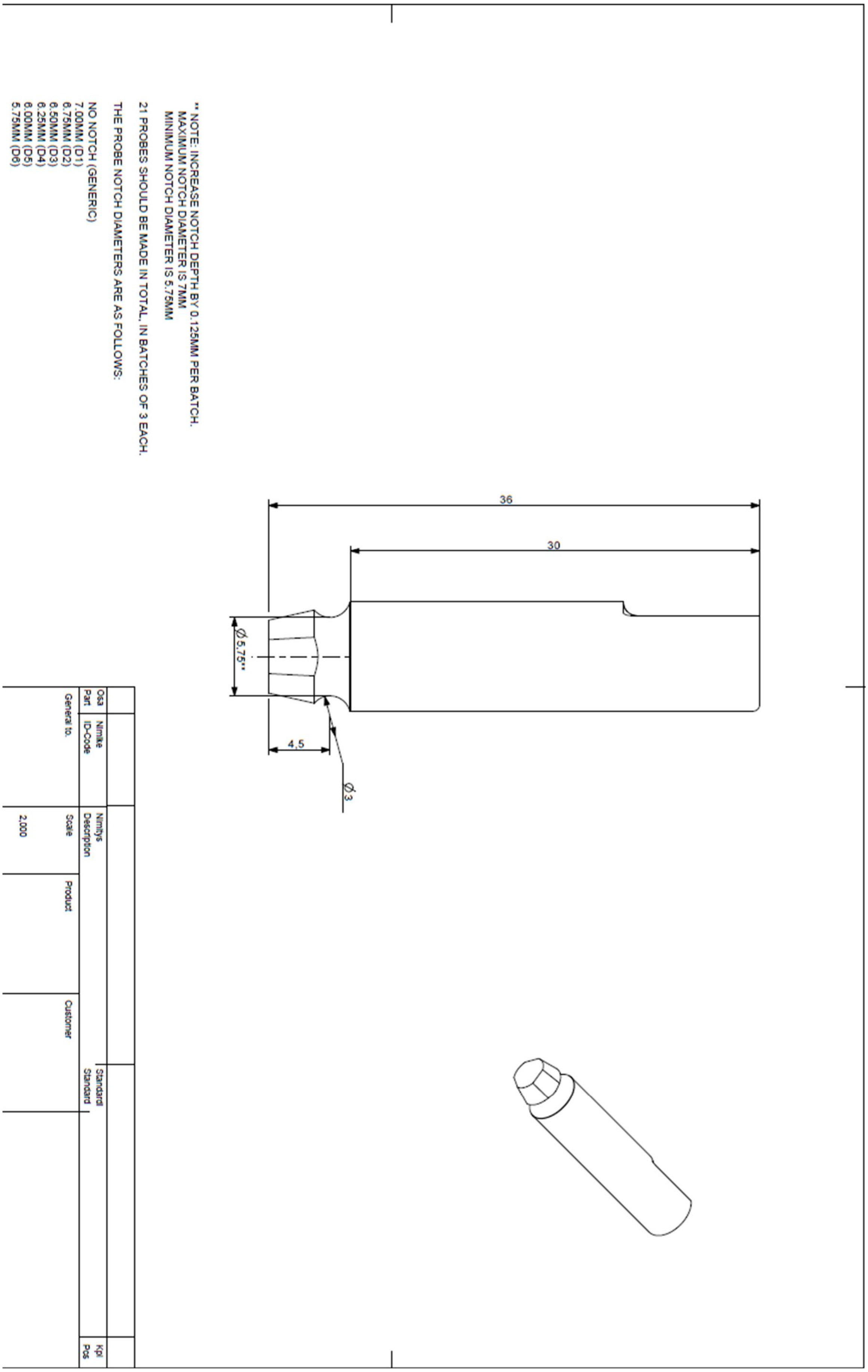

** NOTE: INCREASE NOTCH DEPTH BY 0.125MM PER BATCH.
MAXIMUM NOTCH DIAMETER IS 7MM
MINIMUM NOTCH DIAMETER IS 5.75MM

21 PROBES SHOULD BE MADE IN TOTAL, IN BATCHES OF 3 EACH.

THE PROBE NOTCH DIAMETERS ARE AS FOLLOWS:

NO NOTCH (GENERIC)
7.00MM (D1)
6.75MM (D2)
6.50MM (D3)
6.25MM (D4)
6.00MM (D5)
5.75MM (D6)

36
30
Ø 3
4,5
Ø 5,75**
Osa
Part
Nimike
ID-Code
Nimitys
Description
Standardi
Standard
Kpl
Pcs
General to.
Scale
2,000
Product
Customer

Revision 2 notch manufacturing drawing.